Torque measurement in turbulent Couette-Taylor flows

Borja Martínez Arias

Borja Martínez Arias. Torque measurement in turbulent Couette-Taylor flows. Fluids mechanics [physics.class-ph]. Université du Havre, 2015. English. NNT : 2015LEHA0004 . tel-01215465

HAL Id: tel-01215465
https://theses.hal.science/tel-01215465
Submitted on 14 Oct 2015

THÈSE DE DOCTORAT

préparée à

L'UNIVERSITÉ DU HAVRE

pour l'obtention du grade de

DOCTEUR DE L'UNIVERSITÉ DU HAVRE

Discipline : **Sciences pour l'ingénieur**
Spécialité : **Mécanique des fluides**

par

Borja MARTÍNEZ ARIAS

TORQUE MEASUREMENT IN TURBULENT COUETTE-TAYLOR FLOWS

Soutenue le 23 septembre 2015

Devant le jury composé par :

G. BRENN :	Professeur à la Graz University of Technology	*Rapporteur*
O. CADOT :	Professeur à l'ENSTA-ParisTech, Palaiseau	*Rapporteur*
L. DANAILA :	Professeure à l'Université de Rouen	Présidente
C. EGBERS :	Professeur à la BTU Cottbus-Senftenberg	*Rapporteur*
I. MUTABAZI :	Professeur à l'Université du Havre	*Directeur de thèse*
F. RAVELET :	Maître de Conférences HDR à l'ENSAM-ParisTech	

Invité

J. PEIXINHO :	Chargé de recherche CNRS HDR	*Encadrant*

Laboratoire Ondes et Milieux Complexes (LOMC), UMR CNRS 6294

Acknowledgments

I never thought about doing a doctoral thesis. Never.

This adventure started at the end of May 2012, some minutes after passing my viva voce to obtain the engineering diploma. One of my project supervisor, Carlos del Pino, reminded me that his friend Jorge Peixinho had sent a PhD offer to work in France. Well, I decided to email him. Then, he addressed me to Innocent Mutabazi. Two weeks later I was hired to work on something called Taylor-Couette flow.

Living in a nice place is gratifying. Doing interesting activities during the week is pleasant. But, if you are not surrounded by the appropriate people to share your activities in your place, your daily life can become quite tough. I would like to acknowledge some of the people that I have met during the last three years, because thanks to them I have been able to live the most enriching stage of my life. I would also like to thank all the people and institutions that have allowed me to complete this doctoral thesis.

The first person I would like to thank is my supervisor Dr. Jorge Peixinho. He has been there every time I needed help. He has trained me as a researcher and has taught me a lot of things about the world of research. From the beginning he has guided me during this long project. It was the first time that he worked on the Taylor-Couette flow, but he has always had nice ideas about what kind of experiment to do. Despite all the difficulties that we have found and the limitations with the experimental set-up, he has known how to adapt to the situations and to encourage me to go ahead all the time. He has treated me as an equal, so he has listened to me and has given me the freedom to propose and test my own ideas. The continuous communication that we have had, almost every day, has allowed us to advance very fast. Therefore, I really want to acknowledge him all the time that he has spend with me. Also, I want to thank him the time he has spent during the corrections of the manuscript and the writing of the articles. The success of this doctoral thesis would not have been that great without him.

Je tiens également à remercier mon directeur de thèse, le professeur Innocent Mutabazi. D'abord, merci de m'avoir donné l'opportunité de faire cette thèse de doctorat. Je me souviendrai toujours de cette conversation téléphonique que nous avons eu en juin 2012, quand j'étais à Málaga, après laquelle on m'a offert le post de doctorant. J'ai toujours essayé d'avoir les yeux et les oreilles très ouverts pour apprendre autant que possible de lui, en tant que directeur de thése et comme directeur de laboratoire. Je lui remercie aussi tout le temps qu'il a dépensé ces derniers mois avec la correction du manuscrit de thèse et pour les conseilles qu'il m'a donnés sur la structuration des chapitres. Grâce à son expérience la qualité de ce projet de thèse a été très haute.

Je veux aussi remercier les membres de mon jury de thése pour leur présence le jour de la soutenance, Günter Brenn, Olivier Cadot, Christoph Egbers, Luminita Danaila et Florent Ravelet. En particulier, je remercie M. Brenn, M. Cadot et M. Egber pour avoir rapporté mon manuscrit de thèse.

Je remercie le Centre National de la Recherche Scientifique (CNRS) et l'Agence Nationale de Recherche (ANR), qui à travers du programme Investissements d'Avenir (ANR-10-LABX-09-01), LabEX EMC^3 ont financé cette thése encadrée dans le projet TUVECO (Turbulence et Viscoélasticité dans les Écoulements Complexes)

Je remercie tous les membres de l'équipe de mécanique des fluides du LOMC. Merci Olivier pour ta participation dans les discussions scientifiques qui nous a aidée à améliorer la qualité de notre papier. Merci Arnaud pour les semaines qu'on a passé ensemble pour faire marcher la LIF et pour chaque fois que tu m'a aidé. J'ai aussi trouvé très sympathiques les conversations qu'on a eu, en particulier sur la natation et le tennis. Merci Charlotte pour toutes les fois que tu m'a aidé avec les polymères viscoélastiques. C'est trs̀ important d'avoir quelqu'un comme toi dans un équipe de recherche, toujours prête à participer et à aider les autres. Je te souhaite une bonne carrier en tant que chercheuse. Et merci aussi Yang pour toutes les fois que tu m'a aidé.

Carole est simplement super. Elle est la personne la plus efficace que j'ai jamais connue. Elle m'a toujours aidé très rapidement avec n'importe quel soucis, même quand je ne parlais pas trop français et elle faisait l'effort de me comprendre. Toutes les doutes que j'ai eu sur des trucs administratives, professionnelles ou personnelles, Carole a toujours su les résoudre. Je ne vais pas énumérer toutes les fois qu'elle m'a aidé, parce que je ne finirais jamais. Merci Carole.

Avec Claude j'ai pu apprendre plein des choses qui ne sont pas ni dans les bouquins, ni dans les articles, mais qui sont essentielles pour un expérimentateur. Si quelque chose peut se fabriquer pour une expérience, Claude peut le faire. Il a fabriqué des pièces très importantes pour mes expériences, qui n'étaient pas faciles à faire. En plus, j'ai passé pas mal de temps à côté de lui dans l'atelier pour d'apprendre toutes les choses qu'il m'expliquait. Merci Claude.

Merci Valérie parce que tu es toujours souriante et prête à aider tout le monde. Tu t'en préoccupe de nous les doctorants pour que l'on soit bien dans le laboratoire. Merci, particulièrement, de m'avoir aidé avec la préparations du pot de thèse. J'espère que tu continues à accueillir les nouveaux doctorants de la même façon que tu l'as fait avec moi.

Merci Huge de m'avoir aidé avec les d'expériences et pour le temps que tu as passé avec moi dans la salle de manipulation.

Je remercie aussi Michel Grisel et Frédéric Renou, du groupe de chimie de l'URCOM, de nous avoir aidé avec les mesures rhéologiques.

Maintenant je veux remercier tous le reste de personnes du laboratoire. Merci Greg et Gaël, parce que vous êtes super sympathiques et très gentils. Merci Antoine pour le temps qu'on a passé discuter sur la nouvelle machine et pour ta gentillesse. Fabien, je pense que maintenant tu es convaincu que l'Espagne et la puissance sportive la plus grande du monde et que l'on mange mieux en Espagne que en France. François, toi et Florence vous êtes énormément sympathiques et gentils, donc merci. Merci Benoît pour les conversation que l'on a eu, surtout dans la salle à manger. Laurent, creo que si escribo en español vas a comprender. Ha sido un placer conocerte y te deseo lo mejor. M. Saouab, vous avez été très gentil avec moi et vous vous êtes intéressé sur l'évolution de ma thèse, donc merci. Grégoire, l'informaticien le plus efficace que j'ai jamais connu. Merci pour toutes les fois que tu m'a aidé, même quand tu n'étais plus au LOMC. Émilie, toujours gentille et sympathique. Merci pour les fois que tu m'a aidé avec les papiers administratifs. Jérôme, une de tes étudiantes m'a dit que vous êtes un très bon proffeseur. Je vous souhaite une bonne retraite. Merci aux reste du personnel du LOMC pour faire de ce laboratoire un endroit très convivial.

Les doctorants, la basse de ce laboratoire et l'avenir de la recherche mondial. Je vais m'en occuper de chacun de vous individuellement.

Dude, ingeniero, mouhandis, la 9abra 9ontenta, hola guapo qué haces esta noche, Raounak. ¡¿Qué te voy a decir que ya no sepas?! Que eres alguien excepcional, una de las mejores personas que he conocido en mi vida, siempre sonriente y con un corazón enorme. Muchísimas gracias por todos los momentos vividos juntos, desde Francia a Marruecos, pasando por España. Creo que juntos hemos visitado la mayor parte de los pueblos de Normandía. Siempre que he necesitado hablar en español, tú estabas ahí para escuharme. En fin (giro de cabeza español), espero que siempre mantengamos nuestra amistad, la cual valoro enormemente, y que tengas un próspero futuro allí donde estés. Mi casa siempre será la tuya. Gracias, merci, shukran.

El caballero del apocalipsis, el hombre de hierro, hola qué pasa, pero, pero, perooo, super Saïmoun, Simon. Amigo, j'ai trouvé en toi mon double français. Dès le début tu m'a toujours aidé pour connaître mieux ton pays, maintenant c'est aussi le mien, sa langue, sa culture. Merci pour tous les moments que l'on a passés ensemble, une bonne partie devant une biére Charles Quint. Merci aussi, parce grâce à toi, mon niveau de français écrit a amélioré énormément, tu as passé beaucoup de temps à m'aider. Une des graphique de l'article est aussi bonne grâce à toi (je n'ai pas oublié ça). J'ai pu connaître Roland Garros avec toi (mon vrai but ici en France) et le Mater à Bercy. En fin, en Espagne tu auras toujours ton amigo español. Gracias, merci.

Comandante, ¡oye, chico!, doctor Hernández Vera, Mario. Dicen que vivir en un país extranjero y encontrar un amigo que hable el mismo idioma que tú, no tiene precio. Son infinitos los cafés y las cervezas que nos hemos tomado en los bares del Havre. He disfrutado muchísimo con la cantidad de conversaciones que hemos tenido sobre diversos temas. Bueno, aunque nuestro tema preferido ha ocupado la mitad del tiempo, o más. Muchas gracias por haberme escuchado y recomendado en eso momentos no tan fáciles en este rincón del mundo tan distinto de donde tú y yo provenimos. Siempre tendrás un amigo en España que te estará esperando con los brazos abiertos, si decides volver algún día. Gracias.

Sylvain, Mathieu et Marine. Vous avez été un de mes premiers amis ici en France. Merci de m'avoir accueilli et de m'avoir appris le français au début, quand je disais que des conneries mal traduites de l'espagnol. Sylvain, j'apprécie beaucoup tout les moments que l'on a passés ensemble au Havre et en dehors du Havre. Mathieu, j'ai beaucoup aimé nos conversations sportives. Grâce à toi, le rugby n'a plus de secrets pour moi. Marine, merci d'être aussi gentille et de m'avoir aidé quand j'ai eu besoin.

Moi je connais une bretonne, qui énervais les gens. Céline, toujours souriante et sympathique. Merci pour tous les moments qu'on a partagés, et surtout quand on s'est embêté. Guillermo el conquistador. Guillaume, merci pour ton amitié et pour tous les bons moments de convivialité que l'on a vécu pendent la collocation. Tu m'as fait rejouer aux jeux vidéo après très long temps. Et merci Pauline pour les soirées sushi, tu es très sympathique. Xuezhou, la seule fille dans notre bureau. Je ne sais pas combien de "choses" tu nous as entendu dire... Tu es très sympathique, très gentille, très courageuse d'être dans un pays aussi loin et différent que le tien. Je te remercie les ondes positives que tu transmettres toujours. Je suis sûr que tu vas avoir un avenir fantastique là où tu décides. Miss Eid. Joanna, merci pour tous les moments partagés et les longs conversations que nous avons eu. J'ai pu connaître un pays sans avoir y être. Le mélange entre la nourriture libanaise et l'Almaza est un de plus délicieux repas que j'ai jamais essayé. Je te souhaite bon courage pour la suite, je suis sûr que tu vas réussir. Benedicto El bueno. Benoît, merci pour les moments conviviales au laboratoire et en dehors du laboratoire. Grâce à toi, j'ai pu connaître des choses sur la France pendent nos conversations journalières au RU. JB (mais prononcé en espagnol, jota be). Jean Baptiste, tu es quelqu'un toujours prêt à parler et à participer avec tout le monde, ça fait que le groupe soit plus animé. Je te souhaite un avenir avec plein de succès. Hermana, Nezha. Je hésiterai toujours sur quel est vraiment ton niveau d'espagnol. Je pense que tu comprendre absolument tout. Tu est très sympathique et gentil avec moi et très ouvert. Courage pour la suite. Tony, chaton ("gatito" ça fait un peu bizarre en espagnol). Anthony, tu est très sympathique et aussi gentil. Je pense que une fête sans toi, ce n'est pas la même chose. Clément, merci pour tous les moments et les conversations partagés, surtout à l'heure de manger au RU. Mr. Selvam. Kamal, thank you for the two years that we have shared as Jorge's PhD student. I hope you finsish your PhD successfully and that you can go back to India as soon as possible. Good luck for the future. Merci aussi Antoine, Camille, Rinha, Bouchra, et ceux qui j'oublie. Ce n'est pas facile de se souvenir de tout le monde. Merci aussi aux stagiaires, Mohamed, pour les moments partags avec la LIF, Clément, Arnaud, j'espère que tu utilise bien ma place.

I would like acknowledge all the members of the LAS in the Brandenburg Technical University of Cottbus for the three months I spent there during the research project. First, I want to acknowledge the professor Christoph Egbers for having accepted me to work in his laboratory. Thank you also for having accepted reviewing my thesis manuscript and for coming to Le Havre the day of my PhD defense. Thank you professor Uwe Harlander for having helped me with the EuHIT proposal and for your interest during my stay in Cottbus. Thank you Sebastian for having participate in the project, for all the help that you provided me and for the nice moments that we have spent out of the laboratory, when drinking coffee (while I learned German with the cookies wrapping), our when we went to have diner. Thank you Andreas for having participate with me during the torque measurements and the photograph acquisition in the laboratory. The time we spent, in the laboratory and in the Mensa, was very pleasant for me. I wish all the best for your PhD and the future. Nacho!, my favorite Turkish guy. Emir, thank you man for your help and company. We spent a lot of time while dinning or drinking Radebergers in Cottbus. You know, I have not forgotten it, we still waiting for your certificate that you have to bring to from Turkey. You know which certificate. I wish you all the best for the future. I am sure you will be a great Dr. Ing. Amir, one of the kindest person I have ever known. It was a pleasure to meet you and to know a little from Iran through you. Paco de Luca will be always one part of you. Never stop playing the guitar in the way you do it. All the best for the future. I also want to acknowledge the rest of the people in the LAS, Ion, Rodica, Michael, Andreas, Matthias, Torsten.

Sonia, j'ai été très chanceux d'avoir pu partager plein de bons moment avec toi. Tu m'as fait découvrir ton pays, l'Allemagne, même si tu ne le sens pas comme a, et plein de choses que je n'aurais jamais connues sans toi. The time we spent together was very enriching for me and I will never for get it. You are an inspiring person. Merci, thank you, danke, gracias.

Alors, maintenant je passe au tennis. a n'a rien à voir avec la ths̀e, mais ça fait partie de mon expérience ici. Après le laboratoire, le HAC Tennis c'est l'endroit où j'ai passé plus de temps. Donc, merci à tous les membres du HAC pour tous les matchs que j'ai joués avec vous et pour tous les bons moments que l'on a passés ensemble pendent les matchs par équipe, les barbecues et les soirées apéro. Chopinou, Olivier, merci pour tous les matchs qu'on a joué. Merci à toi aussi, Guillaume, on a joué pas mal de parties. Nico Aubourg, toujours super gentil avec moi. Je me suis amusé beaucoup durant nos matchs. Nico Campeón, capitán, nous savons que dans un an nous aurions battu les frères Bryan. Philippe, toujours super sympathique. Tu connais plus sur l'histoire que les bouquins que l'on lissait au collège. Fred, toujours très sympathique avec moi. On a aussi joué des très bons matchs ensemble. En fin, merci Juillet, Mika, Brice, MarcO, Julien, Fred, et le reste.

Merci Alban de m'avoir entraîné pendent trois ans. J'ai passé des moments très conviviales pendent les cours de tennis. Mon coup droit et mon services ne sont plus les mêmes depuis tes conseils.

La pequeña Marioneta, t'es prête Marionnette?, la campeona de tenis de Normandía, la personne la plus exigeante que j'ai jamais connue, et aussi la personne qui ferme mon cercle de confiance en France, Marion. On s'est connu peu à peu, coup droit après coup droit (pas avec le revers...), et j'ai très très bien aimé ce processus de connaissance. Tu as toujours plein de énergie (patata caliente) et comme on dit en espagnol, tu transmet "buen rollo". On s'est bien amusé et on a bien rigolé à chaque fois que l'on s'est vu. On a partagé des très bons moments lesquels je vais toujours m'en souvenir. Siempre tendrás a tu amigo español allá donde estés. Muchas gracias por tantísimas cosas de Francia que me has enseñado. Gracias a ti también he podido conocer mejor tu bellísima región, la Normandía, y una familia maravillosa. Merci, gracias.

Y ya voy terminando con España. Carlos, Luis, si nos fuera por vosotros, yo no estaría escribiendo esto ahora. Muchas gracias por introducirme en este bonito mundo de la investación en la mecánica de fluidos. Me lo he pasado muy bien cada vez que nos hemos visto cuando volvía a España. Espero que las cenas de navidad no se acaben nunca. Nunca dejéis de exportar doctorandos tan bien preparados por el mundo. Eso sí que es marca España. Señor doctor don José Manuel Gallardo. Ahora ya te puedo tutear, aunque yo sólo sea un doctorcito. Gracias por tu interés estos tres años en la evolución de mi tesis (y de juego de tenis). En nada estamos los dos en España. Recuerdos también al resto de personas del departamento de mecánica de fluidos de la Universidad de Málaga y los que ya no están, Paloma, Sergio, Jose, Ignacio, Ramón.

Mis cuatro mosqueteros españoles, Joselón, Jorginhus, Raulinhus y el Chacho. Jose, gracias por las infinitas conversaciones que hemos tenido cada vez que he vuelto a Marbella. Siempre que pensaba en volver, me agradaba saber que podría echarme unas cuantas cañas contigo. Jorge, eres un crack, así de fácil. Siempre me encanta cuando nos vemos y me lo paso súper bien. Pasa rápido el tiempo, hace nueve años que nos conocemos y desde el primer día has sido de mis mejores amigos. Elvira, desde el primer día eras ya mi amiga. Me han gustado mucho los largos mensajes que nos hemos intercambiado. Dentro de nada serás doctora, ¡ánimo! Raúl, eres un máquina, no hay mejor descripción posible. También nueve años de amistad y desde el primer día me lo paso muy bien contigo. Eres una persona inspiradora. Miriam, siempre encantadora y con ganas de hablar de todo. Gracias a los dos por los buenos momentos pasados cuando volvía a España. El tipo más inteligente que me he echado a la cara, Rubén de Málaga. Chacho, eres un tipo legal. Gracias por estos años de amistad y por las cervezas que nos hemos tomado, sobre todo en feria. Dentro de nada doctor también.

Ya ya termino con mi GRAN FAMILY. Vosotros sois mi España, lo primero que se me venía a la cabeza cuando pensaba en volver a casa y los primeros a los que quería ver nada más llegar. Os quiero agradecer todo el cariño y apoyo que me habéis dado desde la lejanía, en los retornos a la patria y cuando habéis venido a la vecina Francia. Siempre me he sentido muy querido y me lo habéis demostrado vez que volvía a España. Mis primos, Carlos y Alejandra, que aunque no os viniese muy bien, hacíais el esfuerzo de venir a Marbella a verme. Mis tíos, Carlos y Menchu, porque siempre han estado pendientes de mí como si fuera un hijo más. Y mis padres, el punto sólido y fuerte en el que siempre me he apoyado cada vez que las cosas no venían fáciles y con los que he compartido todos las buenas y también duras experiencias que he vivido en estos tres años. Infinitas llamadas telefónicas y videollamadas por Skype. Gracias por todo el apoyo, de todo tipo, que me habéis dado estos tres años. Gracias por las visitas a Le Havre. Simplemente, gracias por estar ahí.

Borja Martínez Arias

Le Havre, Francia. Septiembre de 2015.

Es de bien nacido ser agradecido, dicho español.

Creo que la curiosidad, entendida como la fascinación por aprender cosas nuevas, es una de las mejores acompañantes en la vida. Te permite conocer y comprender el mundo que te rodea, y no sólo eso, te permite conocerte a ti mismo. Atrévete a preguntar, atrévete a probar, atrévete a investigar. Pon en duda todo lo que crees saber. Sé curioso.

A mis padres,

Pascual Martínez de la Barrera

y

Maria Cruz Arias Aragón,

por ser la constante de este mundo tan variable.

Contents

List of Figures

List of Tables

Nomenclature

α	exponent of the scaling law between Nu_ω and Re (2.31)
β	exponent of the scaling law between λ_e and $\mathrm{C}_{\mathrm{PEO}}$ (3.5)
Δ	increment of a given parameter
η	radius ratio of the cylinders
$\bar{\varepsilon}$	total energy dissipation rate per mass $[\mathrm{W\cdot kg^{-1}}]$
ε_{bulk}	energy dissipation rate per mass in the bulk of the flow $[\mathrm{W\cdot kg^{-1}}]$
$\hat{\varepsilon}_{RB}$	dimensionless energy dissipation rate per mass in Rayleigh-Bénard flow
ε_{surf}	energy dissipation rate per mass in the surfaces $[\mathrm{W\cdot kg^{-1}}]$
ε_{wind}	convective or “wind” energy dissipation rate per mass $[\mathrm{W\cdot kg^{-1}}]$
$\hat{\varepsilon}_{wind}$	dimensionless convective or “wind” energy dissipation rate per mass
γ	surface tension $[\mathrm{N\cdot m^{-1}}]$
$\dot{\gamma}$	shear rate $[\mathrm{s^{-1}}]$
Γ	aspect ratio of the cylinders
λ_e	extensional relaxation time [s]
λ_C	Carreau relaxation time [s]
λ_v	radial viscous diffusion time [s]
λ_z	length of a pair of vortices with respect to the gap between cylinders
μ	dynamic viscosity $[\mathrm{kg\cdot m^{-1}\cdot s^{-1}}]$
μ_c	constant in the temperature dependence of the viscosity $[\mathrm{kg\cdot m^{-1}\cdot s^{-1}}]$
μ_s	solvent viscosity in a viscoelastic solution $[\mathrm{kg\cdot m^{-1}\cdot s^{-1}}]$
μ_p	contribution of the polymer to the total viscosity of a viscoelastic solution $[\mathrm{kg\cdot m^{-1}\cdot s^{-1}}]$
μ_v	volume viscosity $[\mathrm{kg\cdot m^{-1}\cdot s^{-1}}]$
μ_∞	viscosity when the shear rates tends to infinity $[\mathrm{kg\cdot m^{-1}\cdot s^{-1}}]$
μ_0	viscosity when the shear rates tends to zero $[\mathrm{kg\cdot m^{-1}\cdot s^{-1}}]$
ν	kinematic viscosity $[\mathrm{m^2\cdot s^{-1}}]$
∇	gradient operator $[\mathrm{m^{-1}}]$

$\nabla\cdot$	divergence operator [m^{-1}]
ω	azimuthal angular velocity [rad$\cdot$s^{-1}]
ω_i	rotation speed of the inner cylinder [rad$\cdot$s^{-1}]
ω_o	rotation speed of the outer cylinder [rad$\cdot$s^{-1}]
Ω	rotation speed of the inner cylinder [rad$\cdot$s^{-1}]
φ	azimuthal direction in a cylindrical coordinate system
σ	pseudo-Prandtl number
σ_p	standard deviation
ρ	density of the fluid [kg$\cdot$m^{-3}]
τ_v	dimensionless viscous time
$\bar{\bar{\tau}}$	stress tensor [Pa]
$\bar{\bar{\tau}}_s$	contribution of the solvent to the stress tensor [Pa]
$\bar{\bar{\tau}}_p$	contribution of the polymer to the stress tensor [Pa]
$\tau_{r\varphi}$	shear stress in φ direction and perpendicular to r [Pa]
ξ_{TC}	exponent of the scaling law between Nu_ω and Ta in Couette-Taylor flow (2.32)
ξ_{RB}	exponent of the scaling law between Nu and Ra in Rayleigh-Bénard convection
ζ	exponent in the relationship between the rescaled torque per number of diwhirls and the number of diwhirls (5.7)
$a_{1,2}$	constants in the relationship between Nu_ω and Re [18]
$A_{i,o}$	surfaces of the inner and the outer cylinder, respectively [m^2]
A	constant in the DiPrima relationship (4.1)
A$_e$	constant in the scaling law between λ_e and C$_{\mathrm{PEO}}$ [s] (3.5)
$\mathcal{A}$	pre-factor of the scaling law between Nu_ω and Re(2.31)
b	coefficient related to the temperature dependence of the viscosity [K^{-1}]
B	constant in the DiPrima relationship (4.1)
$\mathcal{B}$	constant in the relationship between the rescaled torque per number of diwhirls and the number of diwhirls (5.7)
c_1	constant in the relationship between $\mathcal{A}$ and Re (4.2)

c_2	constant in the relationship between $\mathcal{A}$ and Re (4.2)
C_I	constant in the relationship between the torque and the electrical current (3.1) [N·m·A^{-1}]
$\mathrm{C_{gly}}$	concentration of glycerol [%]
$\mathrm{C_{PEG}}$	concentration of poly(ethylene glycol) [%]
$\mathrm{C_{PEO}}$	concentration of poly(ethylene oxide) [ppm]
C_1	constant of the azimuthal speed of a laminar Couette flow (2.14)
C_2	constant of the azimuthal speed of a laminar Couette flow (2.14)
$\mathcal{C}$	constant in the relationship between the rescaled torque per number of diwhirls and the number of diwhirls (5.7)
CaBER	capillary breakup extensional rheometer
d	gap between cylinders [m]
D	diameter of a fluid filament during the extensional rheometry [m]
D_0	diameter of the plates of the CaBER [m]
E_k	kinetic energy per unit of mass [J·kg^{-1}]
El	elastic number
G	dimensionless torque
G_{lam}	dimensionless torque of a laminar Couette flow
G_1	constant related to the elasctic modulus of a viscoelastic solution [mPa]
H	height of the cylinders [m]
I	electrical current [A]
$\mathcal{I}_{i,o}$	contribution of the inner and outer cylinders in the energy dissipation rate in the surfaces of the cylinders [W·kg^{-1}]
IPA	isopropyl alcohol
J	conserved current of temperature in the Rayleigh-Bénard convection
J^{ω}	conserved transverse current of azimuthal motion [m^4· s^{-2}]
J^{ω}_{lam}	conserved transverse current of azimuthal motion of a laminar Couette flow [m^4·s^{-2}]
l	vortex length [m]
$\bar{l}$	average vortex length [m]

$\mathcal{L}$	azimuthal angular momentum per mass [$\mathrm{m}^2\cdot\mathrm{s}^{-1}$]
n	shear-thinning index
n_d	number of diwhirls
n_v	number of vortices
Nu	Nusselt number
Nu_ω	ω-Nusselt number
p	pressure [Pa]
P	injected power [W]
PDF	probability distribution function
PEG	poly(ethylene glycol)
PEO	poly(ethylene oxide)
q	axial wavenumber in the DiPrima relationship (4.1)
r	radial direction in a cylindrical coordinate system
r_i	inner cylinder radius [m]
r_o	outer cylinder radius [m]
$r_{1,2}$	radii of curvature of a drop in the Young-Laplace equation [m]
Ra	Rayleigh number
Re	Reynolds number
Re_c	critical Reynolds number
S	viscosity ratio
SPD	spectral power distribution
t	time [s]
^{T}	vector transpose operator
T	torque [N·m]
T_{lam}	torque of a laminar Couette flow [N·m]
$\mathcal{T}$	temperature [K]
Ta	Taylor number
$\vec{u}$	velocity field [$\mathrm{m}\cdot\mathrm{s}^{-1}$]
u_φ	azimuthal component of the velocity field [$\mathrm{m}\cdot\mathrm{s}^{-1}$]
u_r	radial component of the velocity field [$\mathrm{m}\cdot\mathrm{s}^{-1}$]

u_z	axial component of the velocity field [m·s^{-1}]
wt.%	weight percentage
V	volume enclosed between the cylinders [m^3]
W_i	Weissenber number
z	axial direction in a cylindrical coordinate system

Dimensionless numbers

η:	radius ratio of the cylinders	$\eta = \frac{r_i}{r_o}$
Γ:	aspect ratio of the cylinders	$\Gamma = \frac{r_i}{r_o}$
σ:	pseudo-Prandtl number	$\sigma = \frac{(1+\eta)^4}{(4\eta)^2}$
El:	elastic number	$El = \frac{\lambda_e}{\lambda_v} = \frac{Wi}{Re}$
G:	dimensionless torque	$G = \frac{T}{2\pi\rho\nu^2 H}$
G_{lam}:	dimensionless laminar torque	$G_{lam} = \frac{2\eta}{(1+\eta)(1-\eta)^2}\ Re$
Nu_ω:	ω-Nusselt number	$Nu_\omega = \frac{G}{G_{lam}}$
Re:	Reynolds number	$Re = \frac{\Omega r_i d}{\nu} = \dot{\gamma}\lambda_v$
Ta:	Taylor number	$Ta = \frac{1}{4}\frac{\sigma(r_o-r_i)^2(r_i+r_o)^2(\omega_i-\omega_o)}{\nu^2}$
Wi:	Weissenberg number	$Wi = \dot{\gamma}\lambda_e$

Chapter 1

Introduction

"You never get a second chance to make a first impression".

—Oscar Wilde

1.1 Brief review of the history of fluid mechanics

Fluid mechanics is the field of physics that studies the fluids, namely, liquids, gases and plasmas, by applying them the laws of force and motion. There are two branches: hydrostatics, which studies fluids at rest, and fluid dynamics, that deals with fluids in motion.

The first researches in fluid mechanics date from the ancient Greece, around 250 B.C., when Archimedes studied the buoyancy force in liquids and published his work entitled *On Floating Bodies*, considered as the first major work in the field. In the middle ages the Islamic physicist Al-Khazini invented the first known hydrostatic balance and presented it in *The book of Balance of Wisdom* (1121).

In the seventeenth and eighteenth centuries, there were many advances in Europe. The Italian Evangelista Torricelli, also known as the inventor of the barometer, explained several phenomena related to the motion of liquids in his treatise *De motu gravium naturaliter descendentium* (1644). The French Blaise Pascal published his researches about fluid statics in his treatise *Récit de la grande expérience de l'équilibre des liqueurs* (1648), where he showed the variation of the atmospheric pressure between the French city of Clermont and a nearby mountain called Puy-du-Dôme by using two glass cylinders filled with mercury. The English Isaac Newton published his investigations about the viscosity, after theoretical and experimental investigations of the fluid flowing between two parallel plates, in his *Philosiphiæ naturalis principia mathematica* (1687). More progress in fluid dynamics were made by the Swiss Daniel Bernoulli who studied the energy conservation in moving fluids and established the well known Bernoulli principle which states that a fluid exchanges its kinetic energy for pressure. He presented his results in his *Hydrodynamica seu de viribus et motibus fluidorum commentarii* (1738)

The nineteenth century was fruitful for the progress of fluid mechanics. The French Jean Léonard Marie Poiseuille and the German Gotthilf Heinrich Ludwig Hagen derived experimentally the laws that govern the liquid motion of very slow flows of high viscous fluid through pipes, like the blood that flows through the veins. The French Augustin Louis Cauchy derived the first differential equation of momentum in 1822, using the ideas of the Swiss Leonhard Euler. Around the same period, the most important equation in fluid mechanics, called the Navier-Stokes equation, was obtained independently by the French Claude-Louis Navier and the Irish George Gabriel Stokes. In 1858 the German Hermann von Helmholtz published a paper in which he explained the significance of the vorticity in fluid mechanics and science in general. Some years after, in 1869, the British William Thomson Kelvin published his researches setting the nowadays-called Kelvin's circulation theorem. At the end of this century the Irish Osborne Reynolds studied the condition under which the transition to turbulence occurs in pipe flow and used for the same time the now called Reynolds number in his article of 1883 [19].

In the twentieth century, the German Ludwig Prandtl investigated the flow close to the boundary layers and made the connection between the hitherto unconnected theories describing creeping flows and inviscid flows. The British Geoffrey Ingram Taylor advanced the understanding of fluid viscosity and turbulence and also helped in the development of supersonic aircraft. In 1941 the Soviet Andrey Nicolaevich Kolmogorov proposed a theory for isotropic turbulence, when the Reynolds number is large. He postulated that the smallest scale at which the turbulent energy is dissipated has to be *universal*, namely it does not depend on the large scales of the flow. Therefore, the smallest length and temporal scales of turbulence only depend on the viscosity and the energy dissipation rate.

The interested reader will be able to find more details about the history of fluid mechanics in “A history and philosophy of fluid mechanics” by G. A. Tokay or “The worlds of flow” by Olivier Darrigol.

1.2 The Couette-Taylor flow

Rotating flows are those which turn around a point, an axis or an object. These flows are observed in nature, for example, gases moving around stars, hurricanes or the rotating currents in oceans. They can also be found in many industrial processes, like the blood separators used to extract the plasma from the blood by centrifugation, the air entering in an aircraft turbine or the water that moves a turbine for electricity generation. These flows can even be found in daily life, like the coffee on a glass when it is stirred to dissolve the sugar, the water whirlpools created in sinks or the air around a spinning tennis ball.

A particular case of these rotating flows is when a fluid is confined between two coaxial differentially rotating cylinders. This type of flows is named the Couette-Taylor flow, after the French Maurice Marie Alfred Couette and the British Geoffrey Ingram Taylor. They were one of the firsts using this configuration in their investigations at the end of the nineteenth and the beginning of the twentieth centuries, respectively. Since it appearance, the Couette-Taylor flow has been one of the most investigated flow systems in fluid mechanics, because it is simple and easy to set an experimental model for shear flows. In addition, it is a closed system, so it is less sensitive to perturbations. Moreover, the global balances that relate the angular velocity to the energy dissipation can be obtained easily. From the standpoint of fundamental physics it is a rich system, since it presents multiple flow states, owing to the high non-linearity of the flow.

The Couette-Taylor system was first used in 1888 by Mallock [20] to determine the viscosity of water. Later, Couette [21] employed it as a viscosimeter. In 1917 Rayleigh [22] deduced a stability criterion for inviscid flows. Some years after, in 1923, Taylor [1] found that the laminar flow is linearly destabilised and replaced by axisymmetric steady toroidal vortices, called Taylor vortices. He established a criterion for the first appearance of instabilities depending on the rotation of both cylinders. Additionally, he calculated the velocity profile of these vortices for purely inner rotation and when both cylinders rotate. When a fluid tracer is added to the fluid, these Taylor vortices resemble donuts stacked around the inner cylinder. Figure 1.1(*a*) depicts the streamlines in a plane parallel to the common axis of the cylinder predicted by Taylor's analytical study and figure 1.1(*b*) shows a snapshot of the Taylor vortices. Chandrasekhar [23] studied analytically the hydrodynamics and the hydromagnetic instabilities in Couette-Taylor flows. Di Prima and Swinney performed an analitical study of Taylor vortices and wavy vortices [10]. Di Prima *et al.* [11] obtained an analytical expression to calculate the torque of laminar Taylor vortices as a function of the Taylor number and the radius ratio.

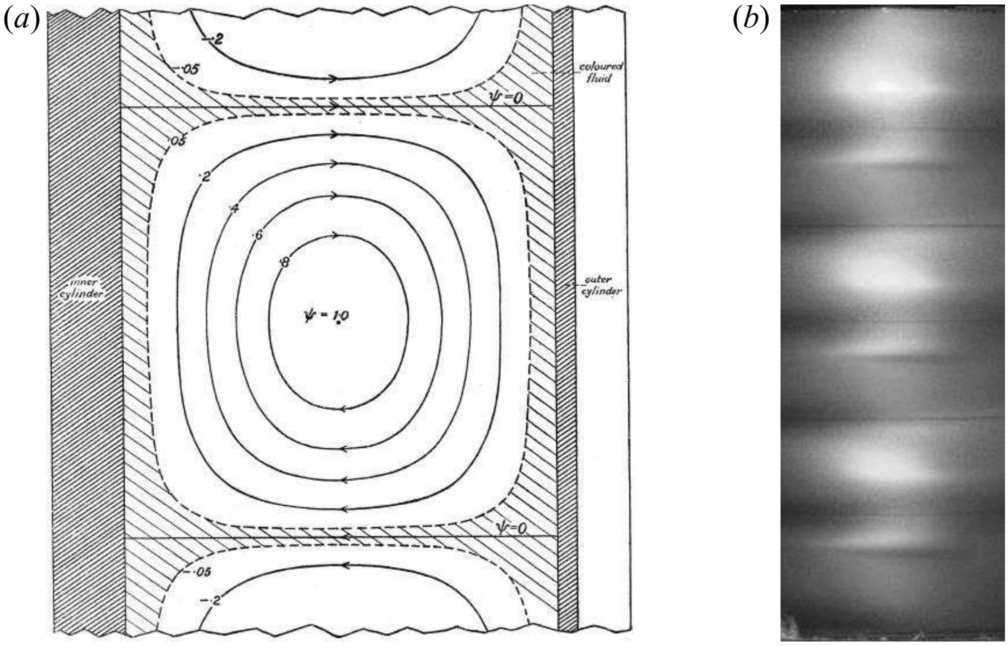

Figure 1.1: (*a*) Reproduction of Taylor's results [1]. Streamlines analytically predicted of a Taylor vortex when only the inner cylinder rotates. (*b*) Snapshot of a flow with 6 Taylor vortices.

Following the works just cited, important contributions to the understanding of this flow instability have been made by many authors. Stuart [24] did an analytical study of disturbances and energy transfer. Coles [25] studied the onset of turbulence and the multiple states in terms of axial and azimuthal wavenumber. Snyder [26] showed experimentally that the wavenumber is sensitive to the initial conditions and that its selection is a time-dependent process. Gollub and Swinney [27] performed a spectral analysis of the radial velocity to study the onset of chaos in the Couette-Taylor system. Barcilon *et al.* [28] proved the co-existence of Görtler vortices and Taylor vortices at high Taylor numbers in the turbulent regime. Koschmieder [29] measured the wavelentgh of turbulent Taylor vortices at high Taylor number in systems with two radius ratios and found that the wavelength strongly depends on the initial conditions in the case of narrow gap. Mullin and Benjamin [30] found that the annulus length has an effect on the stability of various steady cellular flows, in particular, a small length of the cylinders increases considerably the end effects. Benjamin and Mullin [31] demonstrated experimentally that a large number of states with distinct number of vortices can be found in a system with wide gap and that “anomalous mode” with odd number of vortices can arise. Andereck *et al.* [2] discovered a large variety of different flow states by rotating the inner and the outer cylinder for a system with $\eta = 0.883$ and $\Gamma = 30$ (see figure 1.2).

The torque has also been widely studied since Wendt [4] measured the torque for the first time in 1933 in a wide range of speeds, from laminar to turbulent flows. In 1936, Taylor [32] measured the torque in systems with several inner cylinders of different radii. Donnelly and Simon [18] obtained an empirical relationship between the torque of the Taylor vortex flow and the rotation speed of the inner cylinder. Nakabayashi *et al.* [33] analysed the effect of the surface roughness on the torque in transient and fully turbulent flow. In the case of purely inner rotation and turbulent flow, the effect of roughness only depends on the relative roughness and not in the Reynolds number. The recent studies dealing with torque measurements are presented in the following section.

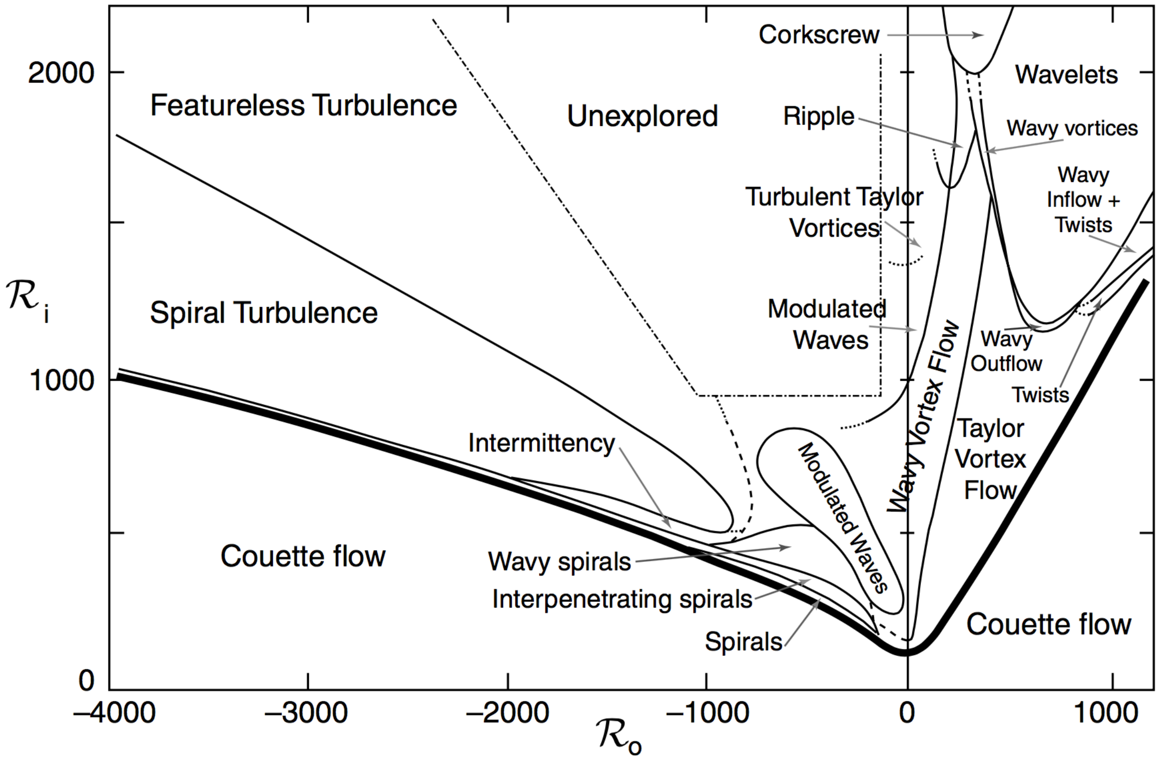

Figure 1.2: Reproduction of Andereck *et al.*'s results [2], redrawn by Cross and Greenside [3]. Regimes observed in Couette-Taylor flow depending on the rotating speed of the inner and outer cylinders in a system with $\eta = 0.883$ and $\Gamma = 30$.

1.3 Turbulent flows

Most of the flows present in Nature and in industrial applications are turbulent. Hence, there exists a great interest in the investigation of this kind of flows. The origin of turbulence is still unknown and it is a scientific challenge. However, the fundamental properties that characterise these flows are known. They are irregular and random, so, as they cannot be described from a deterministic point of view, they are treated using statistic methods. The momentum transfer diffusion is highly effective. Turbulence only appears if the Reynolds number is high, that is, the inertial forces are much larger than the viscous forces. They are three-dimensional and exhibit high levels of vorticity fluctuations. Actually, a turbulent flow can be visualised as a collection of vorticity tubes that are stretched because of the velocity fluctuations, and this process can only take place in three-dimensional flows. Turbulent flows are always dissipative, because the mechanical deformation work of the viscous stress increases the internal energy at the expense of the kinetic energy of the turbulent fluctuations. That is why this kind of flows needs a constant energy source to maintain the turbulence. And finally, the smallest scales of turbulence are larger than the molecular scales, so the fluctuations of the fluid properties, like the pressure, the density or the temperature, are associated to a continuous medium and governed by the Navier-Stokes equations. In addition, as turbulence is a consequence of the flow structure and not of the fluid, most of the dynamic properties of turbulent flows are the same for all the fluids, independently whether they are gases or liquids [34]. Then, the Couette-Taylor system can serve as a prototype to study turbulent flows in closed systems, since it is easy to set up, to control and to perform measurements.

Since the last three decades, turbulent flows and their energy dissipation have been again an important topic in the field of Couette-Taylor flows. Lathrop *et al.* [16] identified a transition from centrifugal to shear driven turbulence. Coughlin and Marcus [35] studied numerically the turbulent burst that appear in the flow before the onset of turbulence and described its dynamic behaviour. Takeda [36] measured the spatio-temporal velocity field of the flow and analysed the frequency spectrum to study the transition from laminar to turbulent flow. Batten *et al.* [37] studied numerically the transition to shear driven turbulence and showed that this transition occurs earlier for large radius ratios than for low ones. Racina and Kind [38] studied the dissipation of turbulent kinetic energy with the help of the particle image velocimetry (PIV). Bilson and Bremhorst [39] carried out direct numerical simulations (DNS) of turbulent flows and showed that the Taylor vortices transport the main part of the momentum transfer at Reynolds number below the transition to shear driven turbulence. Pirrò and Quadrio [40] showed using DNS that the fluctuations in turbulent flows have two main sources: the large-scale vortices and the near-wall shear. Dutcher and Muller [41] analysed the different transitions between the laminar Couette flow and the turbulent flow by means of spatio-temporal diagrams. Burin *et al.* [42] measured the angular momentum transport in a system with a short height and a wide gap, finding few differences with systems with longer heights and narrower gaps.

1.4 Motivations

As already exposed, one of the most important features of turbulent flows is the high energy dissipation. The energy injected in the fluid is transmitted from the large-scale structures to the smallest scales, where the viscous stresses dissipate the kinetic energy of the turbulent fluctuations and transform it in internal energy [34]. In a Couette-Taylor system the total energy injected in the fluid per unit of time, *i.e.*, the power injected, can be calculated multiplying the rotation speed of the cylinders by the applied torque. Therefore, it is clear that the use of torque measurement in these flows provides a fruitful information about the energy dissipation.

Dubrulle and Hersant [43] proposed an analogy between the heat transfer in turbulent Rayleigh-Bénard convection and the momentum transfer in turbulent Couette-Taylor flow. Eckhardt *et al.* [44] extended this analogy and demonstrated that the momentum transfer is directly related to the torque transmitted to the fluid. The demonstration will be explained later together with the connection to the torque measurements. In general, changes in the flow structure are accompanied by a variation of the momentum transfer. So, these changes can be detected from the torque measurements.

The main feature of Couette-Taylor flows is the presence of vortices due to the centrifugal forces. Therefore, these vortices should play an important role in the energy dissipation process and the momentum transfer. The present work focus on the dependence of the torque on the number of vortices and their size, and on the radius ratio.

Many of the flows encountered in industrial processes are not Newtonian. One particular case of non-Newtonain fluids are the viscoelastic solutions, which present both viscous and elastic properties. We will also focus on the torque measurement in viscoelastic solutions in the Couette-Taylor flow, where the turbulence appears at relatively small shear rates and exhibits large fluctuations, due to the elastic stresses.

Therefore, the main object of the present thesis is the development of an accurate technique for torque measurements in the Couette-Taylor system with Newtonian and viscoelastic solutions. The obtained data allow for a better understanding of features of the energy dissipation and the momentum transfer in Couette-Taylor flows

With this information, we have been able to analyse different flow features and the parameters that influence the energy dissipation and the momentum transfer in turbulent Couette-Taylor flows.

1.5 Manuscript structure

This manuscript is organised as follows. Chapter 2 present the theoretical background that holds the experimental work. Chapter 3 describes the experimental set-ups used during the experiments. Chapter 4 deals with torque measurements in turbulent Couette-Taylor flows. Chapter 5 deals with torque measurements in viscoelastic polymer solution. The manuscript ends in chapter 6 with the conclusions.

Chapter 2

Theoretical and experimental background of turbulent Couette-Taylor flows

"After a certain high level of technical skill is achieved, science and art tend to coalesce in aesthetics, plasticity and form. The greatest scientists are always artists as well".

—Albert Einstein

2.1 Equations of motion

The first basic law in fluid mechanics is that the total fluid mass in a closed volume is conserved. It is described by the continuity equation,

$$\frac{\partial \rho}{\partial t} + \nabla \cdot \rho \vec{u} = 0 \tag{2.1}$$

where ρ is the density of the fluid, t is the time, $\nabla \cdot$ is the divergence of a vector field and $\vec{u}$ is the velocity field. The first term of (2.1) represent the temporal variation of mass per unit of time, while the second term is the convective mass flux per unit of volume.

The momentum conservation principle, or Newton's second law of motion, applied to a fluid establishes that the variation of momentum contained in a fluid volume is equal to the sum of all the forces acting on it and is described using the momentum conservation equation. For Newtonian fluids, where the shear stress is proportional to the shear rate, this equation is called the Navier-Stokes equation, and is written as follows,

$$\frac{\partial \rho \vec{u}}{\partial t} + \nabla \cdot (\rho \vec{u}\vec{u}) = -\nabla p + \nabla \cdot \left[\mu(\nabla \vec{u} + \nabla \vec{u}^T)\right] + \nabla[(\mu_v - \frac{2}{3}\mu)\nabla \cdot \vec{v}] + \vec{F} \qquad (2.2)$$

where, ∇ is the gradient, p is the pressure, μ is the dynamic viscosity, ^{T} indicates the transpose of a vector, μ_v is the volume viscosity. The first term on the left side represents the local variation of momentum per unit of volume and the second one represents the momentum flux per unit of time. The first term on the right side includes the pressure forces per unit of volume, the second and the third ones represent the viscous forces related to the shear and the volumetric deformation per unit of volume and $\vec{F}$ is the sum of the external forces applied to the fluid [34]. When the flow velocity is small compared to the sound velocity in the fluid, the flow is considered incompressible ($\rho \approx$const) and it is governed by the following equations.

$$\begin{cases} \nabla \cdot \vec{u} = 0 \\ \dfrac{\partial \vec{u}}{\partial t} + (\vec{u} \cdot \nabla)\vec{u} = -\dfrac{1}{\rho}\nabla p + \nu \nabla^2 \vec{u} + \vec{F}/\rho \end{cases} \qquad (2.3)$$

where $\nu = \mu/\rho$ is the kinematic viscosity and is assumed to be constant.

We consider the flow motion of a Newtonian fluid between two concentric infinitely long cylinders which rotate around a common axis, *i.e.*, the Couette-Taylor flow (see figure 2.1). The inner cylinder of radius r_i rotates at the angular frequency ω_i and the outer cylinder of radius r_o rotates at the angular frequency ω_o. The flow occupies the gap between the cylinders, whose width is $d = r_o - r_i$ and whose hight is H. A cylindrical coordinate system is used and the common axis of the cylinders is chosen as the z-axis. Then, r and φ denote the radial and the azimuthal coordinates, respectively.

The velocity field, $\vec{u}(t; r, \varphi, z)$, can be decomposed in three perpendicular components: the azimuthal one, $u_\varphi(t; r, \varphi, z)$, the radial one, $u_r(t; r, \varphi, z)$, and the axial one, $u_z(t; r, \varphi, z)$. The azimuthal angular momentum per mass is $\mathcal{L}(t; r, \varphi, z) = r u_\varphi = r^2\omega$,

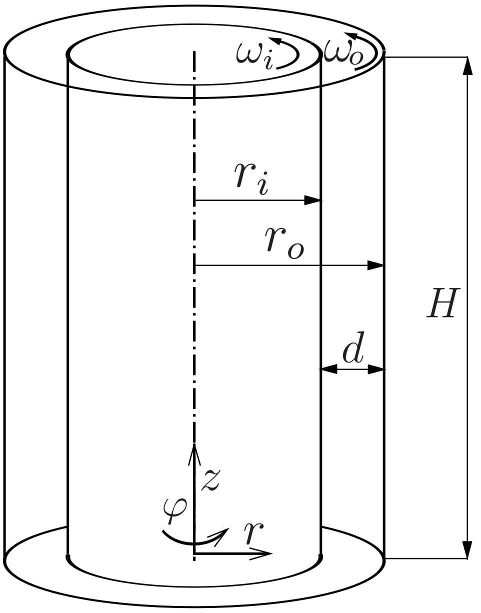

Figure 2.1: Design of the Couette-Taylor system.

where $\omega(t; r, \varphi, z)$ is the azimuthal angular velocity. The continuity equation reads,

$$\frac{1}{r}\frac{\partial}{\partial r}(r u_r) + \frac{1}{r}\frac{\partial u_\varphi}{\partial \phi} + \frac{\partial u_z}{\partial z} = 0 \tag{2.4}$$

and the Navier-Stokes equations for the flow motion in its three cylindrical components are,

$$\begin{aligned}&\frac{\partial u_r}{\partial t} + u_r\frac{\partial u_r}{\partial r} + \frac{u_\varphi}{r}\frac{\partial u_r}{\partial \varphi} - \frac{u_\varphi^2}{r} + u_z\frac{\partial u_r}{\partial z}\\ &= -\frac{1}{\rho}\frac{\partial p}{\partial r} + \nu\left[\frac{\partial}{\partial r}\left(\frac{1}{r}\frac{\partial}{\partial r}(r u_r)\right) + \frac{1}{r^2}\frac{\partial^2 u_r}{\partial \varphi^2} + \frac{\partial^2 u_r}{\partial z^2} - \frac{2}{r^2}\frac{\partial u_\varphi}{\partial \varphi}\right]\end{aligned} \tag{2.5}$$

$$\begin{aligned}&\frac{\partial u_\varphi}{\partial t} + u_r\frac{\partial u_\varphi}{\partial r} + \frac{u_\varphi}{r}\frac{\partial u_\varphi}{\partial \varphi} + \frac{u_r u_\varphi}{r} + u_z\frac{\partial u_\varphi}{\partial z}\\ &= -\frac{1}{\rho r}\frac{\partial p}{\partial \varphi} + \nu\left[\frac{\partial}{\partial r}\left(\frac{1}{r}\frac{\partial}{\partial r}(r u_\varphi)\right) + \frac{1}{r^2}\frac{\partial^2 u_\varphi}{\partial \varphi^2} + \frac{\partial^2 u_\varphi}{\partial z^2} + \frac{2}{r^2}\frac{\partial u_r}{\partial \varphi}\right]\end{aligned} \tag{2.6}$$

$$\begin{aligned}&\frac{\partial u_z}{\partial t} + u_r\frac{\partial u_z}{\partial r} + \frac{u_\varphi}{r}\frac{\partial u_z}{\partial \varphi} + u_z\frac{\partial u_z}{\partial z}\\ &= -\frac{1}{\rho}\frac{\partial p}{\partial z} + \nu\left[\frac{1}{r}\frac{\partial}{\partial r}\left(r\frac{\partial u_z}{\partial r}\right) + \frac{1}{r^2}\frac{\partial^2 u_z}{\partial \varphi^2} + \frac{\partial^2 u_z}{\partial z^2}\right].\end{aligned} \tag{2.7}$$

The velocity components satisfy the no-slip boundary conditions at the cylinders walls, *i.e.*,

$$\begin{cases} u_r = u_z = 0 \quad \text{at} \quad r = r_i,\ r = r_o \\ u_\varphi = \omega_i r_i \quad \text{at} \quad r = r_i \\ u_\varphi = \omega_o r_o \quad \text{at} \quad r = r_o \\ \vec{u} = 0 \quad \text{at} \quad z = 0,\ z = H \end{cases} \tag{2.8}$$

The conditions for u_φ at $z = 0$, $z = H$ depend on the way that the endplates are attached to the Couette-Taylor system.

In fluid mechanics, it is very common to use the dimensionless analysis for two main reasons. On the one hand, it allows to know the minimum number of variables that govern a given problem, reducing the initial physical variables to a smaller group of dimensionless parameters. This enables to set accurately the conditions that should be fulfilled to the existence of similitude between two flow systems; *i.e.*, the dimensionless number must be the same. Therefore, the dimensionless solution of both systems is the same. Then, the physical solutions of the problems can be obtained by undoing the change in the variables using the characteristic magnitudes of each problem. On the other hand, the use of dimensional analysis is important because it provides the relevance of a given variable in the problem, just guessing if its dimensionless value is large or small to know whether the variable influences the dynamics or not [34]. The Couette-Taylor system can be characterised by four dimensionless control parameters: the radius ratio $\eta = r_i/r_o$, which is related to the flow mean curvature $\bar{d} = d/\bar{r} = 2(1-\eta)/(1+\eta)$; the aspect ratio $\Gamma = H/d$; the rotation ratio ω_o/ω_i; and the Reynolds number of the inner cylinder, which represents the ratio between inertial forces to viscous forces, and is defined as

$$Re = \frac{\omega_i r_i d}{\nu}. \tag{2.9}$$

In our study, the outer cylinder is fixed ($\omega_o = 0$), so there are three independent control parameters. The Reynolds number and the curvature can be combined to define the Taylor number as follows,

$$Ta = \frac{1}{4}\frac{\sigma(r_o - r_i)^2(r_i + r_o)^2(\omega_i - \omega_o)^2}{\nu^2}, \tag{2.10}$$

where it is introduced the pseudo-Prandtl number, defined as

$$\sigma = \frac{(1+\eta)^4}{(4\eta)^2}. \tag{2.11}$$

The relationship between Re and Ta, when $\omega_o = 0$, is the following,

$$Ta = \frac{\sigma^2}{[(1+\eta)/2]^2} Re^2 \tag{2.12}$$

2.1.1 Base flow

Let consider the laminar Couette flow between two infinitely long cylinders which rotate independently. The flow is stationary (time independent), axisymmetric ($\partial/\partial\varphi = 0$) and invariant along the the cylinder axis ($\partial/\partial z = 0$). Then, there is only molecular transport of azimuthal angular momentum, $\mathcal{L}$. From the continuity equation, the axial and radial components u_r and u_z are identically zero and the azimuthal component u_φ only depends on the radial component. The base flow equations are,

$$\begin{cases} \rho \dfrac{u_\varphi^2}{r} = -\dfrac{dp}{dr} \\ \dfrac{d}{dr}\left(\dfrac{1}{r}\dfrac{d}{dr}(ru_\varphi)\right) = 0 \end{cases}, \tag{2.13}$$

where the first equation is the balance between the centrifugal force and the radial pressure gradient. The boundary conditions (2.8) lead to the azimuthal velocity of the base flow,

$$u_\varphi(r) = \frac{C_1}{r} + C_2 r \quad , \quad \text{where} \quad C_1 = \frac{(\omega_i - \omega_o) r_i^2}{1-\eta^2} \quad \text{and} \quad C_2 = \frac{\omega_o - \eta^2 \omega_i}{1-\eta^2}. \tag{2.14}$$

The angular momentum $\mathcal{L}(r) = ru_\varphi = C_1 + C_2 r^2$. The viscous stress tensor $\bar{\bar{\tau}}$ has only shear component,

$$\tau_{r\varphi} = -\mu\left(\frac{\partial u_\varphi}{\partial r} - \frac{u_\varphi}{r}\right) = \frac{2C_1\mu}{r^2}. \tag{2.15}$$

In the case where only the inner cylinder rotates, the laminar torque acting on the inner cylinder surface over the height H is,

$$T_{lam} = 2\pi r_i H \tau_{r\varphi} r_i = 4\pi r_i^2 H \mu \frac{\omega_i}{1-\eta^2}. \tag{2.16}$$

The characteristic torque for a cylindrical annulus of fluid with kinematic viscosity ν is $T_\nu = 2\pi\rho\nu^2 H$, which is related to the molecular transport due to viscosity. This allows to define the dimensionless torque expressed as,

$$G_{lam} = \frac{T_{lam}}{2\pi\rho\nu^2 H} = \frac{2\eta}{(1+\eta)(1-\eta)^2} Re. \tag{2.17}$$

2.1.2 Theory of Eckhardt, Grossmann and Lohse

A theory to establish an analogy between the momentum transfer in Couette-Taylor flow and the heat transfer in Rayleigh-Bénard convection was recently developed by Eckhardt, Grossmann and Lohse [44] in 2007. The Rayleigh-Bénard system consists on two parallel plates displaced perpendicular to a gravity field an put at different temperatures. If the lower plate is hotter, heat is transferred from the lower to the upper plate. The flow becomes unstable at a given Rayleigh number, Ra (the analogue of the Taylor number in Couette Taylor flow), which is proportional to the temperature difference imposed on the plates. The idea was to obtain the same set of equations as in Rayleigh-Bénard system that could lead to the same scaling laws in the turbulent regime. The goal of this analogy is to demonstrate that the turbulence mechanisms in high turbulent flows are the same independently of the system. Here below, the different dimensionless parameters are derived from the flow equations.

Let consider a Couette-Taylor flow, beyond the Couette laminar regime, where the velocity field is time dependent and has the three components. In this case, the transport of azimuthal angular momentum, $\mathcal{L}$, is both molecular and convective. To derive the azimuthal conserved current, the equation (2.6) is averaged over a cylindrical surface co-axial with the cylinders area $A(r) = 2\pi r H$, where $r_i \leq r \leq r_o$. The average is defined as,

$$\langle X \rangle_A = \int X \frac{r d\varphi dz}{2\pi r H} = \int \frac{dz}{H} \int X \frac{d\varphi}{2\pi}, \tag{2.18}$$

The terms containing φ vanish. Then, if a time average is also performed, one gets

$$\left\langle u_r \frac{\partial u_\varphi}{\partial r} + \frac{u_r u_\varphi}{r} + u_z \frac{\partial u_\varphi}{\partial z} - \nu \left[\frac{1}{r} \frac{\partial u_\varphi}{\partial r} - \frac{u_\varphi}{r^2} + \frac{\partial^2 u_\varphi}{\partial r^2} \right] \right\rangle_{A,t} = 0. \tag{2.19}$$

The continuity equation allows to eliminate the derivative with respect to z, in fact the term

$$\left\langle u_z \frac{\partial u_\varphi}{\partial z} \right\rangle_{A,t} = \left\langle \frac{\partial (u_z u_\varphi)}{\partial z} - u_\varphi \frac{\partial u_z}{\partial z} \right\rangle_{A,t} = \left\langle u_\varphi \frac{\partial u_r}{\partial r} + \frac{u_\varphi u_r}{r} \right\rangle_{A,t} \tag{2.20}$$

If this is introduced in (2.19), it is obtained

$$\left\langle \frac{\partial (r^2 u_r u_\varphi)}{\partial r} - \nu \left[\frac{1}{r} \frac{\partial u_\varphi}{\partial r} - \frac{u_\varphi}{r^2} + \frac{\partial^2 u_\varphi}{\partial r^2} \right] \right\rangle_{A,t} = 0 \tag{2.21}$$

Now, if (2.21) is multiplied by r^2, and taking into account that $\omega = u_\varphi / r$, the following expression is obtained,

$$\frac{\partial}{\partial r} \left(r^3 \left[\langle u_r \omega \rangle_{A,t} - \nu \frac{\partial \langle \omega \rangle_{A,t}}{\partial r} \right] \right) = 0 \tag{2.22}$$

Therefore, the quantity inside the parenthesis is independent of r, *i.e.*, a quantity that has the same value for any cylindrical surface $A(r)$ in the flow domain $r_i \leq r \leq r_o$. The constant

$$J^\omega = r^3 \left[\langle u_r \omega \rangle_{A,t} - \nu \frac{\partial \langle \omega \rangle_{A,t}}{\partial r} \right] \tag{2.23}$$

is interpreted as the conserved transverse current of azimuthal motion, which transports $\omega(t; r, \varphi, z)$ in the radial direction. Actually, the dimension of J^ω is $[J^\omega] = \mathrm{m}^4\mathrm{s}^{-2} = [\mathcal{L}^2] = [\nu^2]$. The quantity J^ω is the analogue of the conserved current of temperature, J, in Rayleigh-Bénard convection. J^ω evaluated in the inner cylinder at $r = r_i$ is

$$J^\omega |_{r=r_i} = -r_i^3 \nu \frac{\partial \omega}{\partial r} |_{r=r_i}. \tag{2.24}$$

Then, using (2.15), the shear stress evaluated in the inner cylinder at $r = r_i$ is

$$\tau_{r\varphi} = -\mu r_i \frac{\partial \omega}{\partial r}|_{r=r_i}. \tag{2.25}$$

The combination of (2.24) and (2.25) yields the variation between the shear stress and J^{ω},

$$\tau_{r\varphi} = \rho r_1^{-2} J^{\omega}. \tag{2.26}$$

So, the torque can be expressed as,

$$T = 2\pi r_i H \tau_{r\varphi} r_i = 2\pi \rho H J^{\omega}. \tag{2.27}$$

Therefore, measuring the torque T acting on the inner cylinder yields the value of J^{ω}. The dimensionless torque,

$$G = \frac{T}{2\pi\rho\nu^2 H} = \frac{J^{\omega}}{\nu^2}. \tag{2.28}$$

is the ratio between the conserved transverse current of azimuthal motion, J^{ω}, to the purely molecular. The conserved transverse current of azimuthal motion for a Couette laminar flow is

$$J^{\omega}_{lam} = 2\nu C_1 = 2\nu r_i^2 \frac{\omega_i - \omega_2}{1-\eta^2}. \tag{2.29}$$

In analogy with the heat transport in Rayleigh-Bénard convection, where the Nusselt number, Nu, compares the heat transfer in the turbulent regime with the heat transfer in the conduction regime, Dubrulle and Hersant [43] and then Eckhardt *et al.* [44] defined the quasi-Nusselt number on Couette-Taylor flow,

$$Nu_{\omega} = \frac{J^{\omega}}{J^{\omega}_{lam}} = \frac{G}{G_{lam}}. \tag{2.30}$$

which is the ratio of the conserved transverse current of azimuthal motion to the molecular transport in a laminar but not yet transversely convective flow.

The evolution of the torque of a turbulent flow with the rotation speed of the inner cylinder can be expressed as a scaling law,

$$Nu_\omega = \mathcal{A}Re^{\alpha-1}, \tag{2.31}$$

where $\mathcal{A}$ is the pre-factor and α is the exponent. A rigorous analogy between Rayleigh-Bénard convection and Couette-Taylor flow exists between Ra and Ta, so the scaling of the torque should be expressed as follows,

$$Nu_\omega = \bar{\mathcal{A}}Ta^{\xi_{TC}}, \tag{2.32}$$

where $\xi_{TC} = (\alpha - 1)/2$. In the turbulent Rayleigh-Bénard convection, the Nusselt number is given by Grossmann and Lohse [45], and the scaling law of the heat convection is expressed as,

$$Nu \propto Ra^{\xi_{RB}}. \tag{2.33}$$

If the turbulent Couette-Taylor flow and the turbulent Rayleigh-Bénard convection had the same universal behaviour, both exponent would be the same, $\xi_{TC} = \xi_{RB}$, indicating that the mechanisms of turbulence are similar.

The total energy dissipation rate per mass in a Couette-Taylor flow can be easily calculated if the torque and the rotation speed of the inner cylinder are known, so,

$$\bar{\varepsilon} = \frac{\text{torque} \times \text{rotation speed}}{\text{mass}} = \frac{T\ \Omega}{2\pi(r_o^2 - r_i^2)H\rho} = \frac{J^\omega\ \Omega}{(r_o^2 - r_i^2)} \tag{2.34}$$

The energy dissipation per mass can be also deduced from the equations of motion. First, the r-, φ-, and z-components of the Navier-Stokes equations, (2.5),(2.6) and (2.7), are multiplied by u_r, u_φ and u_z, respectively. If the the resulting equations are grouped, it is obtained,

$$\begin{gathered}\frac{\partial\left(\vec{u}^2/2\right)}{\partial t} + \left(u_r\frac{\partial}{\partial r} + \frac{u_\varphi}{r}\frac{\partial}{\partial\varphi} + u_z\frac{\partial}{\partial z}\right)\left(\frac{\vec{u}^2}{2} + p\right) = \\ \nu\left(u_r\nabla^2 u_r + u_\varphi\nabla^2 u_\varphi + u_z\nabla^2 u_z - \frac{u_2^2 + u_\varphi^2}{r^2} + \frac{2u_\varphi}{r^2}\frac{\partial u_r}{\partial\varphi} - \frac{2u_r}{r^2}\frac{\partial u_\varphi}{\partial\varphi}\right)\end{gathered} \tag{2.35}$$

An average over the total volume of the fluid, V, can be defined as,

$$\langle X \rangle_V = \frac{1}{V} \int dr \int dz \int X r d\varphi. \tag{2.36}$$

If (2.35) is averaged over the flow volume and using the divergence theorem, also know as the Gauss-Ostrogradsky theorem, one obtains the equation of the variation of the kinetic energy as,

$$\begin{aligned} &\frac{dE_k}{dt} = \left\langle \frac{\vec{u}^2}{2} \right\rangle_V = \\ &\nu \left\langle \left(u_r \nabla^2 u_r + u_\varphi \nabla^2 u_\varphi + u_z \nabla^2 u_z - \frac{u_2^2 + u_\varphi^2}{r^2} + \frac{2u_\varphi}{r^2} \frac{\partial u_r}{\partial \varphi} - \frac{2u_r}{r^2} \frac{\partial u_\varphi}{\partial \varphi} \right) \right\rangle_V \end{aligned} \tag{2.37}$$

The terms of this equation can be rearranged by splitting the dissipation terms as follows,

$$(\vec{u} \cdot \nabla^2)\vec{u} = \nabla \cdot \left(\nabla \frac{\vec{u}^2}{2} + (\vec{u} \cdot \nabla)\vec{u} \right) - \frac{1}{2} \left(\frac{\partial u_i}{\partial x_j} + \frac{\partial u_j}{\partial x_i} \right)^2 \tag{2.38}$$

where $\partial / \partial x_{i,j}$ are the derivative in the cylindrical coordinates. The equation (2.37) yields

$$\frac{dE_k}{dt} = \nu \left\langle \nabla \cdot \left(\nabla \frac{\vec{u}^2}{2} + (\vec{u} \cdot \nabla)\vec{u} \right) \right\rangle_V - \nu \left\langle \frac{1}{2} \left(\frac{\partial u_i}{\partial x_j} + \frac{\partial u_j}{\partial x_i} \right)^2 \right\rangle_V . \tag{2.39}$$

The first term in the right side of (2.39) corresponds to the energy introduced in the fluid volume through the surfaces due to the viscous no-slip condition. Using again the divergence theorem we can transform the volume integral in a surface integral, using a closed surface, as,

$$\varepsilon_{surf} = \nu \left\langle \nabla \cdot \left(\nabla \frac{\vec{u}^2}{2} + (\vec{u} \cdot \nabla)\vec{u} \right) \right\rangle_V = \frac{\nu}{V} \oint_A \left(\nabla \frac{\vec{u}^2}{2} + (\vec{u} \cdot \nabla)\vec{u} \right) d\vec{A}. \tag{2.40}$$

The second term on the right side of (2.39) corresponds to the dissipation rate in the bulk of the flow, given by,

$$\varepsilon_{bulk} = \frac{\nu}{2} \left\langle \left(\frac{\partial u_i}{\partial x_j} + \frac{\partial u_j}{\partial x_i} \right)^2 \right\rangle_V . \tag{2.41}$$

Hence, the total variation of kinetic energy can be written as,

$$\frac{dE_k}{dt} = \varepsilon_{surf} - \varepsilon_{bulk} \tag{2.42}$$

Now, the surface integral will be developed. The dissipation rate at the surfaces can be computed as,

$$\begin{gathered}\varepsilon_{surf} = \frac{\nu}{V}\oint_A \left(\nabla\frac{\vec{u}^2}{2} + (\vec{u}\cdot\nabla)\vec{u}\right) d\vec{A} = \\ \frac{\nu}{V}\left[A_o\left\langle\frac{\partial}{\partial r}\frac{\vec{u}^2}{2} + ((\vec{u}\cdot\nabla)\vec{u})_r\right\rangle_{A_o} - A_i\left\langle\frac{\partial}{\partial r}\frac{\vec{u}^2}{2} + ((\vec{u}\cdot\nabla)\vec{u})_r\right\rangle_{A_i}\right] = \mathcal{I}_o - \mathcal{I}_i\end{gathered}, \tag{2.43}$$

being $\mathcal{I}_o$ and $\mathcal{I}_i$ the contributions of the surfaces of outer and the inner cylinders, respectively. If the terms inside the brackets are developed, taking into account that $u_\varphi = r\omega$ and that the surfaces are $A_i = 2\pi H r_i$ and $A_o = 2\pi H r_o$, one gets the following expression,

$$\mathcal{I}_o - \mathcal{I}_i = \frac{2\nu}{r_o^2 - r_i^2}\left[\left(r^3\omega\frac{\partial\omega}{\partial r}\right)_{r_o} - \left(r^3\omega\frac{\partial\omega}{\partial r}\right)_{r_i}\right]. \tag{2.44}$$

Taking into account the definition of J^ω (2.23), one obtains,

$$\mathcal{I}_o - \mathcal{I}_i = -\frac{2(\omega_o - \omega_i)}{r_o^2 - r_i^2}J^\omega. \tag{2.45}$$

So, the temporal variation of kinetic energy in the turbulent flow is,

$$\frac{dE_k}{dt} = \mathcal{I}_o - \mathcal{I}_i - \varepsilon_{bulk}. \tag{2.46}$$

In the mechanical equilibrium,

$$\varepsilon_{bulk} = \mathcal{I}_o - \mathcal{I}_i = \varepsilon_{surf}. \tag{2.47}$$

In the case of a laminar Couette flow, where $J^\omega = J^\omega_{lam}$,

$$\varepsilon_{surf,lam} = \nu\frac{r_i^2 r_o^2}{(r_o^2 - r_i^2)^2}\left(\frac{\omega_i - \omega_o}{d}\right)^2 \tag{2.48}$$

In the case of a flow beyond the laminar Couette regime, the increase of energy dissipation rate due to transverse convection between the cylinders is given by the convective or "wind" dissipation rate per unit of mass,

$$\varepsilon_{wind} = \varepsilon_{surf} - \varepsilon_{surf,lam} = \frac{2(\omega_i - \omega_o)}{r_o^2 - r_i^2}(J^\omega - J^\omega_{lam}). \tag{2.49}$$

If this is expressed in terms of Nu_ω, σ and Ta, the following expression is obtained,

$$\varepsilon_{wind} = \frac{\nu^3}{d^4}\frac{Ta}{\sigma^2}(Nu_\omega - 1), \tag{2.50}$$

which shows that the scale of the energy dissipation is ν^3/d^4. From this expression the significance of σ can be interpreted as follows. The pseudo-Nusselt number be also rewritten as,

$$\sigma = \frac{\nu}{r_i^2 r_o^2/(r_i + r_o)^4}, \tag{2.51}$$

where the quantity $r_i^2 r_o^2/(r_i + r_o)^4$ can be interpreted as a viscosity due to the curvature of the system, or the inverse of a resistance to the vorticity transfer in radial direction. The larger is the gap, the larger is σ, so $r_i^2 r_o^2/(r_i + r_o)^4$ decreases. The dimensionless expression of the "wind" dissipation rate is,

$$\hat{\varepsilon}_{wind} = \frac{Ta}{\sigma^2}(Nu_\omega - 1). \tag{2.52}$$

This exact relationship between the energy dissipation rate and the ω-current of the ω-Nusselt number in the Coutte-Taylor is the analogue of the relationship between the energy dissipation and the Nusselt number in turbulent Rayleigh-Bénard convection, which is given by

$$\hat{\varepsilon}_{RB} = \frac{Ra}{Pr^2}(Nu - 1). \tag{2.53}$$

That is why σ is called the pseudo-Prandtl number in Couette-Taylor flow and Ta is the analogous driving force in Couette-Taylor flow to Ra in Rayleigh-Bénard convection.

2.2 Torque in turbulent states

The theory from Eckhardt *et al.* [44] proves that the torque measurements can provide fruitful informations about the flow features, particularly, the energy dissipation and the momentum transfer. In addition to the radius ratio, η, there are other parameters that have an influence on the level of torque, and hence, on the energy dissipation of turbulent flows. Numerous investigations have been carried out in the last two decades to study the parameter space associated to the torque of turbulent flows. Here below, the different works dealing with the torque are presented.

Wendt [4] was the first who measured the torque in turbulent Couette-Taylor flows. In figure 2.2 the evolution of the torque divided by the torque of the laminar Couette flow, Nu_ω, as a function of the Reynolds number, Re, is depicted. At low Re the flow is laminar, so the momentum transport is done by viscous diffusion and $Nu_\omega = 1$. Then, once a critical Reynolds number is reached, the vortices appear in the flow. Systems with different inner radii, $r_i = 4.70$, 2.20 and 0.95 cm, corresponding to $\eta = 0.935$, 0.85 and 0.68, present different level of torque.

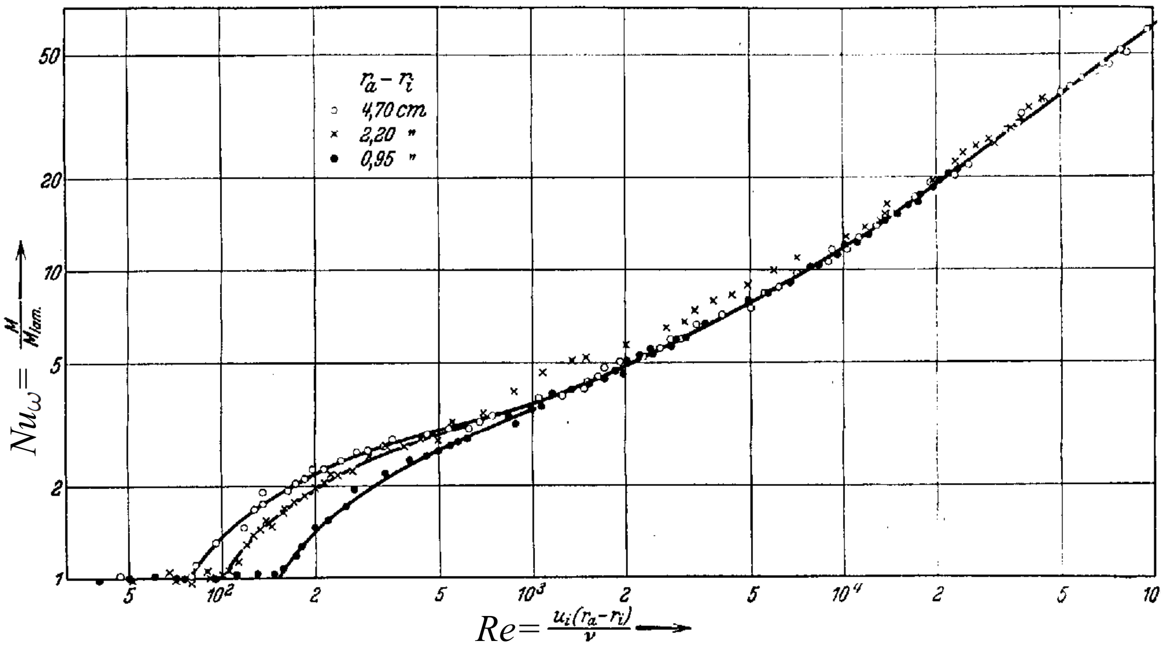

Figure 2.2: Reproduction of Wendt's results [4]. Torque divided by the laminar torque as a function of the Reynolds number

Lathrop *et al.* [5, 16] found a transition from centrifugal to shear driven turbulence in a system with $\eta = 0.725$ by analysing their torque measurements and demonstrated that the mechanisms of energy dissipation change after this transition. Figure 2.3(a) reproduces the results of the evolution G with Re and shows a clear change in the slope of the curve at $Re \approx 10^4$, which becomes steeper after the transition. Figure 2.3(b) shows the evolution of the exponent α of the scaling laws with Re. Different behaviours α are observed before and after the transition at $Re \approx 10^4$, which increase progressively once the transition is attained. Following this work, Lewis and Swinney [6] detected a crossing of the torque-speed curves for turbulent flows with different numbers of vortices around the transition to shear driven turbulence at $Re = 13\ 000$. Figure 2.4 reproduces their results where they showed that the level of torque before the transition of a flow with 10 vortices is higher than of a flow with 8 vortices. After the transition, the flow with larger number of vortices presents lower torque. This means that the role of the vortices become less important after this transition. Actually, Bilson and Bremhorst [39] found in their numerical simulations that the vortices transport the main part of the momentum transfer before the transition.

Dubrulle *et al.* [46] performed an analysis of the control parameters in turbulent Couette-Flow, also finding a change in the slope of the $Nu_\omega(Re)$ curves when only the inner cylinder rotates. They interpreted it as a transition to the "ultimate (universal) regime" of turbulence, in analogy with Rayleigh-Bénard convection, in which energy dissipation proceeds independently of initial conditions. In this regime, the torque should vary like Re^2 and do not depend any more on the molecular viscosity, like in the Kolmogorov theory for developed turbulence at large Reynolds numbers, as Doering and Constatin [47] exposed.

Ravelet *et al.* [14] carried out a study of turbulent flows in a system with $\eta = 0.917$, focusing on the scaling of the torque with the Reynolds number. Again, they found a change in the slope of the torque-speed curve at $Re \approx 10\ 000$, probably related to the transition to the ultimate regime. A change in the behaviour of the exponent α was also found after this transition.

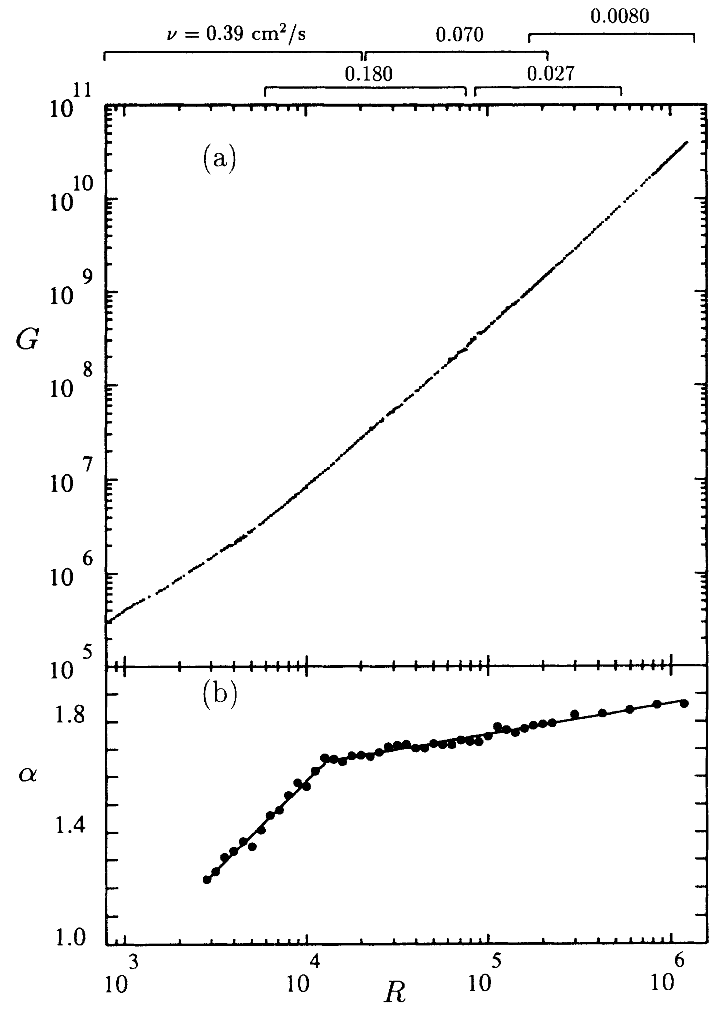

Figure 2.3: Reproduction of Lathrop *et al.*'s results [5]. (a) Evolution of the dimensionless torque G as a function of the Reynolds number, R. (b) Evolution of the exponent α as a function of R.

Paoletti and Lathrop [48] studied the torque in a Couette-Taylor system with $\eta = 0.725$ and independently rotating cylinders, finding a maximum in the dimensionless torque G when the ratio between the inner and the outer cylinder rotations speed is $\omega_o/\omega_i = -0.33$.

Following the work of Eckhardt *et al.* [44], van Gils *et al.* [49] investigated flows at $Re = \mathcal{O}(10^6)$ in a system with $\eta = 0.717$ to reach the ultimate regime. They established that this ultimate regime is attained once the boundary layers of the cylinders become turbulent, like in the Rayleigh-Bénard convection. They found an exponent $\alpha = 1.88$

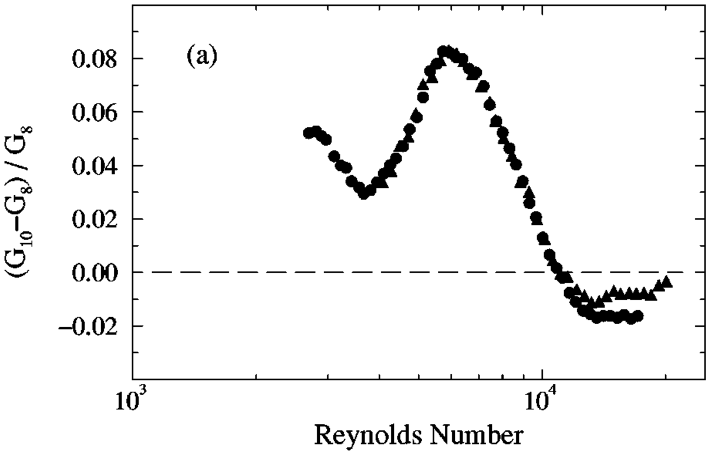

Figure 2.4: Reproduction of Lewis and Swinney's results [6]. Evolution of the difference in torque between a 10-vortex flow, G_{10}, and a 8-vortex flow, G_8, as a function of the Reynolds number.

at the highest Re they reached. Additionally, they found a maximum in the rescaled torque Nu_ω when counter rotating the cylinders at $\omega_o/\omega_i = -0.31$. Huisman *et al.* [17] measured the properties of the boundary layer using particle image velocimetry and found a logarithmic profile, typical of turbulent boundary layers, at $Re \approx 25\ 000$, indicating that the ultimate regime is reached. Focusing in the number of vortices present in the flow, Huisman *et al.* [50] found multiple states in strongly turbulent flows at $Re = \mathcal{O}(10^6)$, questioning Kolmogorov's paradigm about the uniqueness of turbulence at high Reynolds numbers. Finally, in the framework of the present work, we published the results of our investigations [9] related to the effect of different numbers of vortices in the torque of Couette-Taylor flows. Nine different states with different numbers of vortices were found. The $Nu_\omega(Re)$ curves corresponding to these states intersect close to the transition to the ultimate regime at $Re \approx 13\ 000$. These results will be developed in chapter 4.

From a numerical point of view, several groups have been able to simulate turbulent Couette-Taylor flows up to relatively high Re. Most of the investigations used periodic boundary conditions with relatively short calculation domains. Ostilla-Mónico *et al.* [51] presented the effect of three- and four-vortex pairs on the dimensionless transport, suggesting that the increase of the number of vortex pairs induces an increase in torque.

Brauckmann and Eckhardt [12] investigated the effect of the vortex size on the torque and found a maximum of torque for vortices of axial wavelength of 1.93 times the gap width for $Re = 5000$. Both results confirm those of Lewis and Swinney [6] about the influence of the number of vortices in the torque.

Ostilla-Mónico *et al.* [8, 52, 7] analysed the parameter space of turbulent Couette-Taylor flow, focusing on the momentum transfer, and also investigated the transition to the ultimate regime. Figure 2.5(a) shows the evolution of $Nu_\omega - 1$ with Ta for three radius ratios, η=0.5, 0.714 and 0.909. The dashed lines represent the slope of the $Nu_\omega(Ta)$ in logarithmic scale once the ultimate regime is attained. Actually, this is equal to $(\alpha - 1)/2$, where α is the exponent of the scaling law. Hence, $\alpha = 1.88$ and 1.76 for $\eta = 0.909$ and 0.5, respectively. As previously observed [16, 6, 49], the exponent increases smoothly once the ultimate regime is reached. Moreover, the systems with $\eta = 0.909$ and 0.714 present larger levels of torque than the one with $\eta = 0.5$. Figure 2.5(b) illustrates the transition between different regimes in the (Ta,η) parameter space. The dashed line represents the threshold of the transition to the ultimate regime. For $\eta > 0.714$, the transition is independent of Ta, but for $\eta < 0.714$, the threshold is shifted to higher values of Ta when η decreases.

Figure 2.6 depicts the compensated torque Nu_ω versus Taylor number, Ta, for $\eta = 0.909$ and three different vortex wavelength, λ_z. Here λ_z is length of a pair of vortices compared to the gap in between cylinders, where $\lambda_z = 2$ is equivalent to circular vortices. The simulations (DNS) of four different λ_z: 1.5, 2.09, 3.00 and 4.00, are compared with the experimental results of Ostilla-Mónico *et al.* [8] and our results [9]. Both in experiments and in numerics, different branches associated to different states cross at $Ta \approx 2 \times 10^8$, shown as a vertical dashed line in the graphic.

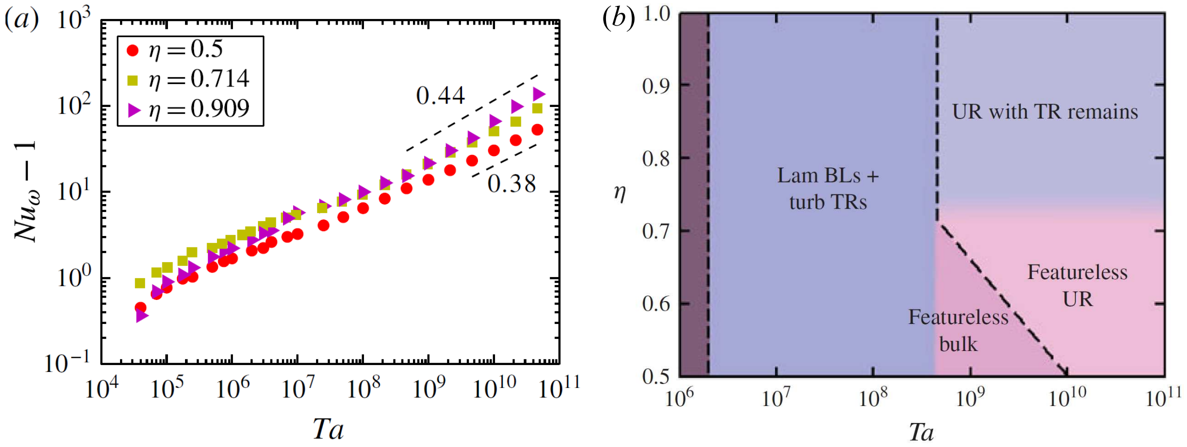

Figure 2.5: Reproduction of Ostilla-Mónico *et al.*'s results [7]. (*a*) Rescaled torque $Nu_\omega - 1$ versus Taylor number, Ta, for different radius ratios, η. (*b*) Transition between different regimes in the (Ta,η) parameter space. The dashed line represents the threshold of the transition to the ultimate regime. Abbreviation: boundary layer (BL), Taylor rolls (TR), ultimate regime (UR).

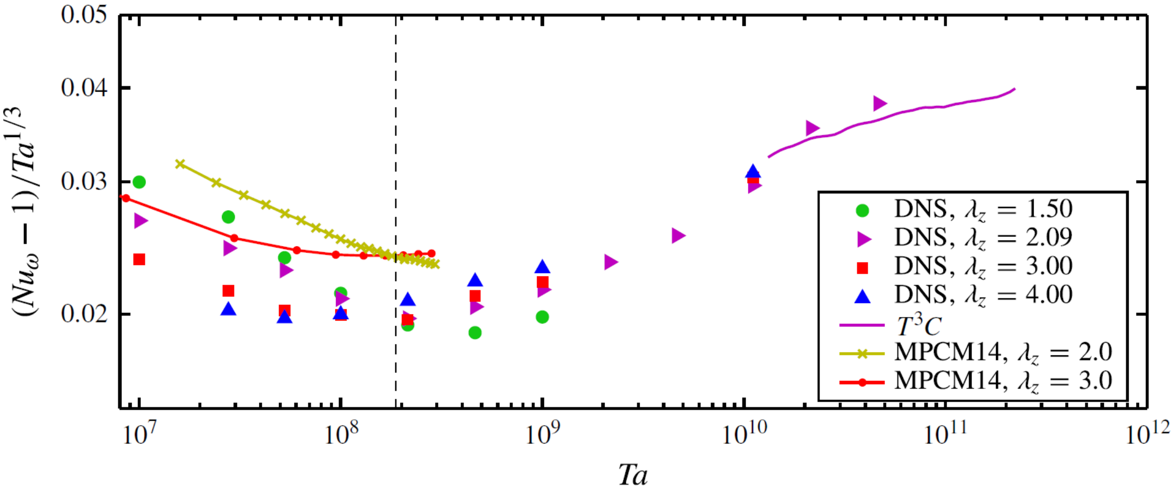

Figure 2.6: Reproduction of Ostilla-Mónico *et al.*'s results [7]. Compensated torque Nu_ω versus Taylor number, Ta, for $\eta = 0.909$ and three different vortex wavelength, λ_z. Experimental data for the T^3C system with $\Gamma = 46.35$ [8] and from Martínez-Arias *et al.* [9] in a system with $\Gamma = 30$ (denoted MPCM14, $\lambda_z = 2$ corresponds to 30 rolls and $\lambda_z = 3$ corresponds to 18 rolls). The vertical dashed line corresponds to the transition to the ultimate regime.

Chapter 3

Experimental set-ups

"In physical science a first essential step in the direction of learning any subject is to find principles of numerical reckoning and practicable methods for measuring some quality connected with it. I often say that when you can measure what you are speaking about, and express it in numbers, you know something about it; but when you cannot measure it, when you cannot express it in numbers, your knowledge is of a meagre and unsatisfactory kind; it may be the beginning of knowledge, but you have scarcely in your thoughts advanced to the stage of science, whatever the matter may be".

—William Thomson Kelvin

In order to analyse the energy dissipation quantitatively in Couette-Taylor flow, the torque has to be measured accurately. For this purpose, the devices and fluids used have been carefully selected to optimise the torque measurements. This chapter presents the three set-ups and the fluids employed for the experiments. The Couette-Taylor systems used are presented in §3.1. The rheology of the working fluids employed is explained in §3.2. Finally, §3.3 deals with reflective particles used for visualisations.

3.1 Couette-Taylor systems

3.1.1 Couette-Taylor system on rheometer

This facility consists on a Couette-Taylor cell fitted on a rheometer (Physica MCR 501 from Anton Paar). A photography of the rheometer and a sketch of the Couette-Taylor cell are depicted in figures 3.1(*a*) and (*b*). There is an outer cylinder with a radius of $r_o = 55.00 \pm 0.01$ mm. Cylinders with different radii can be fitted on the head of the rheometer. Three cylinders with radii of $r_i = 53.50$, 50.00 and 33.00 ± 0.01 mm have been used. Hence, the gap between the outer and the inner cylinders are $d = r_o - r_i = 1.50$, 5.00 and 22.00 ± 0.01 mm, respectively. The height of the inner cylinders is of $H = 150.0 \pm 0.5$ mm. The radius ratios are $\eta = r_i/r_o = 0.973$, 0.909 and 0.6, and the aspect ratios are $\Gamma = H/d = 100$, 30 and 6.82, respectively. Figure 3.2 illustrates the three configurations drawn to scale. The rheometer is able to apply a torque, T, while measuring the angular speed of the inner cylinder, Ω. It is also possible to control the speed through a control loop. The maximum rotation speed that the cylinders can attain is 10 Hz. Note that the outer cylinder is always stationary

The inner cylinders are made of aluminium and their surfaces are anodised. The bottom of the cylinders is recessed. There is a gap of 0.500 ± 0.001 mm between the edge of the base of the inner cylinder and the flat bottom of the outer cylinder filled with an air bubble, which minimises the shear stress on the bottom of the cylinders. The top part of the gap between the two cylinders is covered with an annular PVC lid. It is positioned so that the bottom of the lid is at the same height as the upper edge of the inner cylinder. This makes the gap to be completely filled with liquid and there is no contact between the lid and the inner cylinder. The outer cylinder is made of glass and there is an additional glass jacket filled of circulating water from a thermostat in order to maintain the working temperature at 22.00 ± 0.05°C. The room temperature is fixed at the same temperature to prevent heat fluxes between the ambient and the working fluids.

Most of the previous works dealing with torque measurement of turbulent flows

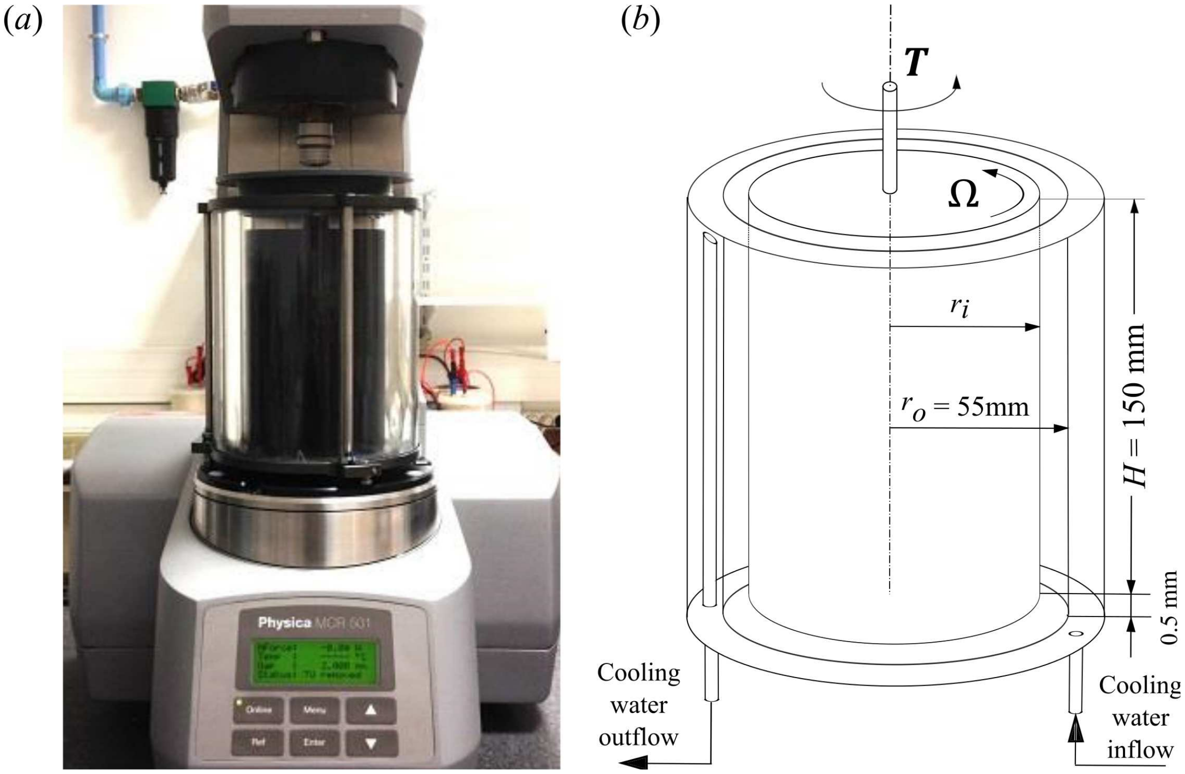

Figure 3.1: Rheometer Physica MCR 501 from Anton Paar and Couette-Taylor cell. (*a*) Photograph of the rheomter with the Couette-Taylor cell fitted. (*b*) Sketch of the Couette-Taylor cell.

employed techniques based on torque bearing [16, 14] or torque sensing strain arms [49, 13]. The rheometer used here controls the torque, which is proportional to the electric current. The purpose of using a rheometer is to take simultaneously accurate torque and rotation speed measurements, in a wide range of rotation speed. By selecting an appropriate fluid, torque measurements, both for laminar Couette flow and turbulent flow, can be done. While in other systems the torque is measured in the centre of the inner cylinder, with the present system the torque is measured for the whole height of the inner cylinder, including the end effects.

The rheometer contains a synchronous brushless electronically commutated motor powered by a direct current electric source via an integrated inverter/switching power supply. The advantage of using a direct current electric source lies on the direct proportionality between the torque that the motor applies and the electrical current that

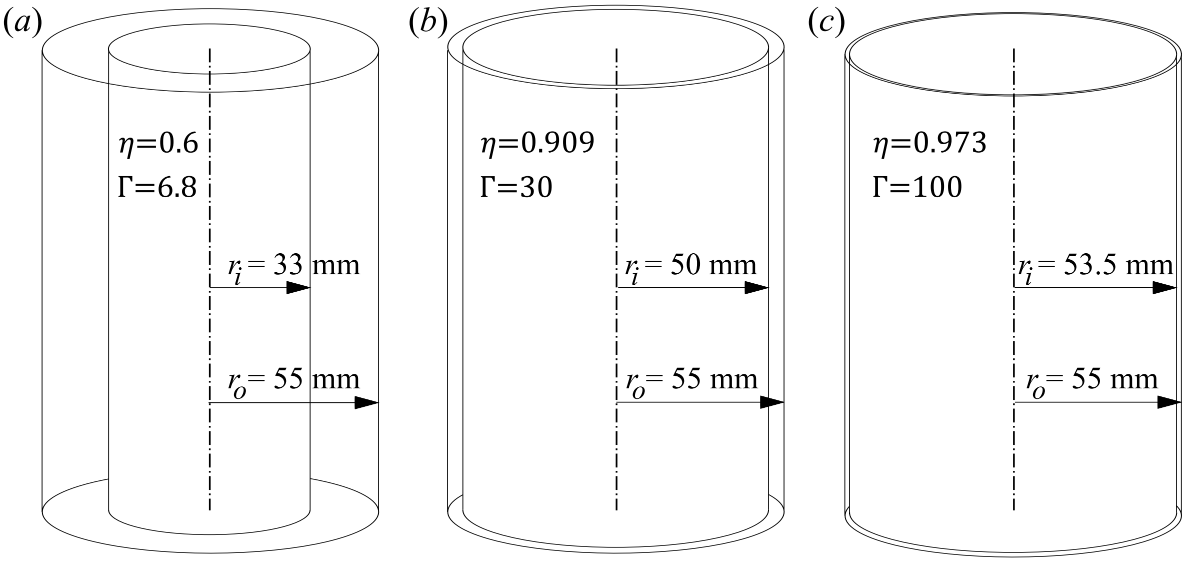

Figure 3.2: Sketches drawn to scale of the different configurations . (*a*) configuration with $\eta = 0.6$ and $\Gamma = 6.85$. (*b*) configuration with $\eta = 0.909$ and $\Gamma = 30$. (*c*) configuration with $\eta = 0.973$ and $\Gamma = 100$.

feeds it. So,

$$T = C_I I \tag{3.1}$$

where T is the torque and C_I depends both on the length of the conductors that drive the electrical current, I, which feeds the motor, and the density of the magnetic field generated by the magnets of the motor. Hence, the torque can be controlled accurately and in a simple way by adjusting the electrical current. To minimise the friction of the motor, the rheometer contains a high-precision air bearing. Thanks to this construction, the accuracy of the torque is 0.5% of the measured value and never smaller than $0.2\,\mu\mathrm{N}\cdot\mathrm{m}$. In addition, the rheometer allows for torque- or speed-controlled runs operated by a real-time control system with a maximum acquisition frequency of 100 Hz and a real resolution of the optical incremental encoder smaller than 1 µrad. In the case when running an experiment in torque control mode, a constant torque is applied to the inner cylinder, since the electrical current that the motor receives is constant. When running an experiment in speed control mode, the real-time control system adjust the torque that is needed to keep the rotation speed constant. The fluids employed in each experiment were selected to optimise the torque or speed acquisitions. The advantage of using the Couette-Taylor cell fitted to a rheometer is that it is small, light and easy to handle. Hence, after every experiment it is unmounted, what allows to clean the cell and renew the fluid for every test. This guarantees that the properties of the fluids are always the same and no trace of other substances is present.

3.1.2 CoGeoF3 Taylor-Couette system

This Couette-Taylor facility is in the Laboratory of Aerodynamics and Fluid Mechanics of the Brandenburg Technical University of Cottbus, Germany [13], and has been used to complement our investigations of turbulent flows in a wide gap. Figure 3.3(a) and (b) show a photograph and a sketch of the device, respectively. The inner and the outer cylinder radii are $r_i = 35$ mm and $r_o = 70$ mm, respectively. Hence, the gap between the two cylinders is $d = r_o - r_i = 35$ mm. The length of the inner cylinder is $L = 700$ mm. Consequently, the dimensionless parameters that describe the geometry are the radius ratio $\eta = r_i/r_o = 0.5$ and the aspect ratio $\Gamma = L/d = 20$. This facility is able to control the speed of the inner cylinder, Ω, while measuring the torque, T.

The inner cylinder is made of aluminium and its surface is anodised. In order to measure the torque, two strain gauges are placed in the internal wall of the inner cylinder. The gauges are calibrated, so each angular deformation of the cylinder is associated to a given torque. The strain gauges give reliable values up to $2\,\mathrm{N}\cdot\mathrm{m}$, although the measured values never exceed $0.5\,\mathrm{N}\cdot\mathrm{m}$. The frequency acquisition is 100 Hz. The effective measuring length of the inner cylinder is 5/7 of the total length. Therefore, the torque acting on the 100 mm closest to the bottom and top ends are not measured, thus the end effects do not affect the torque measurements. The temperature of the system is measured through a sensor placed inside the inner cylinder. The inner cylinder is driven by an electrical motor. The speed of the motor is regulated using a variable-frequency drive, which is adjusted through a computer. Bearings of different sizes and belts are used in the kinematic chain between the electrical motor and the inner cylinder, so the motor works in an optimal regime.

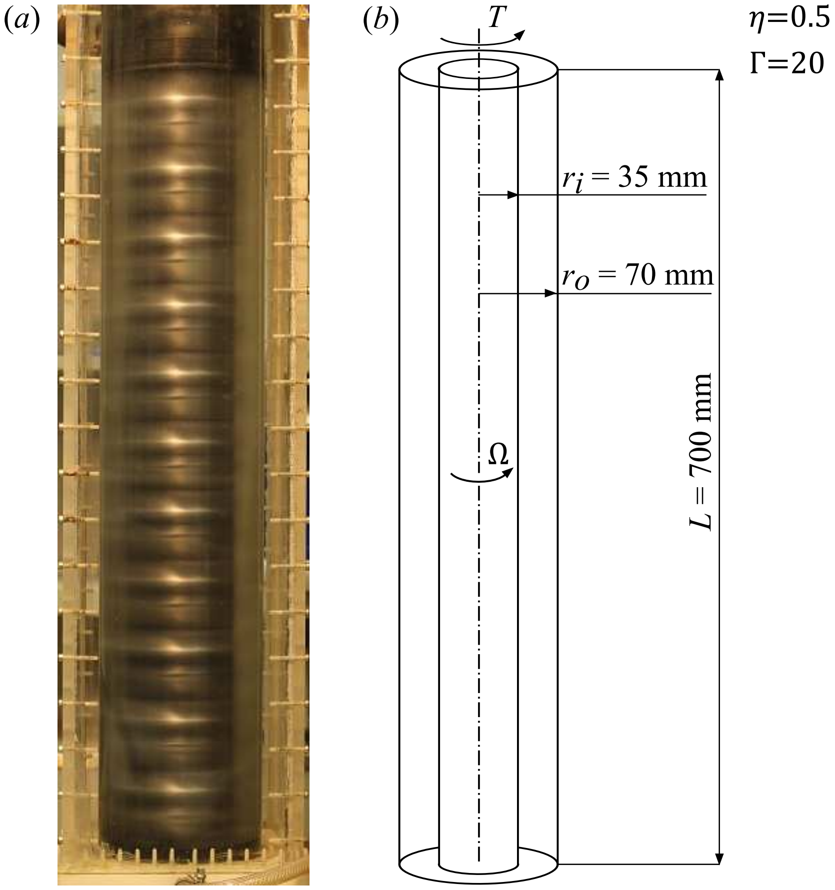

Figure 3.3: CoGeoF3 Couette-Taylor system. (*a*) Photograph of the facility. (*b*) Sketch of the system, drawn to scale.

3.2 Rheology of working solutions

3.2.1 Newtonian solutions

Several Newtonian fluids have been used depending on the goal of each experiment. To reach high Reynolds numbers in turbulent flows, low viscous fluids were employed. In the case of laminar flows at low Reynolds numbers, high viscous fluids were employed to maximise the torque level. Below, the Newtonian fluids used are presented together with their properties.

Demineralised water is obtained from a resin-filtering system and then it is degassed. Its properties are obtained from Kestin *et al.* [53] and Wagner *et al.* [54]. Mixtures of demineralised water and pure glycerol 99%, obtained from *Acros Organics*, in different concentrations were used to obtain high viscous Newtonian fluids. Both substances are degassed before mixing. In table 3.1 the values of the density, ρ, and the dynamic viscosity, μ, for all the glycerol concentrations, C_{gly}, used during the experiments are presented at the working temperature of 22°C. The values obtained from the measurements are compared with previous studies [55] finding a good agreement. Since glycerol is an organic substance and degrades in time, the solutions were prepared everyday for each experiment. The density has been measured using a density-meter Anton Paar DMA 35. The viscosity has been measured using a rolling-ball viscosimeter Anton Paar AMVn for viscosities under 10 m Pa s and the rheometer Anton Paar MRC 501 with a cone and plate geometry of 50 mm of diameter and an angle of 0.5° for fluids with viscosities above 10 m Pa s.

C_{gly} (wt.%)	ρ (kg/m^3)	μ (mPa.s)
0	997.8	0.954
25	1058.3	1.936
50	1125.4	5.543
70	1179.8	20.370

Table 3.1: Density and viscosity of water-glycerol solutions for different concentrations of glycerol at 22°C.

A low viscous silicon oil (Polydimethylsiloxane 0.65 cSt, Aldrich) was used as a Newtonian fluid, because it has a lower viscosity than water and thus higher Reynolds numbers can be reached. Its density is equal to 764 kg/m^3 and its kinematic viscosity equal to 0.65×10^{-6} m^2/s at a temperature of 22°C.

A high viscous silicon oil was used as a Newtonian fluid in the CoGeoF3 to prevent corrosion. The variation of its density, ρ, and its dynamic viscosity, μ, with the temperature, $\mathcal{T}$, have been measured using a viscosimeter Anton Paar SVM 3000 and are displayed in figure 3.4. A linear model and an Arrhenius model were tried to fit the variation of the dynamic viscosity with the temperature, although the results were not satisfactory. Then, an empirical exponential fitting in the form: $\mu = \mu_c e^{(-b\mathcal{T})}$, was tried, as the range of temperature is small, $\Delta\mathcal{T} = 15$ K. Here, $\mu_c = \mu(\mathcal{T} = 0) = 15.23\,\text{kg}\,\text{m}^{-1}\,\text{s}^{-1}$

and $b = 18.30 \times 10^{-3}\ K^{-1}$ is a coefficient related to the temperature dependence of the viscosity. The fitting is plotted as a continuous line in figure 3.4.

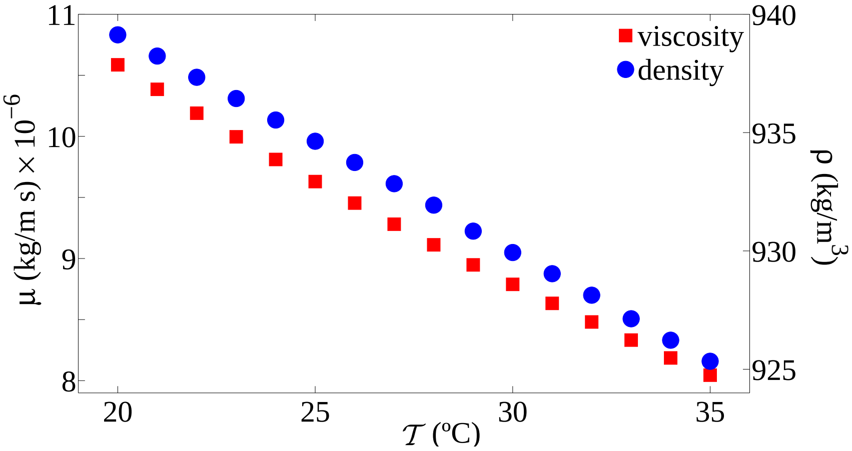

Figure 3.4: Variation of dynamic viscosity, μ, and density, ρ, of the silicon oil AK10 with the temperature, $\mathcal{T}$. The continuous line corresponds to an empirical exponential fitting of μ.

3.2.2 Viscoelastic polymer solutions

Viscoelastic fluids have been used to study the effect of elasticity on the flow. There is a large variety of polymers and the present study considers mixtures of water, poly(ethylene glycol) (PEG), poly(ethylene oxide) (PEO) in different concentrations and isopropyl alcohol (IPA). A Capillary Breakup Extensional Rheometer (CaBER) has been used to determine its elastic properties. This nonionic polymer has the simplest structure among water-soluble polymers. Its chemical structure: $\mathrm{H-(O-CH_2-CH_2)_n-OH}$ allows an aqueous dissolution in a wide range of concentrations and a large number of macromolecular conformations. The properties of aqueous PEO solutions and mixtures of PEO and PEG are well documented [56, 57, 58, 59, 60, 61, 62, 63, 64, 65]. The polymers were provided by Sigma Aldrich. The PEG is a polymer with relatively short linear chains whose molar mass is 20 000 g mol^{-1}. The PEO is a high-molecular-weight polymer with long linear chains whose molar mass is 8 000 000 g mol^{-1}. Initially, different concentrations of PEG in water were tested and the viscosity and density of the solutions were measured. Figure 3.5 shows the variation of the kinematic viscosity,

ν, and the density, ρ, with the concentration of PEG, C_{PEG}, of different solutions. A concentration of 7 wt.% of PEG was selected because it is considered as dilute [66] and it allows to trigger the first instability in Couette-Taylor flow at low rotation speed of the inner cylinder with a sufficiently high level of torque. When this concentration of PEG is combined with PEO concentrations of 76, 100, 150, 300 and 1000 ppm, a suitable compromise between viscosity and elasticity is obtained. The combination of these concentrations covers a dilute to semi-dilute regime [64]. The density of the mixture is the same for all the concentrations and is equal to 1 009 ± 1 kg/m^3.

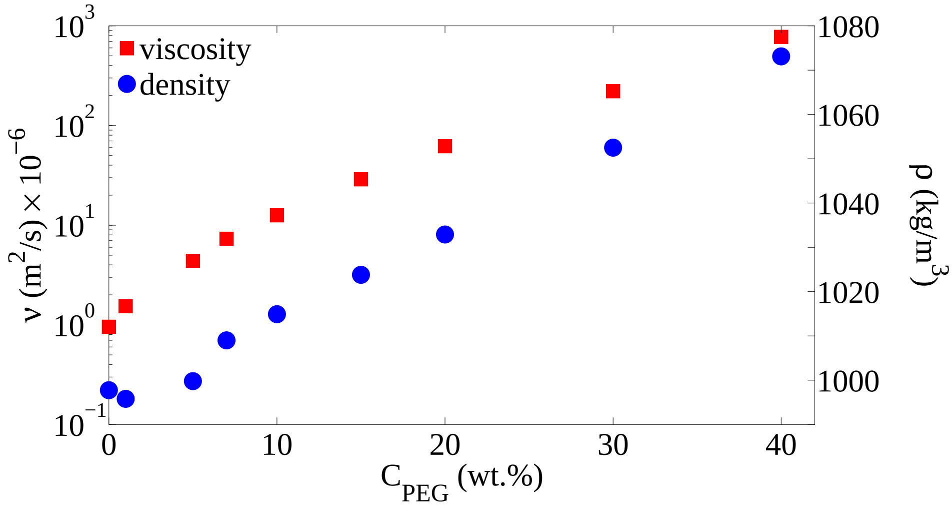

Figure 3.5: Variation of the kinematic viscosity, ν, and the density, ρ, with the concentration of PEG, C_{PEG}, of mixtures of water and PEG.

All fluids were prepared in batches of 1 kg and the protocol [67, 64] is as follows. In one vessel, PEG flakes were dropped in water and the mixture was stirred gently until complete dissolution. In another vessel, PEO powder was mixed in 5 g of IPA and poured into water without being stirred. Both vessels were stored at 5°C during 72 hours. Then, the solutions were mixed and gently stirred. After that, the fluid remained at room temperature, 22°C, during four hours before the experimental runs. A photograph of the fluid filament formed by a solution with a concentration of 1000 ppm of PEO is displayed in figure 3.6.

For measuring the shear viscosity, μ, a bob-cup geometry was installed, having the bob a radius of 13.330 ± 0.001 mm, the cup a radius of 14.460 ± 0.001 mm and the gap a

Figure 3.6: Photograph of the fluid filament formed in an aqueous solution of 7 wt.% of PEG and 1000 ppm of PEO. The diameter of the stick is 8 mm.

length of 40.006±0.001 mm. In figure 3.7(*a*) a sketch of the bob-cup geometry is shown. The values of the shear viscosity, μ, as a function of the shear rate, $\dot{\gamma}$, are presented in figure 3.7(*b*). As the concentration of PEO increases, the shear viscosity increases, but remains constant with respect to the shear rate. In the case of the solution with 1000 ppm of PEO, the shear thinning is significant and the shear viscosity can be fitted using a Carreau model,

$$\mu = \mu_\infty + (\mu_0 - \mu_\infty)[1 + (\lambda_C \dot{\gamma})^2]^{(n-1)/2} \tag{3.2}$$

where μ_0 is the viscosity when $\dot{\gamma}$ tends to zero, μ_∞ is the viscosity when $\dot{\gamma}$ tends to infinity, λ_C is the Carreau relaxation time and n is the shear-thinning index. Here $\mu_0 = 33.5$ mPa.s, $\mu_\infty = 18.1$ mPa.s, $n = 0.7$ and $\lambda_s = 1.62$ s. The curve $\mu(\dot{\gamma})$ that fits the points is represented in figure 3.7(b) as a red continuous line, and is used to assess the viscosity at different shear rates, $\dot{\gamma}$, for 1000 ppm.

3.2.3 Capillary Breakup Extensional Rheometry

A capillary breakup extensional rheometer (HAAKE CaBER 1 from Thermo Scientific) is used to measure the capillary thinning of a fluid filament joining two circular plates after a stretching [68, 69]. An image of the rheometer is shown in figure 3.8(*a*). The

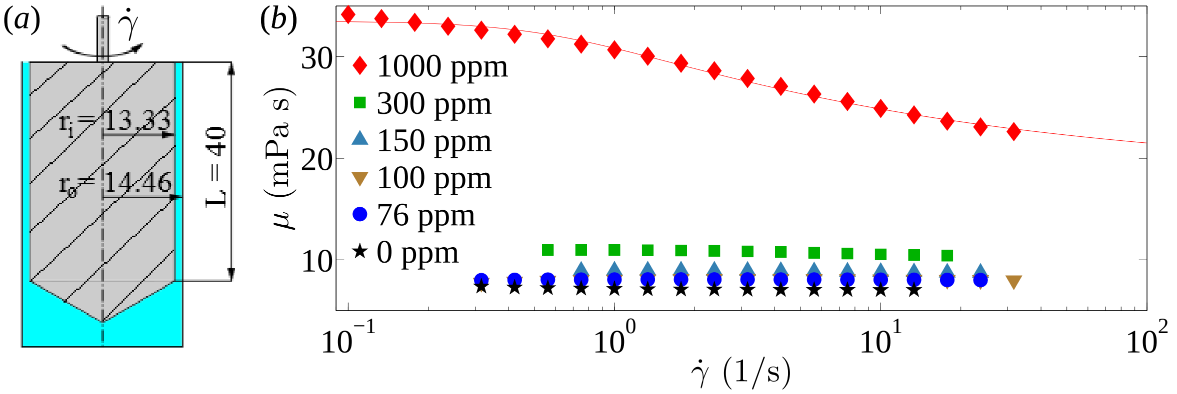

Figure 3.7: (*a*) Sketch of the bob-cup geometry installed in the rheomter for measuring the shear viscosity. All the dimensions are in mm. (*b*) Shear viscosity, μ, as a function of the shear rate, $\dot{\gamma}$, for different concentrations of PEO of $M_w = 8 \times 10^6$ g/mol dissolved in 7% PEG aqueous solution. The red continuous line corresponds to a fitting by the Carreau model.

extensional relaxation time can be deduced from the thinning speed of the filament. This technique was used to characterise the elastic behaviour of the viscoleastic fluids used in chapter 5. Figure 3.8(*b*) displays an image of the plates before and after the stretching. Figure 3.8(*c*) illustrates a sketch of the plates. The diameter of the plates is $D_0 = 6$ mm and they are initially separated by 3 mm. The final distance of the plates is 11.6 mm after the stretching. It works as follows. A sample of fluid is placed between the circular parallel plates. Then, if the gap, the diameter, the density of the fluid and its surface tension are well selected, a capillary bridge will form [70]. At time $t = -50$ ms the top end plate is moved upward to reach a final position at $t = 0$. The displacement profile can be linear or logarithmic. A linear profile is used. The evolution of the fluid filament diameter, $D(t)$, is monitored at the midplane between the end plates using a laser micrometer. It is possible to vary the sampling rate, which is fixed at 1000 Hz in the tests. The spatial resolution is 8 µm, so any variation of the filament diameter below this value can not be detected.

Figure 3.9 (*a*) presents the evolution of the normalised midplane diameter of the filament, $D(t)/D_0$, as a function of time for viscoelastic solutions containing water, 7 wt.% of PEG and PEO in different concentrations. Figure 3.9(*b*) shows snapshots at

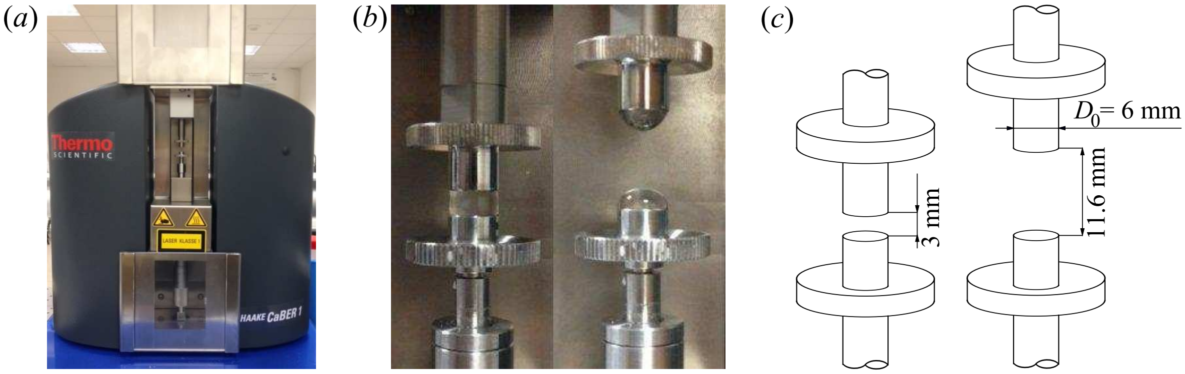

Figure 3.8: Capillary breakup extensional rheometer (CaBER). (*a*) Frontal image of the apparatus. (*b*) Photographs of the plates before and after stretching. (*c*) Sketch of the plates before and after stretching.

different increasing times, in intervals of 0.5 s, of the fluid filament formed between the plates of the CaBER after the stretching by a solutions containing 7 wt.% of PEG and 300 ppm of PEO. In the first instant, after the stretching of the plates, the gravity force is predominant and the diameter decreases rapidly until reducing its initial value 10 times. After this, in the case of the Newtonian fluid, with 0 ppm of PEO, the diameter still reduces rapidly and no filament is observed. In the case of viscoelastic solutions, the elastic force becomes dominant and a fluid filament appears between the plates, like in figure 3.9(*b*). Then, the thinning rate will depend on the level of elasticity of the fluid. In the case of 76 ppm, the filament remains during 1 s before the breakdown. In the case of 1000 ppm, the filament remains more than 5 s. As can be observed in figure 3.9(*a*) the midplane diameter of the filament decays exponentially in time. In practise, this is used to obtain the relaxation time, λ_e, applying the upper convected Maxwell constitutive model [68, 70, 71, 69], which is described by the following equation,

$$\frac{D(t)}{D_0} = \left(\frac{G_1 D_0}{4\gamma}\right)^{1/3} \exp\left[-t/3\lambda_e\right] \tag{3.3}$$

where G_1 is related to the elastic modulus and γ is the surface tension, which is equal to $58.1\,\mathrm{mN\cdot m^{-1}}$ for all the fluids with concentrations 0, 76, 100, 150, 300 and 1000 ppm of PEO. The surface tension was measured using a tensionmeter (DSA100 from KRÜSS). It works using the principle of the pendant drop. When a drop is suspended, an increase of pressure is produced inside the drop as a results of the surface tension and gravity. The correlation between the pressure difference, Δp, the radii of curvature, r_1 and r_2, of the surface and the surface tension is described by the Young-Laplace equation,

$$\Delta p = \gamma \left(\frac{1}{r_1} + \frac{1}{r_2} \right) \tag{3.4}$$

In practice, liquid is injected from a needle, so that it forms a drop on the tip. The drop is then optically observed and the surface tension is calculated from the shape of the drop, based on equation 3.4. Once γ is calculated, G_1 can be obtained. The value of G_1 for each concentration is given in table 3.2. For concentrations of 76, 100 , 150 and 300 ppm the value of G_1 is similar. However, for a concentration of 1000 ppm G_1 is considerably larger.

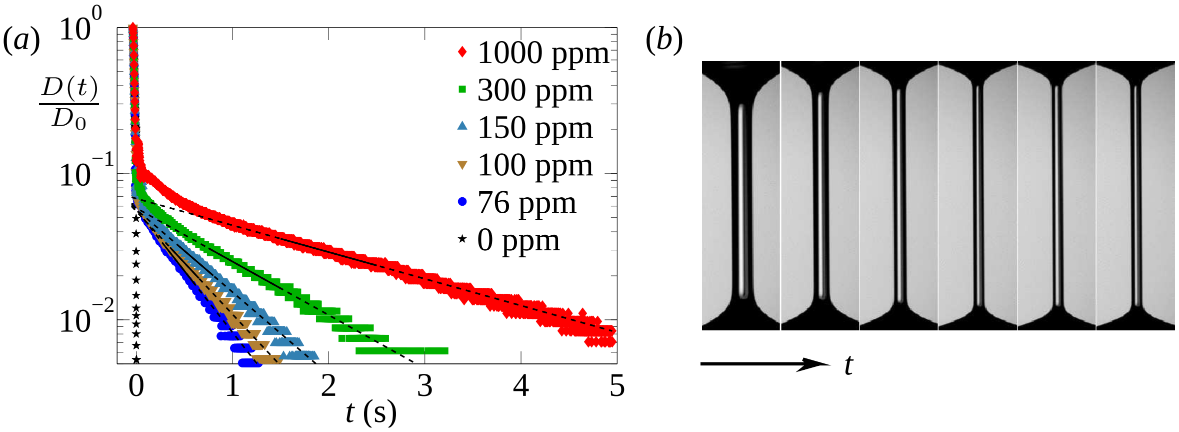

Figure 3.9: Capillary thinning of fluid filaments. (*a*) Evolution of the normalised diameter, $D(t)/D_0$, as a function of time for water solutions containing 7 wt.% of PEG and different concentrations of PEO. (*b*) Snapshots at increasing times, in intervals of 0.5 s, of the fluid filament formed by a solution containing 300 ppm of PEO between the plates of the CaBER after stretching.

	76 ppm	100 ppm	150 ppm	300 ppm	1000 ppm
G_1 (mPa)	7.05	6.62	6.79	7.19	11.68

Table 3.2: Constant G_1 for viscoelastic water solutions containing 7 wt.% of PEG and different concentrations of PEO.

Figure 3.10 depicts the relaxation time, λ_e, as a function of the concentration of PEO, $\mathrm{C_{PEO}}$. The points have been fitted by an exponential law as,

$$\lambda_e = \mathrm{A}_e \mathrm{C}_{\mathrm{PEO}}^{\beta} \tag{3.5}$$

where the constant $\mathrm{A}_e = 12.048\,\mathrm{s}$, and the exponent $\beta = 0.61$, which is close to 0.71 ± 0.03 found by Stelter *et al.* [68] for aqueous solutions of PEO of molar mass 4×10^6 g/mol. In their case, the solutions did not contained neither PEG nor alcohol. The extensional relaxation times, λ_e, are shorter than the relaxation times from shear tests [62, 63] and longer than those from normal force analysis [72]. Also, λ_e is of the same order as the Carreau parameter λ_C.

The flow of polymer solutions is characterised by a stress tensor, $\bar{\bar{\tau}}$, that can be expanded into two parts: the contribution of the solvent to the stress tensor, $\bar{\bar{\tau}}_s$, and the contribution of the polymer to the stress tensor tensor, $\bar{\bar{\tau}}_p$. Hence, $\bar{\bar{\tau}} = \bar{\bar{\tau}}_s + \bar{\bar{\tau}}_p$. It follows that the total viscosity, μ, can be interpreted as the sum of the solvent viscosity, μ_s, and the contribution of the polymer, μ_p, *i.e.*, $\mu = \mu_s + \mu_p$. The elasticity of the fluid only has effects in the polymeric component of the stress, whereas the inertia has effects on both components. To quantify the importance of the polymeric stress to the total shear stress, the viscosity ratio is defined as $S = \mu_p/\mu_s = (\mu - \mu_s)/\mu_s$. To summarize, table 3.3 reports the values of the total shear viscosity, the viscosity ratio and the extensional relaxation time.

$\mathrm{C_{PEO}}$ (ppm)	μ $(\mathrm{mPa \cdot s})$	S	λ_e (ms)
76	8.065	0.094	171
100	8.115	0.1	201
150	8.947	0.213	254
300	10.965	0.487	395
1000	33.500-20.062	1.720-3.542	823

Table 3.3: Properties of the different PEO solutions dissolved in an aqueous solvent containing 7% PEG, whose shear viscosity, μ_s, is $7.375\,\mathrm{mPa \cdot s}$.

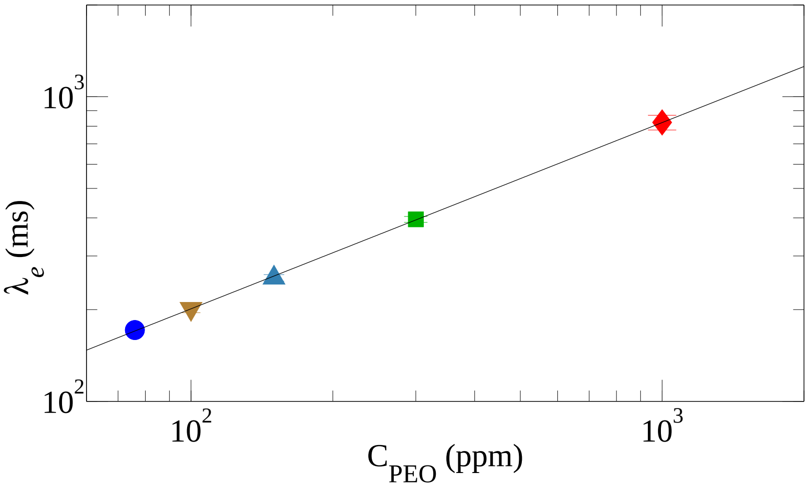

Figure 3.10: Variation of the extensional relaxation time, λ_e, with the concentration of PEO, C_{PEO}. The error bars represent the standard deviation over 3 measurements and are smaller than the symbols. The black straight line is a power law fitting with an exponent of 0.61.

3.3 Reflective particles for visualisation purpose

For flow visualisation purpose, Kalliroscope AQ1000 was added to all the fluids. This is a suspension of $1-2\%$ of reflective flakes which align their largest dimension to the planes of shear. Savaş [73] studied these particles in the case of Couette flow and came to the conclusion that the particles align onto the stream surfaces. More recently, Abcha *et al.* [74] analysed the behaviour of these particles in the Couette-Taylor flow and established that the intensity of light reflected by Kalliroscope flakes is related to the radial velocity component when the outer cylinder is fixed. The particles have a typical size of 30 µm × 6 µm × 0.07 µm [75, 76] with a density of ρ =1.62 g/cm^3. Sedimentation of these particles remains negligible in horizontal or vertical configurations if the experiment lasts less that 10 hours [75]. These particles do not modify significantly the flow viscosity and no non-Newtonian effect is detected as far as small concentrations under 8.1 w.t% are used [76]. Concentrations below 2 wt.% were chosen to get suitable light contrasts in the flow.

Chapter 4

Torque in turbulent Couette-Taylor flows

"C'est par la logique que l'on prouve et par l'intuition que l'on découvre".

—Jules Henri Poincaré

Torque measurements in three systems with three different radius ratios and aspect ratios have been performed for large rotation rates of the inner cylinder. Flow visualisations illustrate a specific procedure to select a given number of turbulent vortices and the influence of the vortex size on the flow. The relationship between the torque and the rotation speed is given by an analytical relationship near the threshold of Taylor vortex flow and by a power law for turbulent flows. The torque for flows containing different number of vortices is reported and a crossing of the different torque-speed curves is found, corresponding to the transition to the ultimate regime of turbulence. Before each intersection, flows with larger number of vortices exert higher levels of torque. After each intersection, flows with larger number of vortices exert lower levels of torque. The level of torque also depends on the radius ratio of the system. The exponent of the scaling laws presents different behaviours depending on the regime of the flow and also depends on the number of vortices. In the ultimate regime it becomes nearly constant when increasing the Reynolds number. The pre-factor becomes independent of the Reynolds number in the ultimate regime. Finally, the effect of the radius ratio and the aspect ratio in the transition to the ultimate regime is analysed.

4.1 Introduction

Turbulent Couette-Taylor flows have been investigated since the works by Wendt [4] and Taylor [32]. They are interesting because the energy dissipation and the momentum transfer can be well quantified through torque measurements [44]. Due to the high non-linearity of this turbulent states, the level of torque depends on different parameters. In this chapter, we focus on the effect of the number of vortices and the radius ratio on the torque.

The number of vortices in a finite-length Couette-Taylor flow is one of the most important flow parameters, since the momentum transfer strongly depends on it. However, the size of those vortices at a given Reynolds number is not a trivial problem and no general rule exists to predict it accurately. Different studies have focused on the number of cells at low Re, like those by Coles [25] or Benjamin and Mullin [31]. Other works that dealt with turbulent flows and the number of vortices were interested in the different level of torque that they induced on the inner cylinder, like those by Lathrop *et al.* [16] and Lewis and Swinney [6]. Recently, experiments performed by Huisman *et al.* [50] at $Re = \mathcal{O}(10^6)$ proved the existence of multiple states in the ultimate regime of turbulence, a regime where the boundary layers become turbulent. Also, recent numerical investigations by Ostilla-Mónico *et al.* [7] focused on flows with different wavelengths and its influence on the torque. These simulations use periodic boundary conditions and the wavelength of the vortices is an imposed parameter, so certain wavelengths might be unstable in given experiment.

The curvature, that depends on the radius ratio, η, is also one of the important geometrical parameters in the Couette-Taylor system, since the centrifugal force, which depends on the curvature, is the main destabilising mechanism of the flow. In fact, at low Re the laminar flow is destabilised by centrifugal forces. The first torque measurements by Wendt [4] and Taylor [32] were already performed in systems with different radius ratios and led to the conclusion that they are affected by the curvature. Recently, Ostilla-Mónico *et al.* [8, 7] carried out numerical simulations and found an influence of the radius ratio on the torque scaling and the transition to the ultimate regime of turbulence.

The chapter is organised as follows. In §4.2 flow visualisations are shown and the effect of the vortex size on the flow is reported in §4.3. In §4.4 the torque measurement for the different systems are presented, focusing on turbulent flows at high Reynolds numbers. The exponents of the scaling law of the torque with the Reynolds number are presented in §4.5, and the behaviours of the exponent and the pre-factor are analysed. The transition to the ultimate regime is discussed in §4.6. The conclusion is drawn in §4.7.

4.2 Flow visualisations

Due to different instabilities that emerge in the flow when the Reynolds number increases, the velocity field of the flow is restructured giving rise to different patterns. These patterns can be observed by using visualisation techniques and information about the flow can be obtained. As it will be presented in figure 4.1, the flow undergoes different transitions, from the laminar Couette flow to the turbulent Taylor vortex flow. Actually, one of the main feature of the Couette-Taylor flow is the vortices and their length. Hence, the goal of this section has been to focus on the number of vortices present in the flow, their length and the way they are affected by the aspect ratio of the systems.

4.2.1 Patterns in Couette-Taylor flow

With the help of a tracer that reflects the light, Kalliroscope, the patterns arising in a Couette-Taylor flow can be observed. In figure 4.1 photographs of different patterns in a system with $\eta = 0.909$ and $\Gamma = 30$ are presented. Note that the height of the cylinder is 150 mm. The fluid is Newtonian and consists of mixtures of water and glycerol at different concentrations. Photographs were taken using an exposure time of 125 μs. Figure 4.1(a) presents a snapshot of a laminar Couette flow at $Re = 20$. Figure 4.1(b) shows a Taylor vortex flow, which is a flow pattern of time-independent, axisymmetric, toroidal vortices, characterised by a single axial wavenumber. Figure 4.1(*c*) corresponds to a wavy vortex flow, a flow pattern of time-dependent, non-axisymetric vortices characterised by a single axial wavenumber and a single azimuthal wavenumber. Figure 4.1(*d*) presents a snapshot of a modulated vortex flow, a flow pattern of non-axisymmetric vortices characterised by a double temporal frequency.

As Re is further increased, the pattern bifurcates to a chaotic state with weak turbulent patches that spread in the flow while the large scale structures remain. The following snapshots correspond to turbulent flows. Figure 4.1(*e*) shows a chaotic wavy vortex flow. Figure 4.1(*f*) corresponds to a wavy turbulent flow, which is a flow characterised by a singular temporal frequency. This pattern is analogous to the wavy vortex flow but turbulent. Figures 4.1(*g*-*i*) present a turbulent vortex flow for increasing Re, an analogous pattern to the Taylor vortex flow but turbulent [41]. Note that as Re is increased the large scales are less visible because of the increase of turbulence.

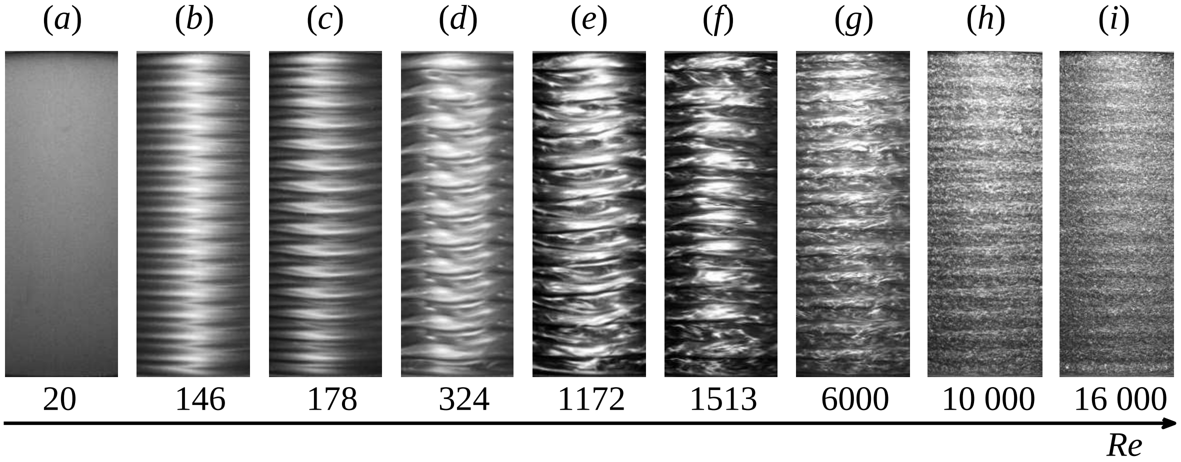

Figure 4.1: Snapshots of Couette-Taylor flows at different Reynolds numbers. (*a*) Laminar Couette flow. (*b*) Taylor vortex flow. (*c*) Wavy vortex flow. (*d*) Modulated wavy vortex flow. (*e*) Chaotic wavy vortex flow. (*f*) Wavy turbulent vortex flow. (*g*), (*h*) and (*i*) Turbulent Taylor vortex flows.

4.2.2 Selection of the number of vortices

The experimental procedure used to select different numbers of vortices in a system with $\eta = 0.909$ and $\Gamma = 30$ is presented. In quasi-static ramping of the velocity, the Taylor vortex flow is characterised by 30 time-independent, axisymmetric toroidal vortices from $Re_c = 138$. This value is close to the predicted value, $Re_c^{th} = 139$ given by the stability theory [77]. For $157 < Re < 199$, wavy vortex flow is seen. From $Re = 199$, modulated wavy vortex flow is observed.

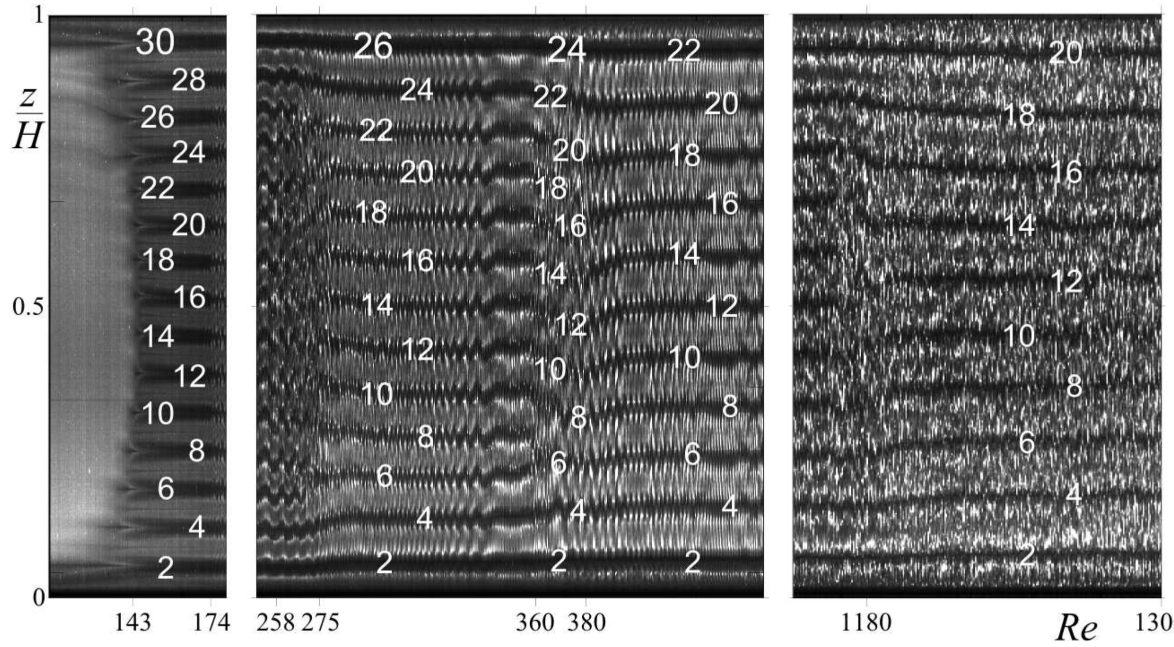

Figure 4.2: Spatio-temporal diagram over the whole height ($\Gamma = L/d = 30$) of the Couette-Taylor flow ($\eta = 0.909$) in three intervals from $Re = 110$ to 1300. The dimensionless acceleration rate is $dRe/d\tau_v = 4$. The numbers on the diagram count the number of cells from bottom to top.

In figure 4.2, a spatio-temporal diagram of the flow patterns over the whole height of the cylinders is presented. The flow is driven by the rotation of the inner cylinder at a constant ramping rate, $dRe/d\tau_v = 4$, where $\tau_v = t\nu/d^2$ and t is time. As Re increases from laminar Couette flow, Eckman vortices develop at the end plates of the cylinders [78]. Then, these vortices evolve into a well-defined state of axisymmetric steady toroidal Taylor vortices that rapidly join at the centre of the cylinder at $Re = 143$. At $Re = 174$, the wavy vortex flow starts. Note that the onset of Taylor vortices and wavy vortices is delayed, as the dimensionless acceleration is faster than the quasi-static one, $dRe/d\tau_v < 0.6$ [79]. In figure 4.2, the second interval ($250 < Re < 450$) shows sequences of regions with strong modulation leading to the merging of cells (26, 24 and 22). In the same range of Re, Coles [25] showed in a system of similar aspect ratio that a large number of expected states were accessible due to the vertical oscillations and the merging of these cells. Clearly, as we progress in time or in *Re* the number of cells decreases from 30 to 20. To obtain a smaller number of cells, say 18, a lower acceleration is used. Hence, this merging of cells will allow to prepare an initial state with 30 to 18 cells. Once the desired number of cells is set up, our strategy is to instantaneously change the torque to a prescribed value and then measure the velocity for few minutes before the next measurement. The stability of each state was tested for approximately 70 times the viscous time, *i.e.* ν/d^2, to ensure that the number of vortices remained constant. The velocity fluctuations of the rotating cylinder are small, typically around 0.6%.

4.2.3 States and number of vortices

The number of vortices depends on multiple parameters and the most important is the aspect ratio, Γ, which establishes the range of number of vortices that a system can hold. In general, the number of vortices in a Taylor vortex flow is close to the aspect ratio, for example, a system with $\Gamma = 30$ will contain 30 circular vortices, as seen in figure 4.2. Any deviation to the value of Γ means that the vortices elongate or shorten in the axial direction. In the turbulent state, the number of vortices at a given *Re* can vary in a wider range than in a flow with laminar structures, because of the increase of degrees of freedom induced by the non-linearity of turbulence.

Snapshots of various flows with different numbers of vortices at distinct *Re* in a system with $\eta = 0.909$ and $\Gamma = 30$ are presented in the following figures. Figures 4.3(*a*-*g*) depict images of flows at $Re = 6000$ containing 18, 20, 22, 24, 26, 28 and 30 vortices, respectively. Figures 4.4(*a*-*d*) depict images of flows at $Re = 10\ 000$ containing 18, 20, 30 and 32 vortices. Figures 4.5(*a*-*d*) display images of flows at $Re = 13\ 000$ and containing 18, 20, 30 and 32 vortices. Figures 4.6(*a*-*d*) display images of flows at $Re = 16\ 000$ containing 18, 20, 30 and 32 vortices.

Figure 4.7 presents different snapshots of flows containing eight, six and four vortices in a system with $\eta = 0.6$ and $\Gamma = 6.8$. Figures 4.7(*a*) and (*b*) depict flows with six and

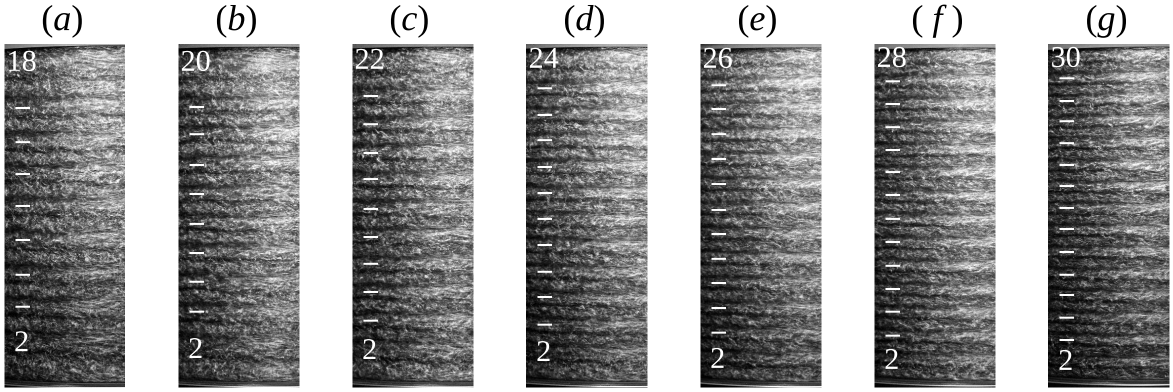

Figure 4.3: Snapshots of turbulent Taylor vortices in a system with $\eta = 0.909$ and $\Gamma = 30$ at $Re = 6000$. (*a*) 18 cells, (*b*) 20 cells, (*c*) 22 cells, (*d*) 24 cells, (*e*) 26 cells, (*f*) 28 cells and (*g*) 30 cells.

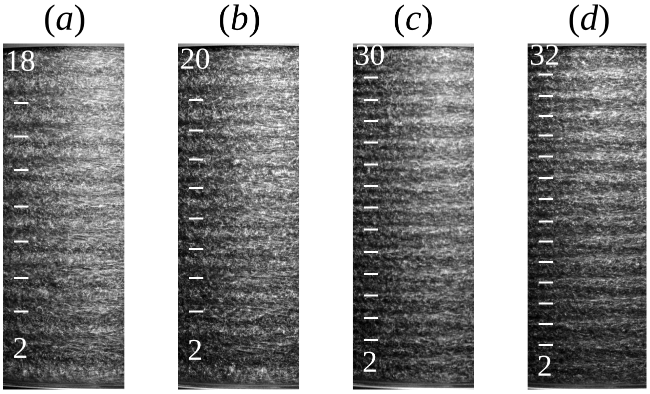

Figure 4.4: Snapshots of turbulent Taylor vortices in a system with $\eta = 0.909$ and $\Gamma = 30$ at $Re = 10\ 000$. (*a*) 18 cells, (*b*) 20 cells, (*c*) 30 cells and (*d*) 32 cells.

eight Taylor vortices at $Re = 110$ and 146, respectively. The end effects elongate the vortices close to the top and bottom. This behaviour was previously observed [78] in a system with large gap, $\eta = 0.75$, and small aspect ratio, $\Gamma = 6$. Figures 4.7(*c*) and (*d*) depict flows at $Re = 6000$ with six and eight vortices, respectively. Figure 4.7(*e*) shows a flow at $Re = 12\ 000$ with four vortices. Interestingly, this state with four vortices has only been found at this particular Reynolds number. Finally, figure 4.7(*f*) shows a flow at $Re = 45\ 000$ containing six vortices. The counting of turbulent vortices becomes a difficult task when the gap increases, this is the reason why the snapshots are blurred,

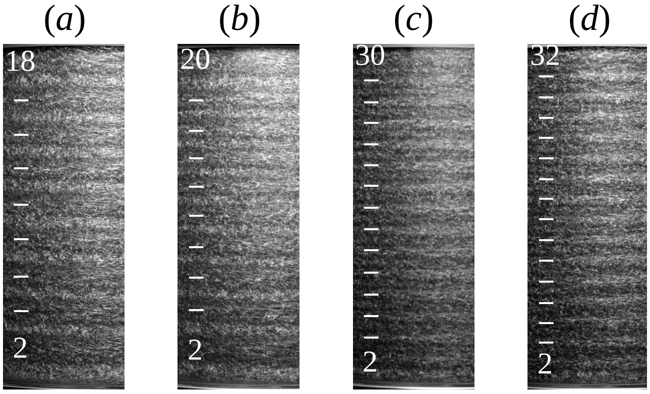

Figure 4.5: Snapshots of turbulent Taylor vortices in a system with $\eta = 0.909$ and $\Gamma = 30$ at $Re = 13\ 000$. (*a*) 18 cells, (*b*) 20 cells, (*c*) 30 cells and (*d*) 32 cells.

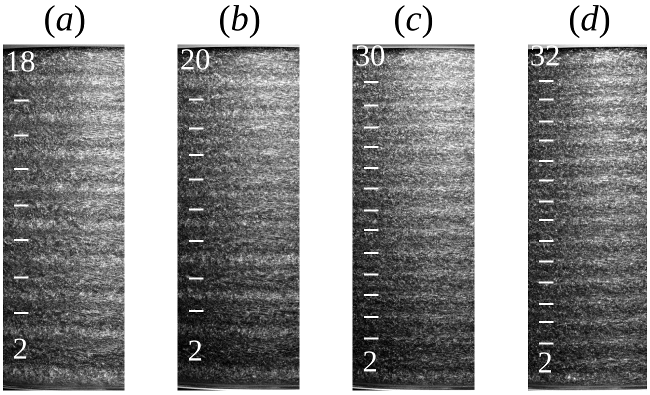

Figure 4.6: Snapshots of turbulent Taylor vortices in a system with $\eta = 0.909$ and $\Gamma = 30$ at $Re = 16\ 000$. (*a*) 18 cells, (*b*) 20 cells, (*c*) 30 cells and (*d*) 32 cells.

as can be observed from figures 4.7(*c-f*). Nevertheless, in the present case, the vortices could be counted while the experiments were running because they were still clear.

Figure 4.8 depicts different snapshots of flows containing several number of vortices at different Reynolds numbers in a system with $\eta = 0.973$ and $\Gamma = 100$. Figure 4.8(a) shows a flow with 100 Taylor vortices at $Re = 272$. Figure 4.8(b) shows a flow with 98 wavy vortices at $Re = 302$. Figure 4.8(c) shows a flow with 84 modulated wavy vortices at $Re = 373$. The modulation reduces significantly the number of vortices, hence they become more elongated in the axial direction. Figure 4.8(d) shows a flow with 68 turbulent vortices at $Re = 2030$. Finally, figure 4.8(e) shows a flow at $Re = 5041$.

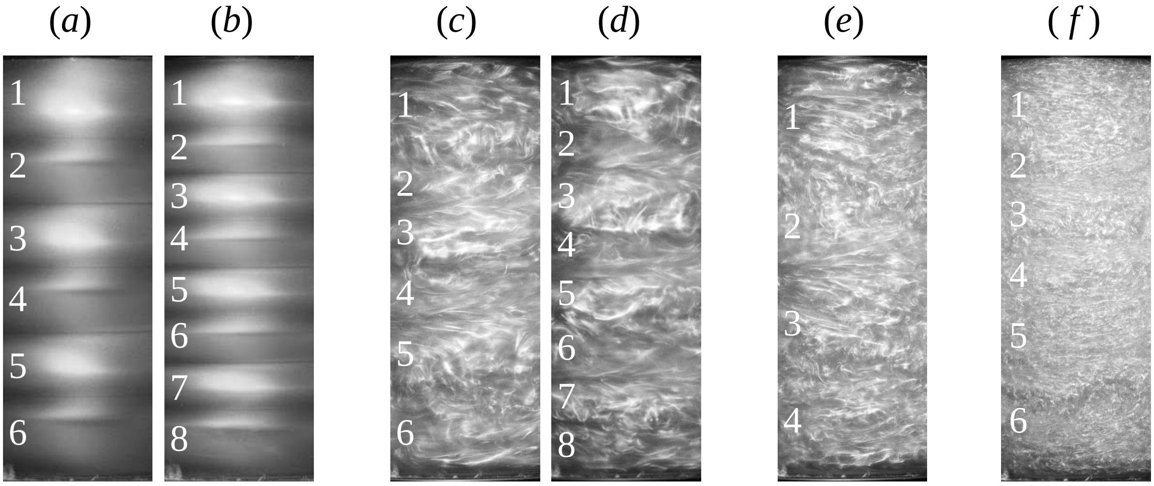

Figure 4.7: Snapshots of flows in a system with, $\eta = 0.6$ and $\Gamma = 6.8$. The numbers help to count the vortices. (*a*) and (*b*) flows containing six and eight Taylor vortices at $Re = 110$ and 146, respectively. (*c*) and (*d*) flows containing six and eight turbulent Taylor vortices, respectively, at $Re = 6000$. (*e*) Flow containing four turbulent Taylor vortices at $Re = 12\ 000$. (*f*) Flow containing six turbulent Taylor vortices at $Re = 45\ 000$.

Here, the number of vortices can not be determined.

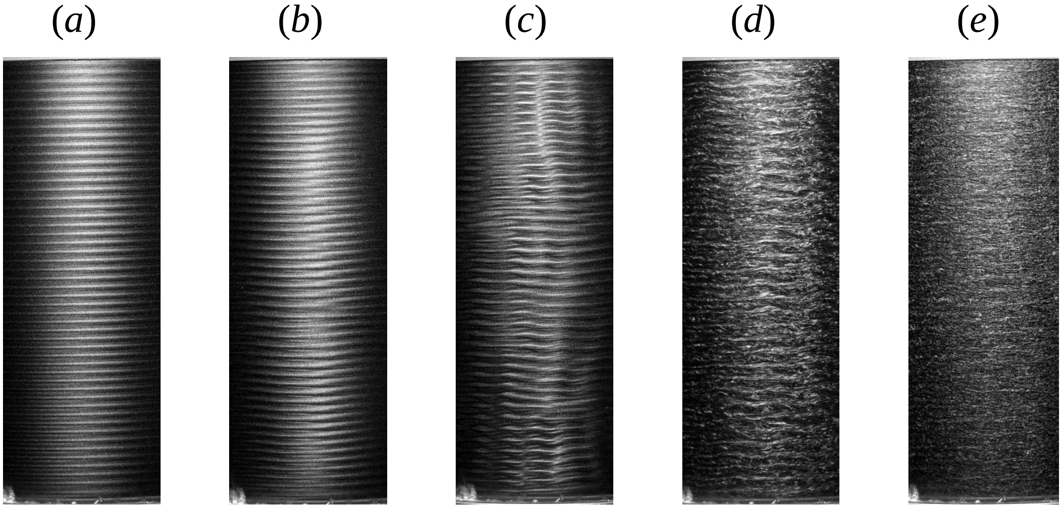

Figure 4.8: Snapshots of flows in a system with $\eta = 0.973$ and $\Gamma = 100$. (*a*) Flow containing 100 Taylor vortices at $Re = 272$. (*b*) Flow containing 98 wavy vortices at $Re = 302$. (*c*) Flow containing 84 modulated wavy vortices at $Re = 373$. (*d*) Flow containing 68 turbulent Taylor vortices at $Re = 2030$. (*e*) Flow at $Re = 5041$.

Figure 4.9 presents different snapshots of flows containing 20 and 18 vortices in a system with $\eta = 0.5$ and $\Gamma = 20$. Figure 4.9(a) shows a flow with 20 turbulent Taylor vortices at $Re = 6000$. Figure 4.9(b) shows a flow with 18 turbulent Taylor vortices at $Re = 6000$.

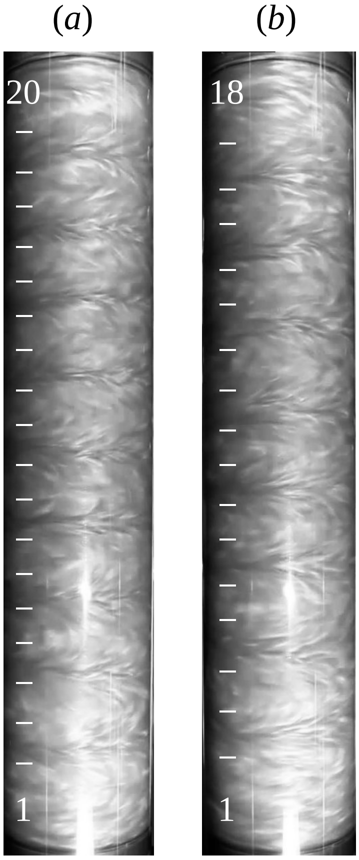

Figure 4.9: Snapshots of turbulent vortices in a system with $\eta = 0.5$ and $\Gamma = 20$ at $Re = 6\ 000$. (a) Flow containing 20 turbulent Taylor vortices. (b) Flow containing 18 turbulent Taylor vortices.

4.3 Aspect ratio and end effect

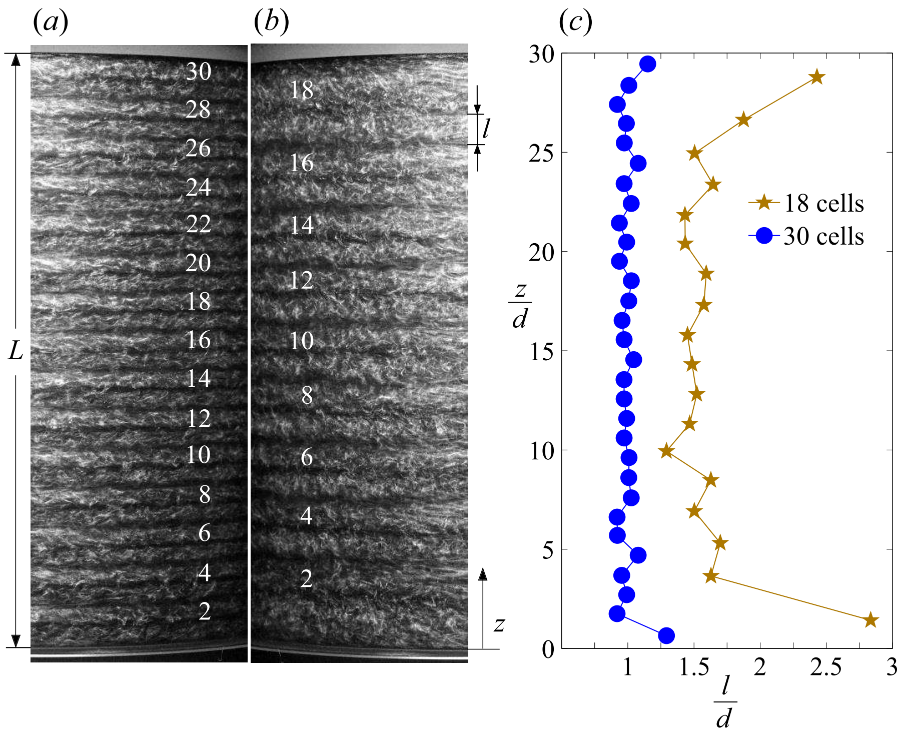

Figure 4.10: Snapshots and aspect ratio along the axis of 30 and 18 cellular modes at $Re = 6000$. (*a*) Normal 30 cells, (*b*) abnormal 18 cells and (*c*) the associated aspect ratio along the axis.

The finding of different states for the same boundary conditions requires that the size of the cells varies from one state to another. In figure 4.10(*a*,*b*), photographs of two states with 30 and 18 cells at $Re = 6000$ in a system with $\eta = 0.909$ and $\Gamma = 30$ are depicted. Figure 4.10(*c*) presents their aspect ratio along the vertical axis. For intermediate numbers of cells, 20, 22, 24, 26 and 28, intermediate curves are found, but not shown for clarity of the figure. For the primary state of 30 cells, the aspect ratio, l/d, of all the cells is close to one. However, for the 18-cell pattern, the ratio l/d is 1.5 in the centre of the cylinder, so the cells are elongated. It should be noted that the cells close to the ends of the cylinders have a significantly larger aspect ratio up to 2.75. This indicates that the caps have a local effect and strongly elongate the two cells close to the ends [78]. Even if the data on the aspect ratio are for $Re = 6000$, one can check in figures 4.3, 4.4, 4.5 and 4.6 that the flows look essentially similar to the ones in figure 4.10(a,b) when increasing Re, although fuzzier.

To quantify the effect of the ends plates on the vertical elongation of the vortices, the height of the cells has been measured in three systems containing several number of vortices at $Re = 6000$. Figure 4.11 shows the mean aspect ratio of the vortices far away from the end plates, $\bar{l}/d$, as a function of Γ/n_v, where n_v is the number of vortices. Hence, the vortices close to the end plates have been neglected. The red continuous line, (−), is the bisecting that separates the bottom part, where the vortices in the middle are compressed in the axial direction, and the upper part, where the vortices are elongated. Hence, the points laying on such bisecting line means that all the vortices along the axis have the same height. It is found that the smaller is the number of vortices in the flow, the parameter Γ/n_v increases, the more compressed the vortices are, hence the points on the right move down with respect to the bisecting line. This indicates that the vortices close to the end plates become more elongated when reducing the number of vortices, compressing the other vortices. This behaviour is well observed in figure 4.10(c) for $\Gamma = 30$ between the flows with 30 and 18 cells, where the top and bottom vortices of the 18-cell state are bigger than for the 30-cell state. Particularly, the average size of the top and bottom vortices for the 30, 28, 26, 24, 22, 20 and 18 vortices states are 23, 25, 42, 59, 72, 94 and 81% bigger than the mean height of the vortices far away from the end, respectively. This occurs because when the number of vortices is reduced, those close to the end plates have more freedom to expand in the gap and compress the vortices in the middle. Clearly, the effect of the end plates on the vortices height increases when decreasing the number of vortices.

Another result that is obtained from figure 4.11 is the effect of the aspect ratio, Γ, on the mean aspect ratio of the vortices, $\bar{l}/d$. The larger is Γ the less compressed are the vortices in the middle, so they tend to have the same size wherever they are located along the axis. Actually, the points for $\Gamma = 30$ are closer to the bisecting line than those for $\Gamma = 20$ and 6.8.

The states in figures 4.10 and 4.11 were obtained at $Re = 6000$. The largest vortex

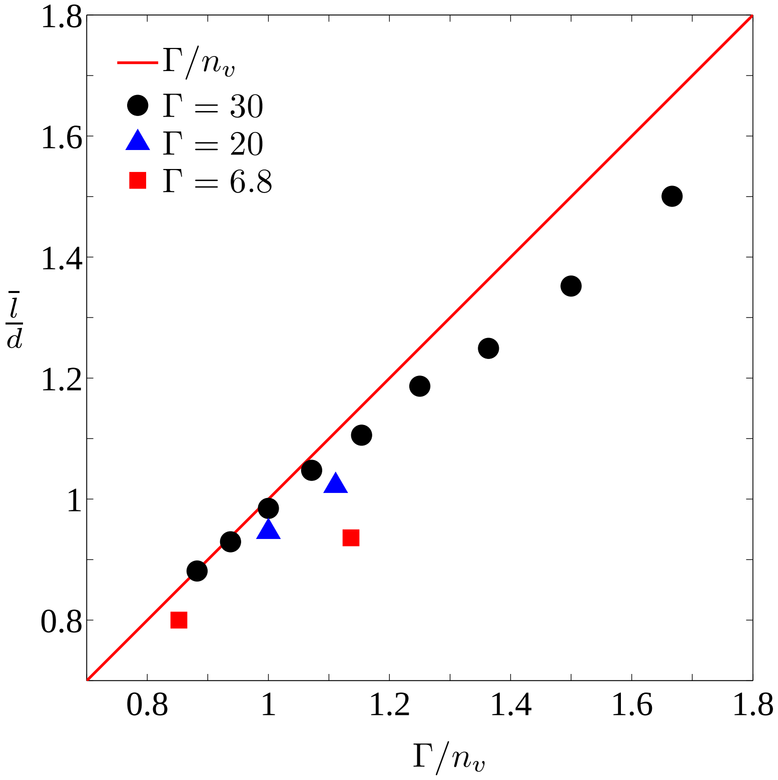

Figure 4.11: Mean value of the aspect ratio of the vortices far away from the end plates, $\bar{l}/d$, as a function of Γ divided by the number of vortices, n_v, in three systems with different aspect ratios: $\Gamma = 30$, 20 and 6.8. The radius ratios are $\eta = 0.909$, 0.5 and 0.6, respectively. The red line (—) is the bisecting where all the vortices have the same size along the axis.

aspect ratio for $\Gamma = 30$ and $\eta = 0.909$ is 1.5 for 18 cells and the smallest is 0.88 for 34 cells. In the numerical simulations by Ostilla-Mónico *et al.* [7] the smallest vortex aspect ratio found for $\eta = 0.909$ is 0.75 and the authors argue that this might be an artificial result due to numerical constraint and not stable in an experiment. Effectively, no states with vortex aspect ratio smaller that 0.88 have been found for $\eta = 0.909$. However, in the case of $\eta = 0.6$, the smallest $\bar{l}/d$ found is 0.8.

4.4 Global variation of the torque

When the rotation speed of the inner cylinder increases from rest, the different instabilities that appear make the flow undergoes several transitions, giving rise to different states. The patterns that characterise these states were already presented in figure 4.1. In figure 4.12 it is shown the evolution of the rescaled torque Nu_ω as function of the Reynolds number, Re, in the system with $\eta = 0.909$. In the following subsections the different $Nu_\omega(Re)$ curves for each system is analysed.

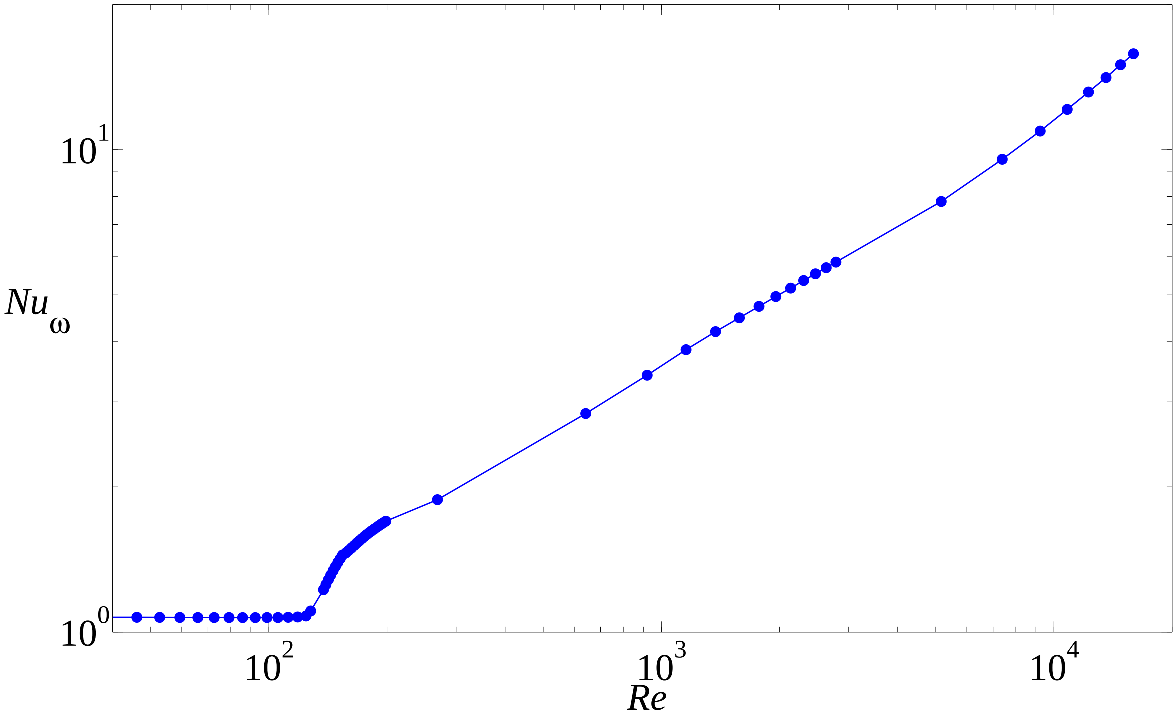

Figure 4.12: Variation of Nu_ω with Re in a system with $\eta = 0.909$.

4.4.1 Variation of torque in pre-turbulent flows

The evolution of the torque with the rotation speed of the inner cylinder is analysed for laminar Couette flow (see figure 4.1(*a*)), Taylor vortex flow (see figure 4.1(*b*)) and wavy vortex flow (see figure 4.1(*c*)) in systems with $\eta = 0.973$, 0.909 and 0.6. Figure 4.13 depicts the evolution of Nu_ω with Re up to $Re = 1000$ in logarithmic scale. The ω-Nusselt number associated to the azimuthal Couette flow (-) is constant and above one in all the cases, because of the end plates that introduce an additional torque with respect to an infinite cylinder. In the case of $\eta = 0.6$, $Nu_\omega = 1.66$ presenting the largest shift. This is due to the small aspect ratio, $\Gamma = 6.8$, that makes the end effect considerably significant. In the other two cases $Nu_\omega = 1.16$ and 1.07 for $\eta = 0.973$ and 0.909, respectively. One might think that the Nu_ω for $\eta = 0.973$ should be smaller than for $\eta = 0.909$, since the aspect ratio of the former, $\Gamma = 100$, is larger that the later, $\Gamma = 30$. This inconsistency could be related to the air bubble below the inner cylinder. In the case of the wider cylinder the surface of the end plates is smaller, but the air bubble is larger and the stress that its edge introduces could be enough to increase the torque.

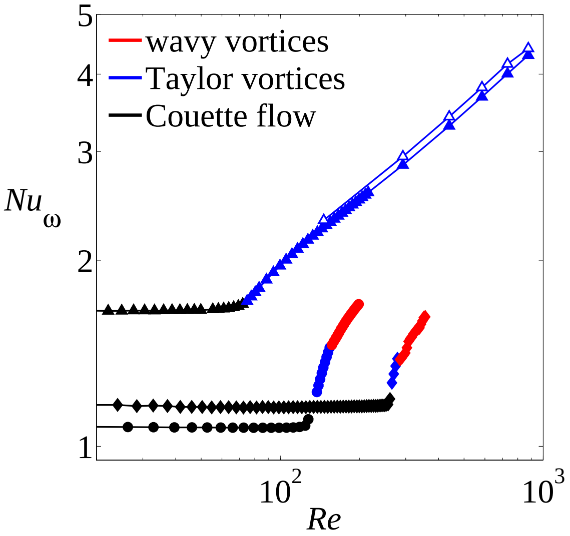

Figure 4.13: Variation of Nu_ω with Re in systems with $\eta = 0.973$, 0.909 and 0.6 in logarithmic scale. Different symbols are used to distinguish different radius ratios: (◆) for $\eta = 0.973$, (●) for $\eta = 0.909$ and (▲) for $\eta = 0.6$. Note that the empty blue triangle, (△), represents a flow with 8 Taylor vortices.

For increasing values of the Reynolds number Nu_ω stops being constant and grows when the Taylor vortices appears in the flow, being completely developed at $Re_c = 73$, 138 and 264, for $\eta = 0.6$, 0.909 and 0.973, respectively. Esser and Grossmann [77] predicted theoretically the onset of Taylor vortices for an infinitely long cylinder at $Re_c^{th} = 73$, 139 and 252, respectively, hence the values agree well. The Nu_ω related to the Taylor vortices is characterised by a sharp increase of the slope. This slope depends on the radius ratio and decreases for decreasing η. This is related to the space between cylinders, the closer they are the better is the momentum transfer. For the case of $\eta = 0.6$ the range of Reynolds number in which Taylor vortices are stable is much larger than the other two systems and goes up to $Re = 880$. This increase of the stability of the Taylor vortices when reducing the aspect ratio was reported before [80]. Moreover, we have been able to set two different states with 6 and 8 vortices, corresponding to the blue filled triangles, (▲), and blue empty triangles, (△), respectively, finding that the flow with larger number of vortices exert larger torque. This is explain by the high momentum transfer efficiency of the vortices, so the more vortices there are in the flow, the better is the momentum transfer. Particularly, the largest difference in torque between the 6-cell state and the 8-cell state is found to be 3.72 % at $Re = 731$. Finally, the vortices are wavy between $138 < Re < 154$ for $\eta = 0.909$. In the case of $\eta = 0.973$ the vortices are wavy from $Re > 264$. No wavy vortices have been identified for $\eta = 0.6$.

In order to compare the torque with analytical results, the date have been rescaled using the laminar torque measured in the experiments, T_{lam}^{exp}. Figure 4.14 shows the rescaled torque, T/T_{lam}^{exp} as a function of Re. Donnelly and Simon [18] proposed the relationship of the momentum transport in the form $Nu_\omega = a_1 Re^{-2} + a_2 Re^{0.36}$. Our data are fitted for the system with $\eta = 0.909$ with values of $a_1 = -13\,374$ and $a_2 = 0.33$.

Another analytical relationship between T/T_{lam} and Re was proposed by DiPrima *et al.* [11] to calculate the torque for Taylor vortices and reads,

$$\begin{aligned}\frac{T}{T_{lam}} = 1 + \mathrm{A}(\eta,q)\left[1 - \frac{Re_c(\eta,q)}{Re}\right] + \mathrm{B}(\eta,q)\left[1 - \frac{Re_c(\eta,q)}{Re}\right]^2 \\ + \mathcal{O}\left[1 - \frac{Re_c(\eta,q)}{Re}\right]^3\end{aligned} \tag{4.1}$$

where $\mathrm{A}(\eta,q)$, $\mathrm{B}(\eta,q)$ and the critical Reynolds number, $Re_c(\eta,q)$, are constants that depend on η and the axial wavenumber, q. Here, $A(\eta,q)$ and $B(\eta,q)$ have been obtained

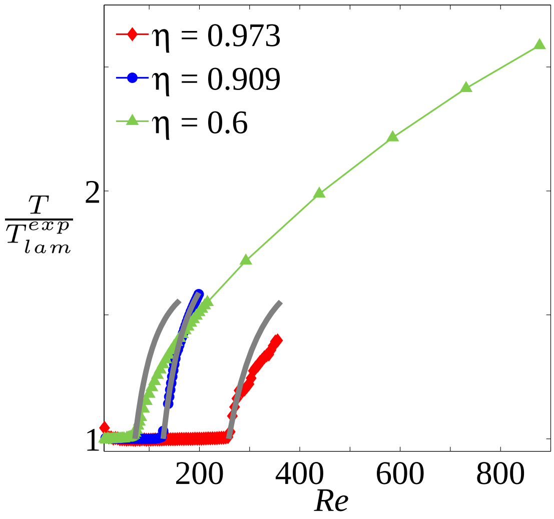

Figure 4.14: Variation of the torque, T, divided by the experimental laminar torque, T_{lam}^{exp}, as a function of Re in linear scale. The grey continuous line corresponds to the analytical expression proposed by DiPrima *et al.* [10].

from DiPrima *et al.* [11] for an axial wavenumber, $q = 3.127$, which correspond to square cells. The values of $Re_c(\eta, a)$ have also been obtained obtained from DiPrima *et al.* [11]. Both tables are reproduced in figure 4.15. The relationship is depicted in figure 4.14 as grey continuous lines and covers the range of Re where the Taylor vortices are stable in our system. In the case of $\eta = 0.909$ the line is extended up to wavy vortex flow. It is also extended in the case of $\eta = 0.973$, although the region of stability of wavy vortices is not known. The lines have been shifted in the Re-axis so the curves begin at the transition points found experimentally, not at the Re_c calculated analytically. The cases for $\eta = 0.973$ and 0.909 agree well with the experimental data in the Taylor vortex regime, but not in the case of $\eta = 0.6$. This is because of the small aspect ratio which makes that the end effects have a strong influence on the torque. Mullin and Benjamin [30] also found that the aspect ratio has an effect on the stability of various steady cellular flows, in particular, a small length of the cylinders increases considerably the end effects. In the case of $\eta = 0.909$ the fitting also agrees for the torque exerted by the wavy vortices.

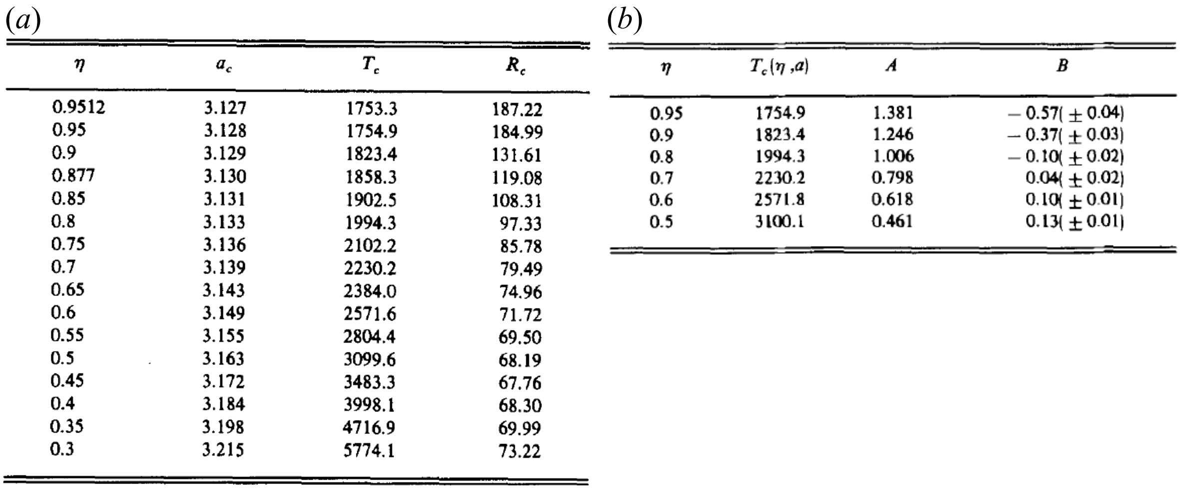

(*a*)

η	a_c	T_c	R_c
0.9512	3.127	1753.3	187.22
0.95	3.128	1754.9	184.99
0.9	3.129	1823.4	131.61
0.877	3.130	1858.3	119.08
0.85	3.131	1902.5	108.31
0.8	3.133	1994.3	97.33
0.75	3.136	2102.2	85.78
0.7	3.139	2230.2	79.49
0.65	3.143	2384.0	74.96
0.6	3.149	2571.6	71.72
0.55	3.155	2804.4	69.50
0.5	3.163	3099.6	68.19
0.45	3.172	3483.3	67.76
0.4	3.184	3998.1	68.30
0.35	3.198	4716.9	69.99
0.3	3.215	5774.1	73.22

(*b*)

η	$T_c(\eta, a)$	A	B
0.95	1754.9	1.381	$-0.57(\pm 0.04)$
0.9	1823.4	1.246	$-0.37(\pm 0.03)$
0.8	1994.3	1.006	$-0.10(\pm 0.02)$
0.7	2230.2	0.798	$0.04(\pm 0.02)$
0.6	2571.8	0.618	$0.10(\pm 0.01)$
0.5	3100.1	0.461	$0.13(\pm 0.01)$

Figure 4.15: Tables from DiPrima *et al.* [11]. (*a*) Table I to obtain the critical Reynolds number, Re_c. (*b*) Table VI to obtain the values of $A(\eta, q)$ and $B(\eta, q)$ for $q = 3.127$.

4.4.2 Variation of torque in turbulent flows

The energy dissipation in a turbulent flow is much larger than in a laminar flow because of the increase of shear stress induced by the chaotic vibration of the fluid particles. This increase of energy dissipation requires to inject more power in the fluid through the torque exerted by the inner cylinder. In addition, the turbulence increases the number of degrees of freedom and multiple states can appear in the flow, corresponding to different numbers of vortices. The torque of turbulent flows in three systems with different radius ratios will be analysed here.

First, torque and speed measurements have been performed in the system with $\eta = 0.909$ and $\Gamma = 30$ up to $Re = 24000$. Using the procedure presented earlier we were able to measure the torque associated to nine different states with distinct number of cells. The relationship between the ω-Nusselt number and the Reynolds number for these states is presented in figure 4.16. Different symbols and colours represent the different states: the laminar Couette flow, the Taylor vortex flow (30 cells), the wavy vortex flow and the nine different turbulent Taylor vortex flows with 34, 32, 30, 28, 26, 24, 22, 20 and 18 cells. In order to access large values of Re up to 24 000, low-viscosity silicone oil was used and two series of data are reported in figure 4.16. The use of silicone oil does not allow to visualise the flow and therefore to count the number of vortices. These data were obtained by applying protocols leading to states with large and small numbers of cells. The trend of the curves suggests that the black triangles correspond to large numbers of cells and empty triangles to small numbers of cells. Clearly, the level of torque depends on the number of vortices. Each state is not stable for every Reynolds number and the onset of turbulence is around $Re \approx 1000$, as can be seen in figure 4.1(e). At Re below $Re = \mathcal{O}(10^4)$ the states with larger number of vortices exert larger torque. A change in the slope is observed above $Re \approx 10^4$, corresponding to the transition to the ultimate regime, as previously observed by Lathrop *et al.* [16], Lewis and Swinney [6], Dubrulle *et al.* [46], Ravelet *et al.* [14], Merbold *et al.* [13] and Ostilla-Mónico *et al.* [8, 7]. In the following, these aspects will be deeply analysed. Additionally, it is presented in figure 4.17 the variation of the dimensionless "wind" dissipation rate per mass, $\hat{\varepsilon}_{wind}$, with the Reynolds number.

The stability domains of the different numbers of vortices are shown in figure 4.18. It is interesting to notice that the 34-, 32-, 30-, 28- and 26-vortex states are not stable for Re below 3800. Similarly, the 24-, 22- and the 20-cell states are not stable for Re below 2300, 2100 and 1700, respectively. In the range between 1000 and 1700, only the 18-cell state is stable. These results are reminiscent of the stability studies of Coles [25], Snyder [26], Koschmieder [29] and Cliffe *et al.* [81].

As the Reynolds number increases, a systematic growth of the ω-Nusselt number is observed. The 18-cell state always has the lowest ω-Nusselt number, whereas the states associated with the largest number of cells always have the highest ω-Nusselt number. As the Reynolds number increases further, the curves of Nu_ω versus Re move closer together. Then, the curves for different states intersect in a range of Re between 9600 and 15 500. A zoom in this range is shown in figure 4.19 where most of the intersections are located at approximately 12 600. In table 4.1 it is presented the value of Re for each intersection. Below each intersection, the torque is larger for states where the number of cells is larger. Above each intersection, the trend changes and a smaller number of cells leads to a larger torque. Similar intersections were reported by Lathrop *et al.*

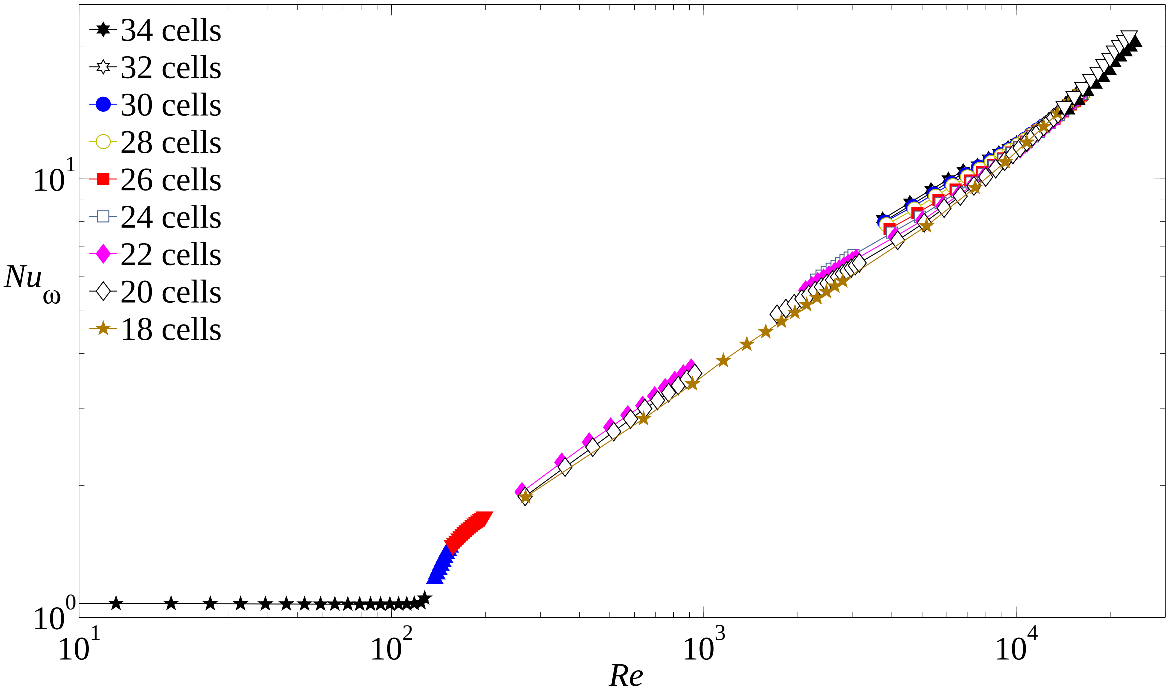

Figure 4.16: Rescaled torque, Nu_ω, as a function of Re for the different flow states in a system with $\eta = 0.909$ and $\Gamma = 30$. The black stars (★), the blue triangles (▲) and the red triangles (▼) represent the laminar Couette flow, the Taylor vortex flow and the wavy vortex flow, respectively. The black triangles (▲) and the empty triangles (▽) represent data obtained using a low viscosity silicone oil.

[16] and Lewis and Swinney [6] for eight- and 10-cell states in a system with η =0.724. Recently, numerical studies by Ostilla-Mónico *et al.* [7] with $\eta = 0.909$ have shown the same behaviour for flows with four distinct wavelengths, where the crossing of the curves are around $Re = 13\,000$. These intersections are a consequence of the transition to the ultimate regime.

Physically, this is explained as a change in the mechanism of momentum transfer. Before the transition to the ultimate regime, the turbulence is driven mainly by the centrifugal force, that induces the vortices, while the boundary layers remain laminar. Hence, the main part of the momentum transfer is carried out by these vortices. This explains why the larger is the number of vortices, the larger is the momentum transfer and the larger the level the torque. However, in the ultimate regime, the boundary layers

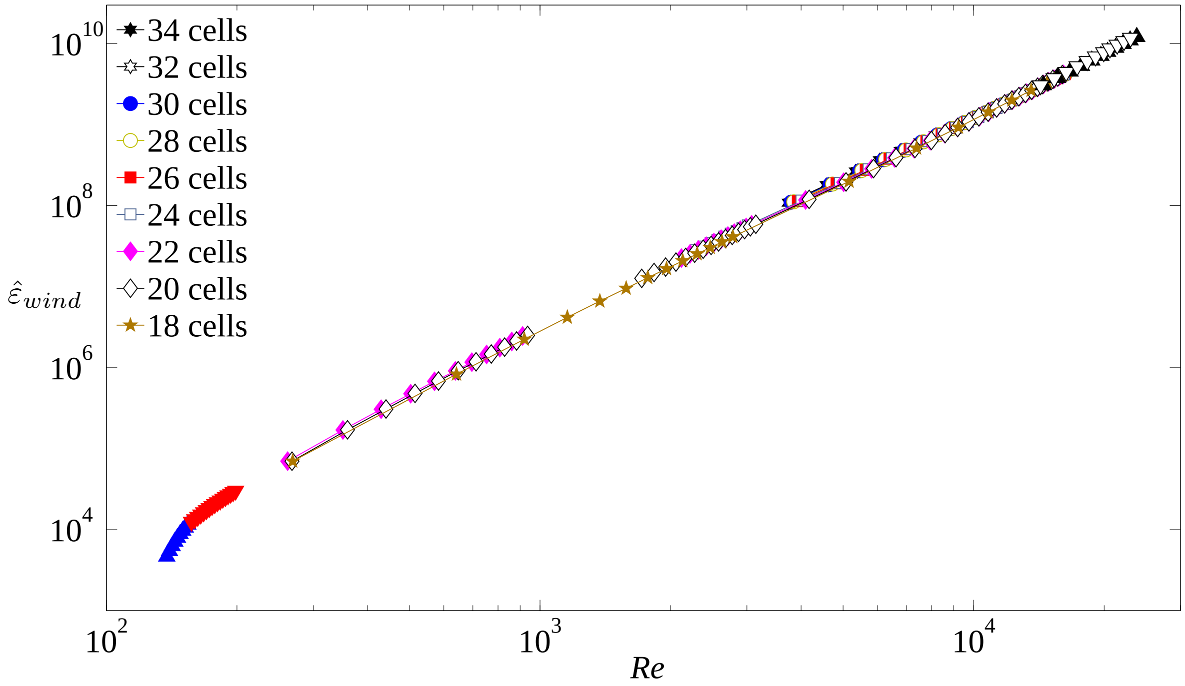

Figure 4.17: Dimensionless "wind" dissipation rate per mass, $\hat{\varepsilon}_{wind}$, as a function of Re for the different flow states in a system with $\eta = 0.909$ and $\Gamma = 30$. The blue triangles (▲) and the red triangles (▼) represent the Taylor vortex flow and the wavy vortex flow, respectively. The black triangles (▲) and the empty triangles (▽) represent data obtained using a low viscosity silicone oil.

become turbulent and dominate the dynamics of the flow [16]. Hence, the turbulence acquires the main role in the momentum transfer. So, the less number of large structure are present in the flow, that is, the vortices, the better is the momentum transport and the larger is the level of torque.

The analysis of our data allows us to present in figure 4.20 the rescaled torque, Nu_ω, as a function of the aspect ratio of the vortices, $\bar{l}/d$, for several values of Re. For relatively small Re, the rescaled torque decreases as the aspect ratio of the vortices increases. For large Re, the rescaled torque increases with $\bar{l}/d$. At $Re = 13\,000$, Nu_ω is almost constant. In the experiments, values of $\bar{l}/d$ between 0.88 to 1.5 correspond to states with 34 to 18 cells. Our results are compared with the numerical simulations of Brauckmann and Eckhardt [12] for a flow containing 2 vortices at $Re = 5000$, and confirm a clear effect of the vortex aspect ratio on Nu_ω. At $Re = 5000$, our values

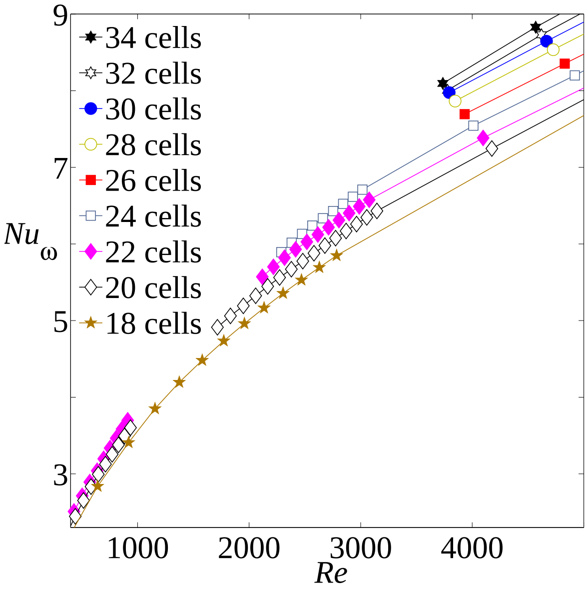

Figure 4.18: Rescaled torque, Nu_ω, as a function of Re for the different flow states in a system with $\eta = 0.909$ and $\Gamma = 30$ to show the stability threshold of different states.

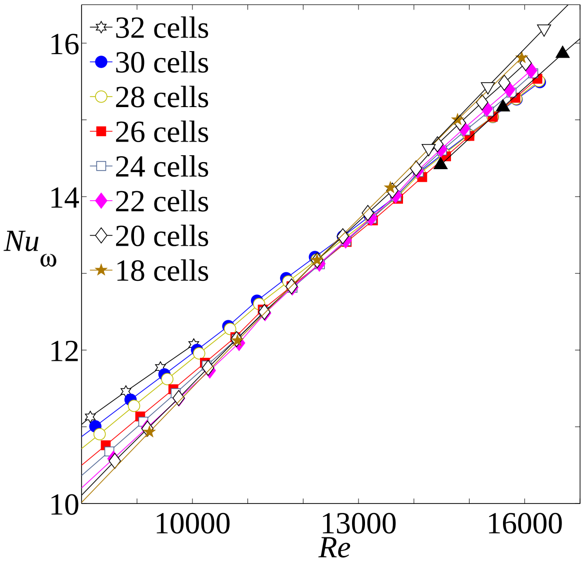

Figure 4.19: Rescaled torque, Nu_ω, as a function of Re for the different flow states in a system with $\eta = 0.909$ and $\Gamma = 30$ to show the intersections between the different curves.

present larger values of Nu_ω for $\bar{l}/d < 1.35$, however, they do not exhibit the peak that these authors found in their data at $\bar{l}/d = 0.965$. The discrepancy between the experiments and the numerical simulations may be due to the fact that the numerical

n_v ($\bar{l}/d$)	30 (0.99)	28 (1.05)	26 (1.13)	24 (1.19)	22 (1.25)	20 (1.34)	18 (1.50)
30 (0.99)		15 296	15 391	13 835	13 532	12 691	12 590
28 (1.05)			15 446	13 480	13 253	12 345	12 311
26 (1.13)				12 407	12 186	11 806	11 773
24 (1.19)					11 711	11 392	11 514
22 (1.25)						9 585	10 170
20 (1.34)							11 689

Table 4.1: Reynolds numbers of the crossings point for different of number of vortices (mean aspect ratio of the vortices). The average of all the Re numbers corresponding to the different intersections equals to 12 591.

simulations were performed for a radius ratio $\eta = 0.71$ and with periodic boundary conditions.

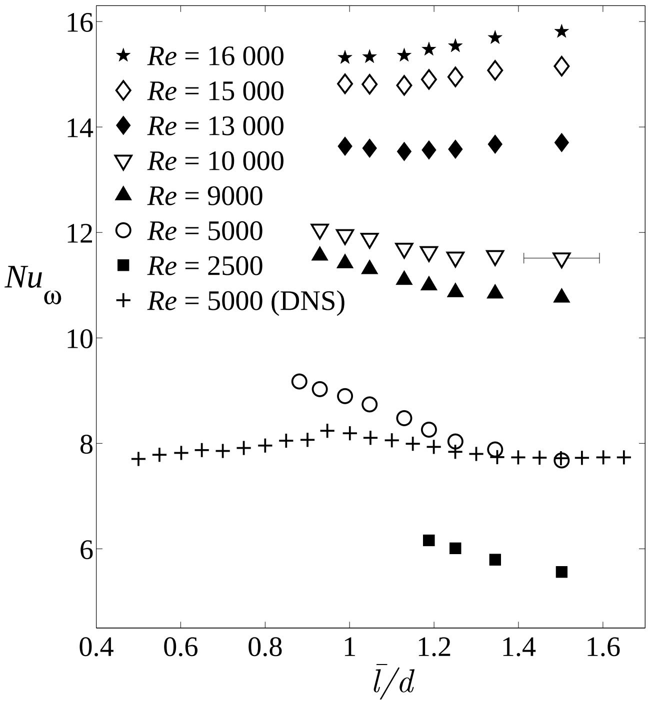

Figure 4.20: Rescaled torque, Nu_ω, as a function of the mean aspect ratio of the cells, $\bar{l}/d$, for different Re in a system with $\eta = 0.909$ and $\Gamma = 30$. The horizontal error bar for $Re = 10\ 000$ represents the maximum error on $\bar{l}$. The vertical error on Nu_ω is smaller than the symbol height. The cross points (+) correspond to the direct numerical simulations (DNS) of Brauckmann and Eckhardt [12] at $Re = 5000$ with $\eta = 0.71$.

Now, the system with $\eta = 0.6$ and $\Gamma = 6.8$ is analysed. Torque speed measurements have been performed up to $Re = 45\ 000$ for flows containing different numbers of vortices. The relationships between the ω-Nusselt number and the Reynolds number are depicted in figure 4.21. Different symbols and colours are used to represent the different states: laminar Couette flow, Taylor vortex flow with six and eight vortices (see figures 4.7(*a*) and (*b*)) and turbulent vortices with eight, six and four cells (see figures 4.7(*c*), (*d*) and (*e*), respectively). Again, different numbers of vortices present distinct levels of Nu_ω. A crossing of the $Nu_\omega(Re)$ curves happens at $Re = 6090$. A zoom around this point is shown in figure 4.22. Before this crossing the state with 8 cells presents larger values of torque. The largest difference of ω-Nusselt between the 8- and the 6-vortex state is 2.18% at $Re = 2779$, when the flow is already turbulent. The differences in ω-Nusselt between the 8- and the 6-vortex for a Taylor vortex flow is 3.72% at $Re = 731$. The difference is larger in the case of laminar vortices, because the momentum transfer is done almost completely by the vortices. However, when the flow is turbulent, part of the momentum transfer is done by the turbulence. Therefore, the differences in torque when varying the number of vortices are smaller. Then, after the crossing of the curves, the state with 8 cells present a lower value of Nu_ω. This behaviour is in agreement with the flow in the system of $\eta = 0.909$. Additionally, the state with 8 vortices is not stable for $Re > 6500$. This behaviour was previously reported in the work of Lewis and Swinney [6], where only one branch of the curves survives after the crossing. Finally, an increase of the $Nu_\omega(Re)$ slope is observed after the crossing. This is a consequence of the change in the mechanism of the momentum transfer in the ultimate regime. As explained above, the turbulence penetrates the boundary layers and dominates the momentum transfer, which increases. This improvement of the momentum transfer is reflected as an increase of the $Nu_\omega(Re)$ slope, when shown in logarithmic scale.

The variation of the dimensionless torque with the radius ratio, η, was already investigated in the first studies done by Wendt [4] and Taylor [32]. Recently, Ostilla-Mónico *et al.* [8, 7] have dealt numerically with the radius ratio dependence of the flow for purely inner rotation, focusing on the transition to the ultimate regime. In

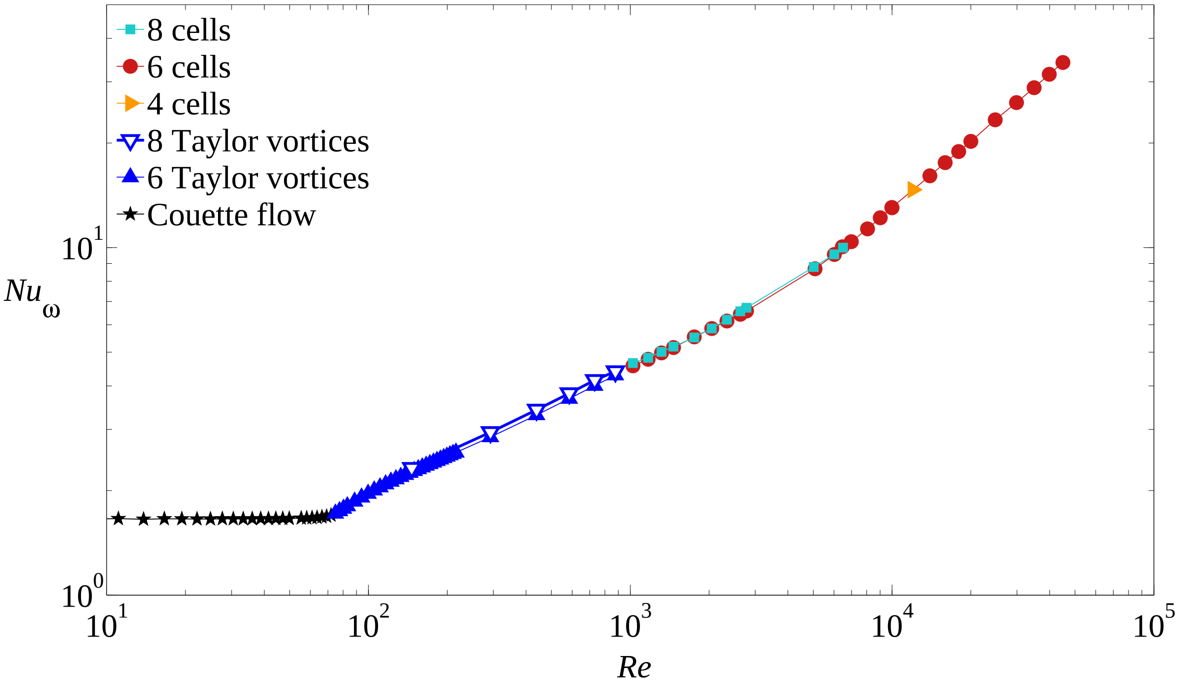

Figure 4.21: Rescaled torque, Nu_ω, as a function of Re for different flow states in a system with $\eta = 0.6$ and $\Gamma = 6.8$.

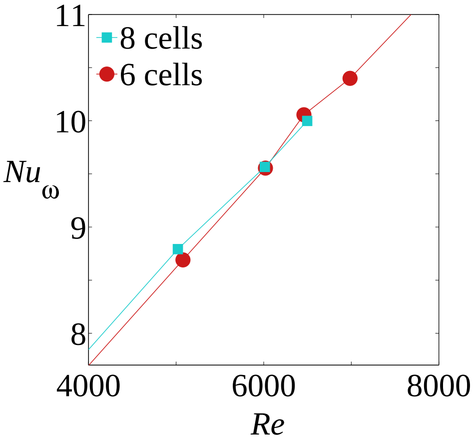

Figure 4.22: Rescaled torque, Nu_ω, as a function of Re for different flow states in a system with $\eta = 0.6$ and $\Gamma = 6.8$ to show the intersection between the curves.

the following, the effect of the radius ratio, η, on the ω-Nusselt number is analysed for different systems.

Figure 4.23 displays the evolution of Nu_ω as a function of the Reynolds number in the range $40 < Re < 45\ 000$ for three different radius ratios, $\eta = 0.6$, 0.909 and 0.973. As explained in 4.4.1, at low Re, in the Couette laminar regime, the three curves are shifted up due to the end effects that introduce an additional torque with respect to the theoretical laminar torque calculated for an infinite cylinder. This increase of torque induced by the end effects appears to be important when analysing the torque at large Re. Therefore, it is proposed to use a new rescaling by using the torque measured in the laminar regime, T_{lam}^{exp}, as previously done.

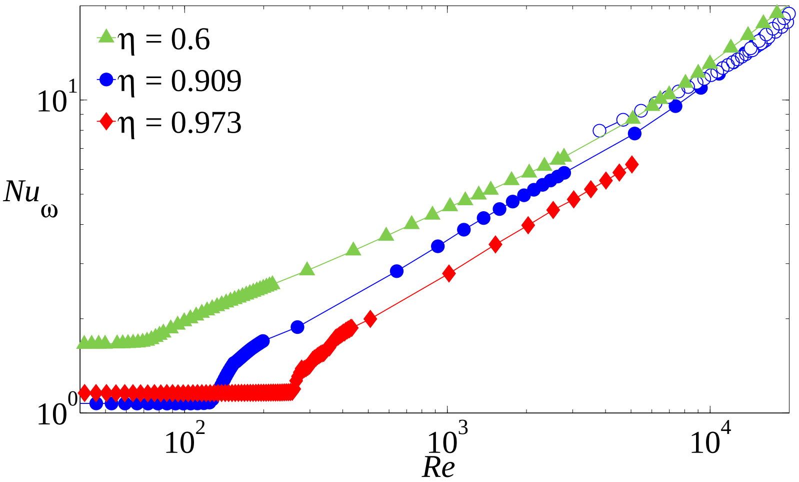

Figure 4.23: Rescaled torque, Nu_{ω}, as a function of Re in systems with three different radius ratios. The aspect ratios, Γ, are: 6.8, 30 and 100, respectively.

Figure 4.24 depicts the variation of the rescaled torque T/T_{lam}^{exp} with Re in the systems with $\eta = 0.6$, 0.909 and 0.973. The results from Merbold *et al.* [13] with $\eta = 0.5$ are added for comparison. The experimental set-up used by these authors has been described in chapter 3, where the torque is only measured in the centre of the inner cylinder, so the end effects are not taken into account. The results of Wendt [4] are also added for three different radius ratios, $\eta = 0.68$, 0.85 and 0.935. Clearly, there is an influence of the radius ratio on the level of Nu_{ω}, where the systems with $\eta = 0.6$ and 0.973 have the lowest levels of T/T_{lam}^{exp}. Then, the rest of the data superpose in a wide range of Re. However, as we are comparing very different systems, in which the torque is measured in distinct ways, we can not extract strong conclusions about the variation of T/T_{lam}^{exp} with η. Nevertheless, the slope of the curves can be compared. It was already explained that the flow in the systems with $\eta = 0.6$ and 0.909 undergoes a transition to the ultimate regime at $Re = 6090$ and 12 600, respectively. This transition induced a change in the slope of the curve $Nu_{\omega}(Re)$, that can be observed in figure

4.24. A similar change in the slope was reported by Merbold *et al.* [13] at $Re = 75\ 000$ in the system with $\eta = 0.5$, probably due to the transition to the ultimate regime. The slope after the transitions are similar in all the systems. Also, in the curves of Wendt [4] for $\eta = 0.68$ and 0.85 the slope is similar.

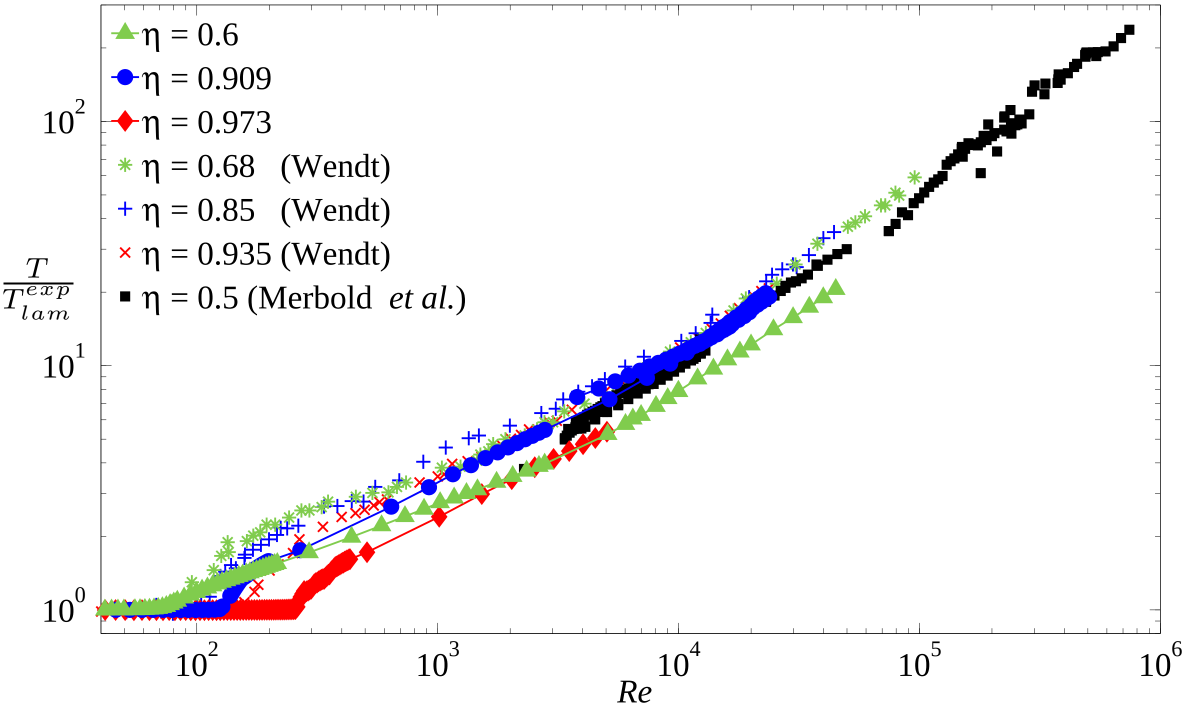

Figure 4.24: Rescaled torque, T/T_{lam}^{exp}, as a function of Re in systems with different radius ratios. The experimental data from Wendt [4] and Merbold *et al.* [13] are added for comparison purposes.

4.5 Power law fitting

In chapter 2 it was explained that the motivation behind seeking scaling laws is to find the universal behaviour of momentum transfer in turbulent flows. Particularly, the analogy with Rayleigh-Bénard system is interesting as the driving mechanism of momentum transfer and heat transfer are comparable [46, 44]. The dependence of Nu_ω on Re can be described as $Nu_\omega = \mathcal{A}Re^{\alpha-1}$, where $\mathcal{A}$ is the pre-factor and α is the exponent. In the following, the variation of both parameters will be discussed.

4.5.1 Exponent

In turbulent flows, at very high Re, the exponent, α, tends to 2, according to the Kolmogorov's theory of isotropic and homogeneous turbulence [47, 16]. For intermediate Reynolds numbers α varies and depends on several parameters. In figure 4.25 the evolution of α with Re is shown for the three systems studied with $\eta = 0.6$, 0.909 and 0.973. Here, $\alpha - 1 = \partial(\log_{10} Nu_\omega)/\partial(\log_{10} Re)$ is calculated for each system as a function of the Re using sliding least-square fit [16, 6, 14, 13] over intervals between $0.1 < \Delta(\log_{10} Re) < 0.4$. The results are compared with those of Ravelet *et al.* [14] with $\eta = 0.917$, Lim and Tam [15] with $\eta = 0.892$, Lewis and Swinney [6] with $\eta = 0.714$ and Merbold *et al.* [13] with $\eta = 0.5$.

Around $Re \approx 400$, the flow is chaotic and exhibits some turbulent patches. It is possible to test the scaling law (2.31). For $400 < Re < 4000$ the behaviour of the exponent is constant. The points for $\eta = 0.6$ are around $\alpha = 1.4$, in agreement with those of Ravelet [14]. And the points for $\eta = 0.909$ and 0.973 are around $\alpha = 1.5$, in agreement with those of Lim and Tan [15]. The common feature in this range, in which the turbulence starts appearing in the flow, is that the exponent remains constant.

At $Re > 4000$ the turbulence is well established in the flow and the exponent increases again. Note that in the case of $\eta = 0.909$ there is a large number of points, corresponding to the different numbers of vortices found. In the case of $\eta = 0.6$ the exponent reaches a constant value at $Re = 9200$. This occurs after the crossing of

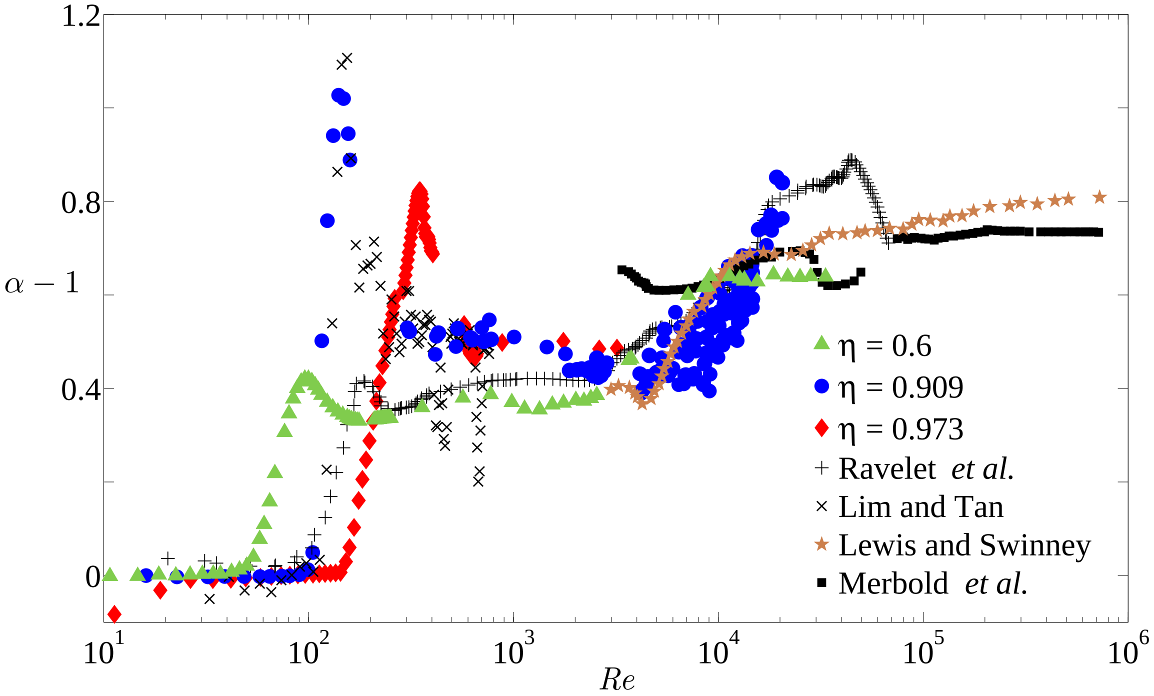

Figure 4.25: Evolution of the exponent, α, with Re in three systems with different radius ratios. The data are compared with those of Ravelet *et al* [14] with $\eta = 0.917$, Lim and Tan [15] with $\eta = 0.892$, Lewis and Swinney [6] with $\eta = 0.714$ and Merbold *et al.* [13] with $\eta = 0.5$.

the $Nu_\omega(Re)$ curves at $Re = 6090$, where the slope of such curve also changes. The same trend is observed in the case of Lewis and Swinney [6], in which the behaviour of α varies after the change in slope of the $Nu_\omega(Re)$ curves and the crossing of its two branches. A similar behaviour is observed in the case of Ravelet *et al.* [14], where the exponent grows smoothly at the same Reynolds number, $Re \approx 13\ 000$, where a change in slope of the $Nu_\omega(Re)$ curve is observed. A drop of the exponent takes place at $Re \approx 40\ 000$. In the case of Merbold *et al.* [13], the change in the behaviour of α occurs at $Re \approx 75\ 000$. In figure 4.24 it can be observed a change in the slope of the torque at the same Re. The value of α is also related to the transition to the ultimate regime. Actually, Ostilla-Mónico *et al.* [7] realised that the ultimate regime is characterised by an exponent $\alpha > 5/3$, in analogy with the Rayleigh-Bénard system. In all the cases included for comparison, α is larger than $5/3$. In the case of $\eta = 0.6$ the exponent is slightly below this threshold and equals 1.64. This could be explained by the small aspect ratio of this system, $\Gamma = 6.8$.

Once the variation of α with Re has been analysed, now we focus on the dependence of the exponent with the number of vortices. Figure 4.26(a) displays the variation of $\alpha - 1$ as a function of Re for different numbers of cells between $4000 \lesssim Re \lesssim 21\ 000$. A dependence of the exponent with the number of vortices is found, so the smaller is the number of vortices, the larger is the exponent. Actually, the meaning of α is related to the viscosity dependence of the torque [16]. The Kolmogorov assumption assumes $\alpha = 2$ for fully developed turbulence at extremely high Re [47, 16]. Any deviation from $\alpha = 2$ implies a particular form of velocity fluctuations. In fact, this is considered as an upper limit and no numerical [8] or experimental [48, 49, 50] study has managed to attain this limit even at $Re = \mathcal{O}(10^6)$. In a flow system with a given number of vortices, the form of the velocity fluctuations is constrained by the presence of large-scale vortices and cannot be completely random. Hence, the less number of vortices there are in the flow, the largest is the level of turbulence and the higher is the exponent. Modern investigations using particle image velocimetry [38, 82] aim to quantify the velocity fluctuations and estimate the average turbulent kinetic energy dissipation rate.

A new scaling of the Reynolds number based on the mean aspect ratio of the cells, $\bar{l}Re/d$, depicted in 4.11, is proposed for the exponent in figure 4.26(b). A partial overlap of the data is found at $\bar{l}Re/d > 17\ 000$, most probably when the ultimate regime starts. This suggests that the size of the cells is an important parameter before the transition. However, in the ultimate regime the role of turbulence is more important than the one of the vortices.

The principal feature that we wish to highlight is the systematic dependence of the scaling on the number of vortices in the flow. For situations where the number of cells is small, the flow is less constrained by the cells. Therefore, the turbulent flow will exhibit larger velocity fluctuations, leading to higher turbulence and a larger α. For situations were the number of cells is large, the flow is more constrained by the cells and the velocity fluctuations are weaker, leading to a smaller value of α.

According to Ostilla-Mónico *et al.* [7], the ultimate regime is characterised by an

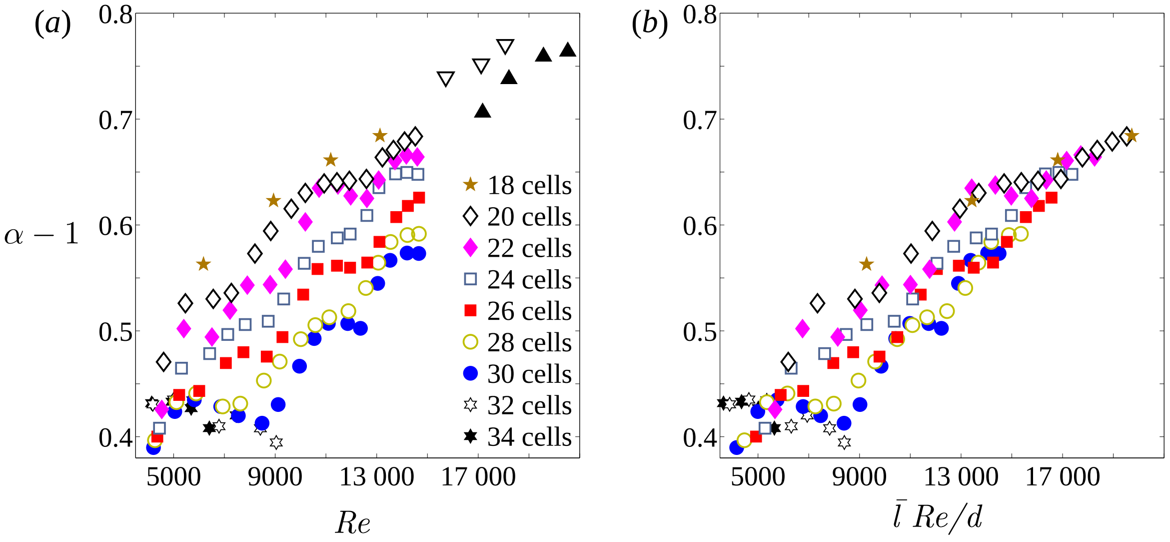

Figure 4.26: Evolution of the exponent, α, for different numbers of cells. The black triangles (▲) and the empty triangles (▽) represent data obtained using low viscosity silicone oil. (*a*) $\alpha - 1$ as a function of Re and (*b*) $\alpha - 1$ versus $\bar{l}Re/d$, based on the averaged height of the cells, $\bar{l}$.

exponent, $\alpha > 5/3 \approx 1.67$. A recent experimental work [51] has shown that at very high Reynolds numbers, $R = \mathcal{O}(Re^6)$, the exponent reaches values of 1.78. In numerical simulations an exponent of 1.88 has been reached at $Re = \mathcal{O}(Re^5)$. In our case, even at much lower Reynolds numbers, $Re = \mathcal{O}(Re^4)$, exponent with values above 1.75 have been attained in the case of small number of vortices (see the black triangles (▲) and the empty triangles (▽) in figure 4.26). However, in the case of 30 cells the exponent only reaches a value of 1.57. This indicates that if the number of vortices is reduced, similar levels of turbulence can be attained than in flows at higher Re but larger number of cells.

4.5.2 Pre-factor

So far, only the exponent had been analysed when performing scaling laws of the torque [16, 6, 15, 44, 14, 13, 8, 7], without taking into account the role of the pre-factor, $\mathcal{A}$, in (2.31). In the following analysis, the dependence of $\mathcal{A}$ on Re and the number of vortices is analysed.

In figure 4.27 the evolution of the pre-factor, $\mathcal{A}$, for different numbers of vortices in a system with $\eta = 0.909$ and $\Gamma = 30$ is presented. The data corresponding to the system with $\eta = 0.6$ are also included. The values of $\mathcal{A}$ are greater for larger number of vortices and decrease for increasing Re numbers. Two upward peaks are observed at approximatively $Re = 8500$ and $Re = 12\ 300$. These upward peaks appear at the same Re numbers that the two downward peaks observed in figure 4.26(a).

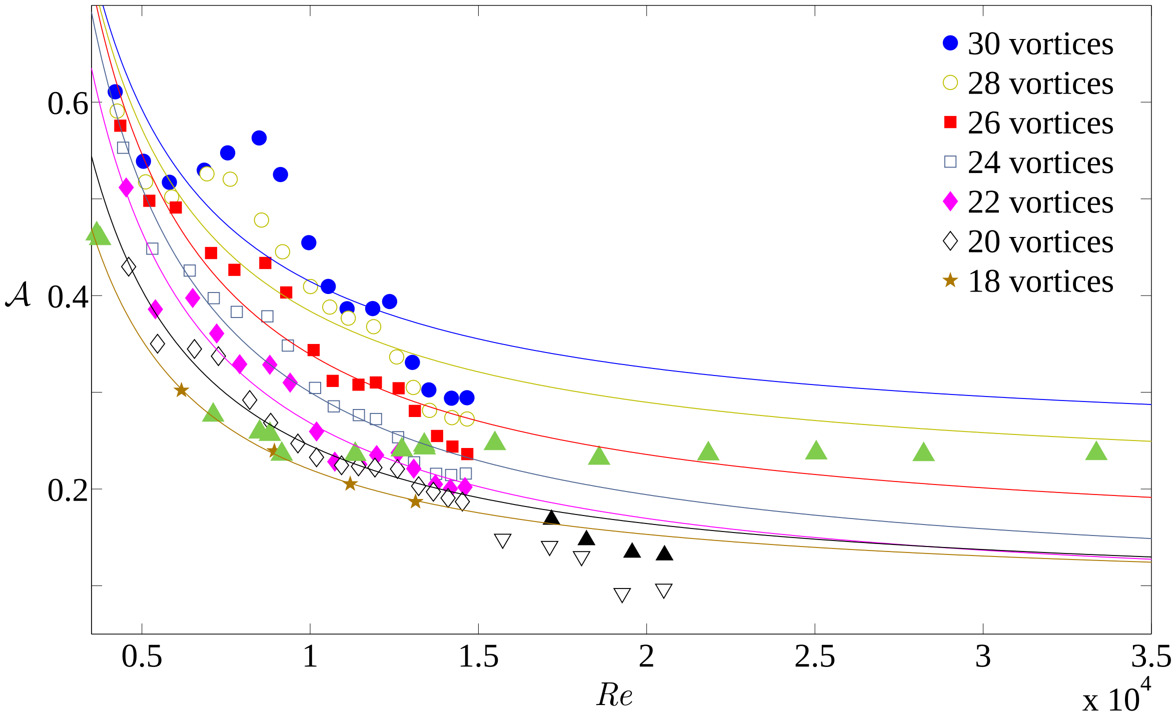

Figure 4.27: Evolution of the pre-factor, $\mathcal{A}$, with Re, for different numbers of vortices. The continuous line corresponds to a fitting given by (4.2). The black triangles (▲) and the empty triangles (▽) represent data obtained using low-viscosity silicone oil. The green triangle (▲) represent the values in the system with $\eta = 0.6$.

Regarding the tendency of the curves, the following fit is proposed.

$$\mathcal{A} = c_1 + \frac{c_2}{Re}. \tag{4.2}$$

where $c_1 = \lim_{Re\to\infty} \mathcal{A}$ and c_2 is related to the dependence of $\mathcal{A}$ on Re. When Re is smaller or of the same order of c_2, $\mathcal{A}$ depends on Re. On the contrary, when $Re \gg c_2$, the term in (4.2) depending on Re is negligible and $\mathcal{A}$ becomes constant and equals c_1. The fit curves corresponding to (4.2) are presented in figure 4.27 as continuous lines. Although they do not overlap well on the points, due to the two upward peaks, these curves estimate the behaviour of $\mathcal{A}$ at the largest Reynolds numbers, suggesting that the curves reach a constant value and the pre-factors are no longer dependent on Re. Moreover, the range of Re where the pre-factors seem to become constant coincides with the crossing of the $Nu_\omega(Re)$ curves. The values of c_1 and c_2 are shown in table 4.2. If this is compared to the system with $\eta = 0.6$, the suggestion is confirmed. Actually, the pre-factor reaches a constant value when $Re > 9200$, in the same region where the exponent α also becomes constant. As explained before, this coincides with the ultimate regime of turbulence.

The main results that we want to stand out is the change in the behaviour of $\mathcal{A}$ before and after the transition to the ultimate regime. Before the transition, the pre-factor depends on Re. In the ultimate regime, the pre-factor is constant. This implies that before the transition there is not a unique exponent α. So, the exponent is a local property of the flow strongly dependant on Re. In the ultimate regime, the exponent is a global property of the flow, although it still depends on Re, as shown in different works [16, 6, 13, 8, 7].

n_v	30	28	26	24	22	20	18
c_1	0.2365	0.1955	0.1322	0.0883	0.0709	0.0837	0.0860
c_2	1780.4	1884	2070	2117	1974	1611	1342

Table 4.2: Values of the constants c_1 and c_2 in (4.2) for different numbers of vortices.

4.6 Transition to the ultimate regime

The transition to the ultimate regime in Couette-Taylor flow was first observed by Latrhop *et al.* [16] and was explained as a change from centrifugal turbulence to shear-driven turbulence. This transition involves several changes in the features related to the torque: a variation of the slope in the evolution of the torque with the rotational speed, a crossing between the different branches of the $Nu_\omega(Re)$ curve for different numbers of vortices, a progressive growth of the exponent of the scaling law once $\alpha = 1.67$, a change in the axial diffusion coefficient and different wall shear stress characteristics [16, 7]. Moreover, we have shown a clear behaviour of the pre-factor, $\mathcal{A}$, after this transition, which becomes constant in this regime. In the following, the dependence of the Reynolds number in the transition to the ultimate regime, Re_T, on the radius ratio, η, is analysed. A dependence on the aspect ratio Γ is also observed.

In the numerical work of Ostilla-Mónico *et al.* [8, 7] the η-dependence of the transition to the ultimate regime was analysed. For $\eta \gtrsim 0.7$ the threshold appears at a constant Taylor numbers which is equivalent to $Re = \mathcal{O}(10^4)$. However, for $\eta \lesssim 0.7$ the critical point increases with decreasing radius ratios. Moreover, it was suggested that the transition is independent of the wavelength of the cells. They gave three reasons for which the global effect of reducing η leads to an increase of Re_T. First, when the gap is large compared to the radii of the cylinders, *i.e.*, when the curvature is pronounced, the fluctuations in the outer cylinder are reduced with respect to the inner cylinder. Second, the convexity of the inner cylinder and the concavity of the outer one tend to stabilise and destabilise the flow, respectively [83, 84, 85]. And third, the shear close to the outer cylinder is reduced for large gaps. All this leads to an asymmetry of the boundary layers that delays the transition to the ultimate regime of turbulence.

In figure 4.28 it is displayed different Re_T as a function of η. In our case, the point for $\eta = 0.6$ represents the crossing of the $Nu_\omega(Re)$ curves, that coincides with the change of slope of this curve. In the case of $\eta = 0.909$, the point represents the average Re where all the intersection of the $Nu_\omega(Re)$ curves take place. A comparison with several works is done.

For Lewis and Swinney [6] the point at $Re_T = 13\ 000$ for $\eta = 0.724$ is based on the change in slope of the evolution of the exponent, α, with Re, and in the crossing of the $Nu_\omega(Re)$ curves for two flows with different numbers of vortices. In the simulations of Ostilla-Mónico *et al.* [7] the points at $Re_T = 59\ 300$, $14\ 000$ and $16\ 500$ for $\eta = 0.5$, 0.714 and 0.909, respectively, are based on the onset of turbulence in the boundary layer, that coincides with a change in slope in the $Nu_\omega(Ta)$ curves. In the experimental study of Merbold *et al.* [13] a change in slope in the $Nu_\omega(Re)$ curve is observed at the $Re_T = 75\ 000$ for $\eta = 0.5$. Huisman *et al.* [17] identified a change to a logarithmic boundary layer at $Re_T = 25\ 700$ for $\eta = 0.716$. For Ravelet *et al.* [14] the point is based in the change in slope of the $Nu_\omega(Re)$ curve at the $Re_T = 10\ 380$ for $\eta = 0.917$.

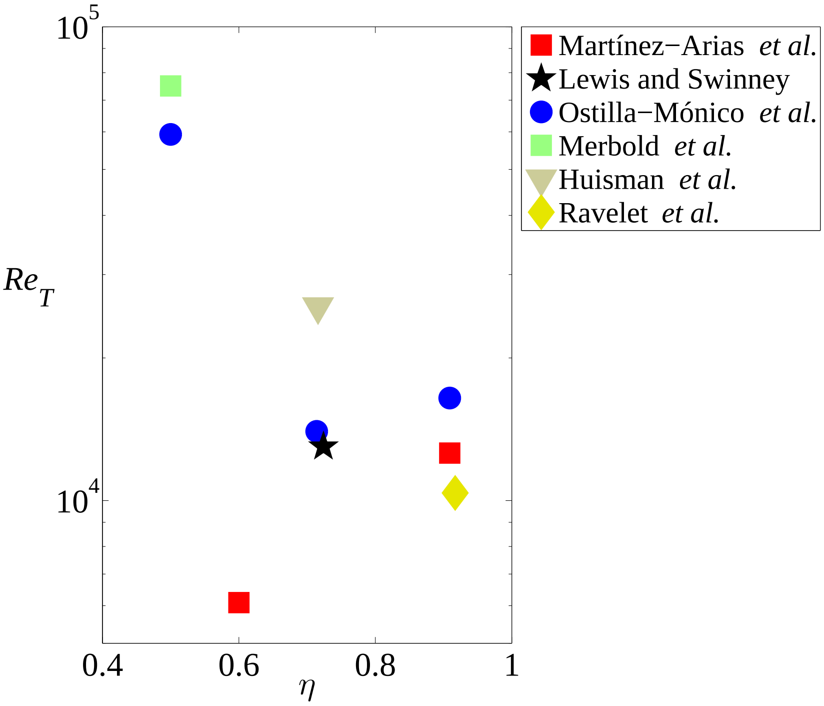

Figure 4.28: Reynolds number in the transition to the ultimate regime, Re_T, as a function of the radius ratio, η. Points from different works [16, 14, 17, 13, 9, 7] are added for comparison purposes.

Regarding the figure 4.28 the transition to the ultimate regime seems to be little affected by the radius ratio when $\eta \gtrsim 0.7$. However, for $\eta \lesssim 0.7$ the transition is delayed with decreasing η. This is in agreement with the explanation of Ostilla-Mónico *et al.* [7]. Nevertheless, the point with $\eta = 0.6$ strongly differs. This could be explained by the short aspect ratio, $\Gamma = 6.8$, that advances the transition to the ultimate regime. In the other experimental works, the aspect ratio is larger than 20. In the numerical works, the periodic boundary conditions do not take into account the effect of the boundary layer. Therefore, this result indicates that the transition to the ultimate regime is affected by the aspect ratio of the system.

4.7 Conclusions

This chapter have dealt with the torque that turbulent flows exert on the inner cylinder when only this cylinder rotates. Torque measurements in three systems with different radius ratios, $\eta = 0.973$, 0.909 and 0.6, have been carried out up to Reynolds numbers of 45 000. The effect of the radius ratio and the number of vortices have been studied. Flow visualisation have been performed to count the number of vortices.

The flow visualisations have shown the different transitions that the flow undergoes, starting from the laminar Couette flow, until reaching the turbulent regime. The procedure to select the number of vortices has been illustrated through a spatio-temporal diagram and then, the multiple turbulent states that can be established in the flow have been shown. Finally, the size of the vortices, l, has been measured and the influence of the aspect ratio of the system, Γ, on the mean vortex size, $\bar{l}$, has been analysed.

The global variation of the rescaled torque, Nu_ω, with the Reynolds number, Re, has been shown. A focus on the regimes before the onset of turbulence has been made, particularly, on the laminar Couette flow, the Taylor vortex flow and the wavy vortex flow. The critical Reynolds number, Re_c, of the onset of Taylor vortices agrees well with the theory [77]. The torque measured for Taylor vortices agrees well with the analytical studies of DiPrima *et al.* [11] for the systems with large radius ratio, although the agreement is not good with the system with $\eta = 0.6$. This could be due to the small aspect ratio of this system, $\Gamma = 6.8$.

In the case of turbulent flows, the torque measurements show a clear effect of the number of vortices in the rescaled torque, Nu_ω. Before the transition to the ultimate regime of turbulence [7], the laminar boundary layers limit the momentum transfer of the turbulence, as it can not reach the cylinders. Hence, the vortices have the main role in the momentum transfer and the larger is the number of vortices, the larger is the torque they apply. In the ultimate regime, the turbulence penetrates the boundary layers [17], so it can now dominate the momentum transfer. Therefore, the higher is the level of turbulence in the flow, the larger is the momentum transfer. As the level of turbulence increases when the number of vortices decreases, flows containing a smaller number of vortices will exert larger levels of torque. As a consequence of the change in the mechanism of momentum transfer, intersections of the $Nu_\omega(Re)$ are observed. This improvement of the momentum transfer mechanism in the ultimate regime also results in an increase in the slope of the $Nu_\omega(Re)$ curves, which is observed after the crossing of the curves. Finally, an influence of the radius ratio, η, is observed in Nu_ω, although strong conclusion of the effect can not be made, due to the differences between the systems.

Power law fitting have been applied to the torque data to analyse the behaviour of the exponent, α, and the pre-factor, $\mathcal{A}$. For laminar Couette flows $\alpha = 1$, since the torque is proportional to the rotation speed of the inner cylinder. After an abrupt increase of α, corresponding to the Taylor vortices, the exponent reaches a constant value, that varies between $1.4 < \alpha < 1.5$, depending on the system. Once the turbulence appears in the flow, the exponent grows significantly. Then, after the transition to the ultimate regime, α reaches a constant value and, in some cases, still increase but smoothly. The effect of the number of vortices has also been analysed, finding that the exponent increases when reducing the number of vortices. This is related to the turbulent energy dissipation, so the less the number of vortices, the higher is the level of turbulence, and hence, the larger is α. We have demonstrated that flows with a small number of vortices and moderate Reynolds numbers, $Re = \mathcal{O}(10^4)$, presents the same level of turbulence than flows with larger number of vortices and higher Reynolds numbers, $Re = \mathcal{O}(10^6)$. When rescaling Re, using the mean aspect ratio of the cells, $\bar{l}/d$, a collapse is found at the highest Reynolds number, most probably related to the ultimate regime. With respect to the pre-factor, $\mathcal{A}$, it is found that it depends on Re before the transition, and becomes constant in the ultimate regime. This indicates that, if universal scaling laws are sought between momentum transfer and the driving force, they should be done in the ultimate regime of turbulence.

The threshold of the transition to the ultimate regime of turbulence, Re_T, has been analysed as a function of the radius ratio, η. As previously presented by Ostilla-Mónico *et al.* [7], Re_T depends on η. For systems with $\eta \gtrsim 0.7$ and aspect ratios $\Gamma \geq 20$, Re_T seems to not vary so much with η. For systems with $\eta \lesssim 0.7$ and $\Gamma \geq 20$, Re_T increases with decreasing η. We have shown that a small Γ modifies the transition to the ultimate regime, so Re_T becomes smaller.

Chapter 5

Torque of viscoelastic polymer solutions in Couette-Taylor flows

"I have not failed. I have just found 10 000 ways that will not work".

—Thomas Alva Edison

The effect of long-chain polymer addition in Couette-Taylor flow is described. Torque measurements and flow visualisations have been performed in a wide range of elastic numbers. When the fluid is pre-sheared, flow visualisations during an acceleration-deceleration cycle of the inner cylinder show that different patterns emerge when increasing the concentration of long-chain polymers. The torque presents hysteresis during the acceleration-deceleration cycles, corresponding to different patterns. With high concentrations, pairs of solitary vortices are observed when decelerating and their torque is measured. Additionally, the number of these solitary vortices is controlled through the deceleration rate of the inner cylinder. The relationships between the torque and the speed are also analysed when the fluids are not pre-sheared. Finally, when the rotation rate is large, inertio-elastic turbulence was observed and the torque fluctuations that arise have been analysed.

5.1 Introduction

When a viscoelastic polymer solution is employed as working fluid in a Couette-Taylor flow, elastic properties can give rise to the inertio-elastic instabilities, or pure elastic instabilities as shown by Larson *et al.* [86]. Special patterns, such as localised steady vortex pairs of large wavelength, called tall Taylor cells by Beavers and Joseph [87] and Haas and Bühler [88] or diwhirls by Groisman and Steinberg [89, 90], can arise. The challenge when dealing with polymer solutions is the increase of dimensionality of the parameter space, because of new parameters that depend on the rheological properties of the fluid.

After pioneering studies done by Denn and Roisman [91], there has been a growing interest in viscoelastic instabilities in the Couette-Taylor system [86, 89, 57, 92]. Theoretical studies are nowadays complemented by numerical calculations using viscoelastic models, like the upper-convected-Maxwell fluid model [93] or the Oldroyd-B model [94] and finite extensible nonlinear elastic (FENE) dumbbell models [95, 96, 97, 98]. Although these studies were able to reproduce many flow properties observed in experiments such as standing waves or diwhirls, the torque and wavelength selection mechanism have been less investigated.

The present study considers high-molecular-weight linear polymer poly(ethylene oxyde) (PEO) in a mixture of water and poly(ethylene glycol) (PEG). The properties of aqueous PEO solutions and mixtures of PEO and PEG are well documented in several studies [56, 57, 58, 59, 60, 61, 62, 63, 64, 65, 99, 100, 101]. Different stability diagrams of different regimes in Couette-Taylor flow are available [57, 65, 67]. Recently, Dutcher and Muller [79, 65] summarized most of previous experimental studies on viscoelastic Couette-Taylor flow. They identified inertial and inertio-elastic transitions depending on the viscoelasticity of the fluids (viscosity ratio and elastic number, defined below). The transition sequences, including elastically dominated turbulence, were characterized using patterns from spatio-temporal diagrams. Another technique to detect the transition is to monitor the torque that the fluid exerts on the inner cylinder as done by Denn and Roisman [91], Yi and Kim [102] and Groisman and Steinberg [92]. Denn and Roisman [91] provided torque data for several polymer solutions, including PEO of 4×10^6 g/mol. Yi and Kim [102] studied dilute polyacrylamide solutions. Groisman and Steinberg [92] also studied polyacrylamide solutions and reported hysteretic behavior for a single large elastic number.

Our objective was to carry out a systematic study of the dependence of the flow patterns and the torque on different rotation speeds and different concentrations of PEO during slow acceleration/deceleration cycles. The chapter is organised as follows. In §5.2 the experimental methodology is presented. In §5.3 results about pre-sheared fluids are presented. The patterns that appear are illustrated in spatio-temporal diagrams, the torque is analysed and the pairs of solitary vortices that appear during deceleration are analysed. In §5.4 results concerning fluids non pre-sheared are presented. The fluctuations in the inertio-elastic turbulent regime are analysed. The conclusion is presented in §5.5.

5.2 Experimental methodology

5.2.1 Dimensionless numbers

We use the Couette-Taylor system with $\eta = 0.909$ and $\Gamma = 30$ described in §3.1. The addition of polymer to the fluid increases the parameter space of Couette-Taylor flow. Hence, new parameters have to be defined to quantify the new effects on the flow. The shear rate is defined as,

$$\dot{\gamma} = \Omega r_i/d \tag{5.1}$$

which is the deformation rate of a fluid layer parallel to the cylinders surfaces. The Reynolds number has been previously defined in (2.9), but using the shear rate it can be defined as,

$$Re = \dot{\gamma}\lambda_v, \tag{5.2}$$

where $\lambda_v = d^2/\nu$ is the viscous diffusion time across the gap. The dimensionless viscous diffusion time across the gap is defined as,

$$\tau_v = \frac{t}{\lambda_v} = \frac{\nu t}{d^2}. \tag{5.3}$$

To quantify the effects of the elasticity on the flow, the Weissenber number, which is the product of $\dot{\gamma}$ and the relaxation time, λ_e, is defined as,

$$Wi = \dot{\gamma}\lambda_e. \tag{5.4}$$

The elastic number, which is the ratio between the relaxation time and the viscous time is defined as,

$$El = \frac{\lambda_e}{\lambda_v} = \frac{Wi}{Re}. \tag{5.5}$$

The viscosity ratio is,

$$S = \frac{\mu_p}{\mu_s}, \tag{5.6}$$

where μ_p is the polymer contribution to the viscosity and μ_s is the solvent viscosity.

5.2.2 Rheology summary

In §3.2 the properties of the viscoelasctic fluids were presented and are summarised in table 5.1. The elastic number, El, has been calculated using the elongational relaxation time measured with the CaBER, as it is the longest relaxation time of the fluid.

5.2.3 Experimental protocol

During the experiments, the rotation speed of the inner cylinder was varied with a constant acceleration and deceleration $\Delta\Omega/\Delta t = \pm 5.2 \times 10^{-3}$ rad/s^2. This ramping rate was selected, so the dimensionless acceleration is below the criterion of Dutcher and Muller [41] that states that the Newtonian Couette-Taylor flow instability is independent of the acceleration when $\Delta Re/\Delta\tau_v \lesssim 0.60$. As τ_v is larger than any relaxation time of the polymer solution, the acceleration used here is slow enough to allow for the

C_{PEO} (ppm)	λ_v (s)	S	λ_e (ms)	El
76	3.128	0.094	171	0.05
100	3.109	0.100	201	0.06
150	2.819	0.213	254	0.09
300	2.301	0.487	395	0.17
1000	0.753-1.257	1.720-3.542	823	0.66-1.09

Table 5.1: Properties of the different PEO solutions dissolved in an aqueous solvent containing 7% PEG, whose viscous diffusion time is, $\lambda_v = 3.420$ s. Note that for the solution with 1000 ppm the minimum and maximum values of λ_v, S and El correspond to the shear thinning of the viscosity.

elastic stress response.

When viscoelsatic fluids are poured for the first time in the Couette-Taylor system and the inner cylinder is submitted to an acceleration, it is observed that the first instability does not appear at the same $\dot{\gamma}$, if the experiment is repeated. Actually, this critical shear rate is delayed for several repetition of the experiment, until the critical $\dot{\gamma}$ becomes constant and the experiments are reproducible. In order to get reproducible results, a pre-shear at a constant shear rate slightly larger than the critical shear for instabilities was applied for sufficiently long time until the torque reached a constant value. After using this protocol, the critical $\dot{\gamma}$ is constant. In figure 5.1 the evolution of the torque, T, with the shear rate, $\dot{\gamma}$, is displayed for flows containing different concentrations of PEO. The black curves correspond to fluids without pre-shear and the red ones to pre-sheared fluids. In the case of the small concentrations, 76 ppm, no difference is observed before and after the pre-shear. However, for larger concentrations, the critical $\dot{\gamma}$ for the transition appears at higher values in the case of pre-sheared fluids. In the case with 100 ppm, the curve corresponding to the pre-sheared fluid (−−) lays above the curve without pre-shear (–). This results may indicate that the polymer chains are entangled when the fluid is prepared. Then, when the fluid is submitted to a certain level of shear stress the polymer chains untangle.

This issue introduces a new complexity in the study of viscoelastic fluids in Couette-Taylor flow. For this reason, we have performed different types of analyses in fluids

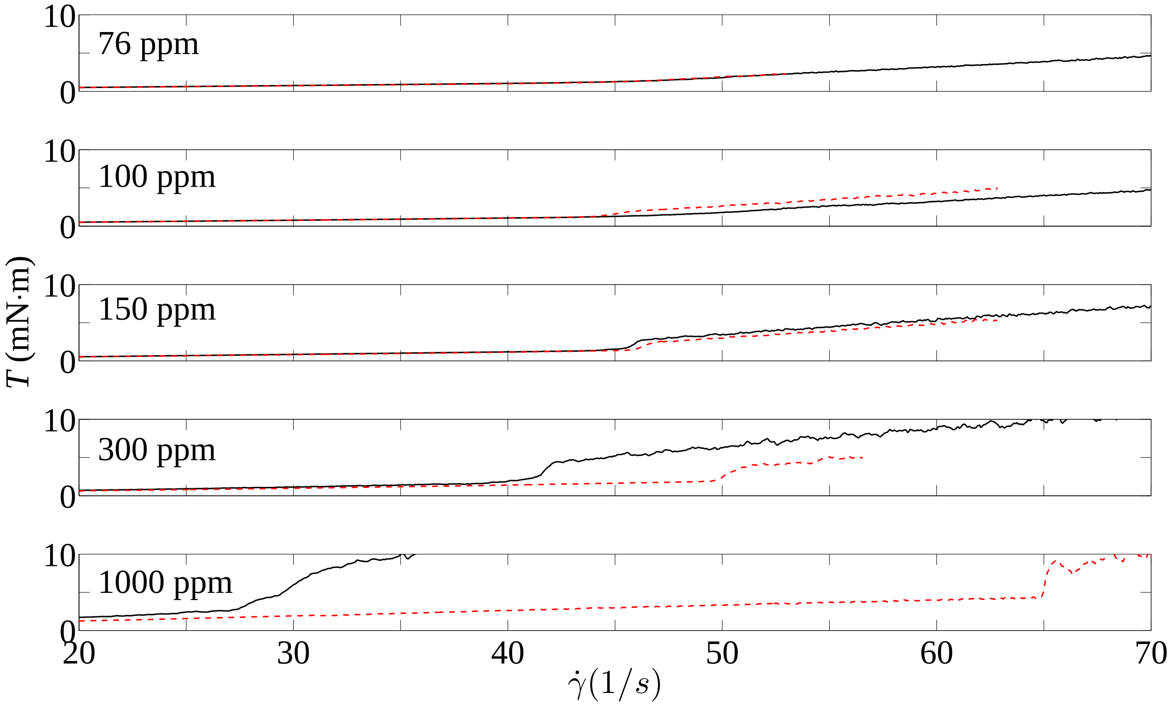

Figure 5.1: Torque, T, as a function of shear rate, $\dot{\gamma}$, for fluids containing different concentrations of PEO dissolved in 7% PEG aqueous solution. The black curves (–) are fluids without pre-shear and the red curves (– –) are pre-sheared fluids.

without pre-shear and fluids with pre-shear that will be treated in different sections.

5.2.4 Degradation

The early studies from McGary [103] showed that PEO solutions are susceptible of degradation due to mechanical, thermal, oxidative or aging processes. Dutcher and Muller [65] showed that aqueous solutions of PEG and PEO age faster than aqueous solutions of PEO in 47% glycerol. To circumvent the drawback of degradation due to processes related to the lifetime of the solutions, the fluids are always used at the third day after preparation. However, the mechanical degradation is still unknown. In order to test the limit at which the fluid are mechanically degraded, they were sheared up to a high $\dot{\gamma}$ to test their responses while monitoring the torque. The fluid with 1000 ppm of PEO, was sheared up to the highest shear rate reachable in our Couette-Taylor system in an acceleration-deceleration cycle. Figure 5.2 reports the torque as a function of shear rate for all the solutions and for the solvent. The first transition is identified by an abrupt change in slope at low shear rate and an increase in the amplitude of torque fluctuations. At higher $\dot{\gamma}$ the level of fluctuations decreases significantly and the vortices resemble turbulent Taylor vortices as in a Newtonian solution, at $\dot{\gamma} \simeq 200$, 200, 220, 265 and 400 s^{-1} for concentrations of 76, 100, 150, 300 and 1000 ppm, respectively. In the case of 1000 ppm, the following steps of the curve correspond to a change in the number of vortices that reduces the torque further, as shown in chapter 4. During the deceleration, the torque significantly reduces down to the level of the solution without PEO. This, together with the fact that the torque fluctuations are reduced, suggests that the fluid has lost some of its viscoelastic properties.

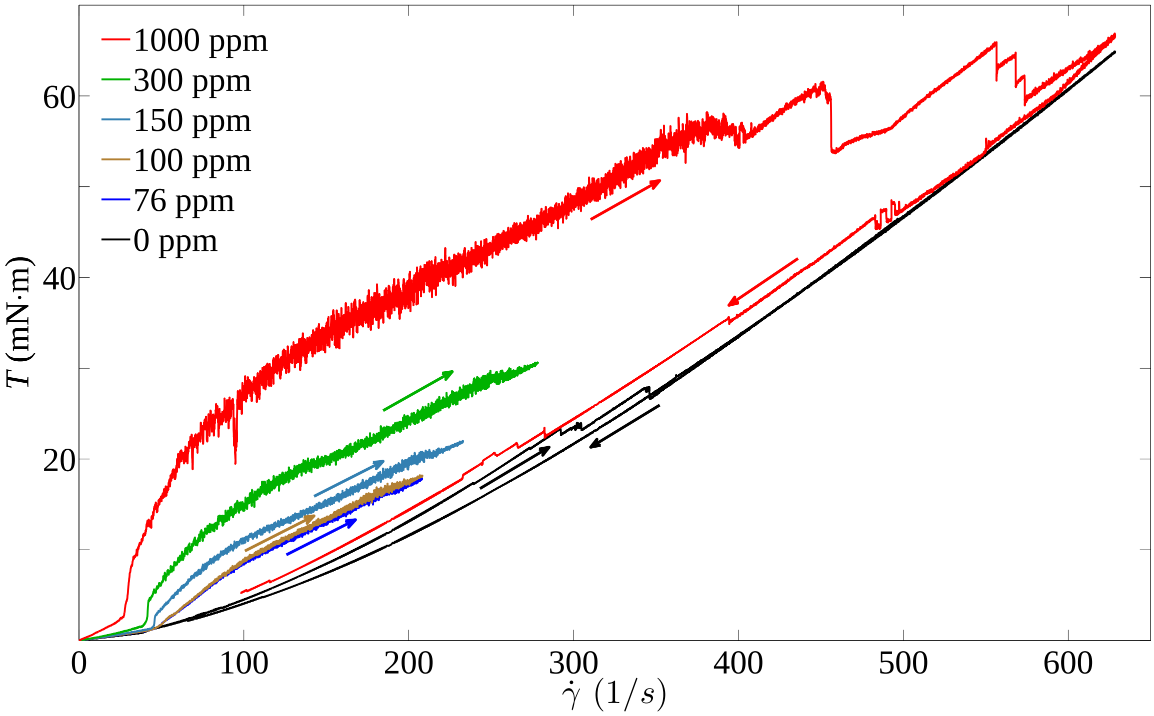

Figure 5.2: Torque, T, as a function of shear rate, $\dot{\gamma}$, for solutions containing different concentrations of PEO dissolved in a 7% PEG aqueous solution. The solvent (0 ppm) and the solution with 1000 ppm were submitted to an acceleration and deceleration cycle, so the up- and down-arrows indicate acceleration and deceleration, respectively.

5.3 Pre-sheared solutions

As explained in 5.2.4, the critical $\dot{\gamma}$ for the first instability is reproducible if the fluids have been previously pre-sheared. This section deals with fluids that have been pre-sheared.

5.3.1 Visualisations

The patterns that appear in a Couette-Taylor flow when using a viscoelastic solution are different from those in a Newtonian fluid, because of the effect of elasticity. The transitions that the fluid undergoes are distinct depending on the elastic number, El, and do not occur at the same values of Re or Wi. Through flow visualisations, the patterns that appear when accelerating and decelerating the inner cylinder with fluids containing 76, 100, 150, 300 and 1000 ppm of PEO are analysed.

Figures 5.3(a) and (b) present the spatio-temporal diagrams of a solution with 76 ppm of PEO ($El = 0.05$) with the inner cylinder accelerating and decelerating, respectively. At low shear rate, during the acceleration, the laminar Couette flow is progressively replaced by Taylor vortices. The critical Re is at 133, indicating that the fluid is destabilized compared to the Newtonian case for which the transition happens at $Re = 135$. According to the non-monotonous behavior of the stability boundaries found earlier [57], this 76 ppm solution is not far from the intertio-elastic regime, as it destabilises the flow. Between $134 < Re < 137$ the Taylor vortices present weak oscillations that appear at the ends of the cylinder and propagate to the center, giving rise to disordered oscillating flow (or noisy non-axisymmetric standing waves) between $137 < Re < 143$ [104, 89, 105, 57]. Beyond $Re = 143$ the space-time diagram shows a random pattern in which irregular lines emerge and disappear in short ranges of Re. This pattern is present for all the concentrations of PEO at high shear rates and is a characteristic of elastic instabilities [106]. A snapshot of this flow is shown in figure 5.13(a) as a pattern characterized by chaotically oscillating thin vortices. This pattern has also been named as “inertio-elastic turbulence” [104]. During the deceleration, the disordered oscillating flow is also observed for $142 > Re > 136$. However, it is not replaced by Taylor vortices but by symmetric standing waves [104, 89, 105, 57]. These standing waves observed as diagonal lines in a narrow range around the transition are typical modes of high concentrations [57].

Figures 5.3(*c*) and (*d*) present the spatio-temporal diagrams of a flow with a solution with 100 and 150 ppm of PEO ($El = 0.06$ and 0.09), respectively, with the inner cylinder accelerating. The Taylor vortices are completely developed at $Re = 135$ and $Re = 131$. The fluid with 100 ppm ($El = 0.06$) is stabilised with respect to the one with 76 ppm ($El = 0.05$). The fluid with 150 ppm ($El = 0.09$) is even more destabilised than in the case of 76 ppm ($El = 0.05$). In both cases, the range in which Taylor vortices are stable decreases with the elastic number. Afterwards, the same weak oscillations appear, as for 76 ppm ($El = 0.05$), then the disordered oscillating flow and finally the inertio-elastic turbulence pattern. The occurrence of Taylor vortices during the acceleration together with the inertio-elastic turbulence in the cases of 76, 100 and 150 ppm ($El = 0.05$, 0.06 and 0.09, respectively) indicate that these solutions present inertio-elastic instabilities.

Figures 5.4(*a*) and (*b*) present the spatio-temporal diagrams of a solution with 300 ppm of PEO ($El = 0.17$) with the inner cylinder accelerating and decelerating, respectively. In this case, during the acceleration, the laminar Couette flow is not replaced by Taylor vortices, but by symmetric standing waves, the same as in figure 5.3(*b*), that appears between $Re = 116$ and 118. This behaviour during acceleration was also observed by Baumert and Muller [105]. For $Re > 118$ the flow presents inertio-elastic turbulence. During the deceleration, the inertio-elastic turbulent pattern is directly replaced by a laminar Couette flow between $Re = 109$ and 107. Note that in both cases the patterns are not symmetric with respect to the mid height of the cylinders.

Figures 5.4(*c*) and (*d*) present the spatio-temporal diagram of a flow with a solution of 1000 ppm of PEO ($0.71 < El \geq 1.09$) with the inner cylinder accelerating and decelerating, respectively. Again, the transition from the laminar state to inertio-elastic turbulence is preceded by standing waves without any Taylor vortex. During the deceleration, at $Re > 80$ the inertio-elastic turbulent pattern is observed. Then, dark

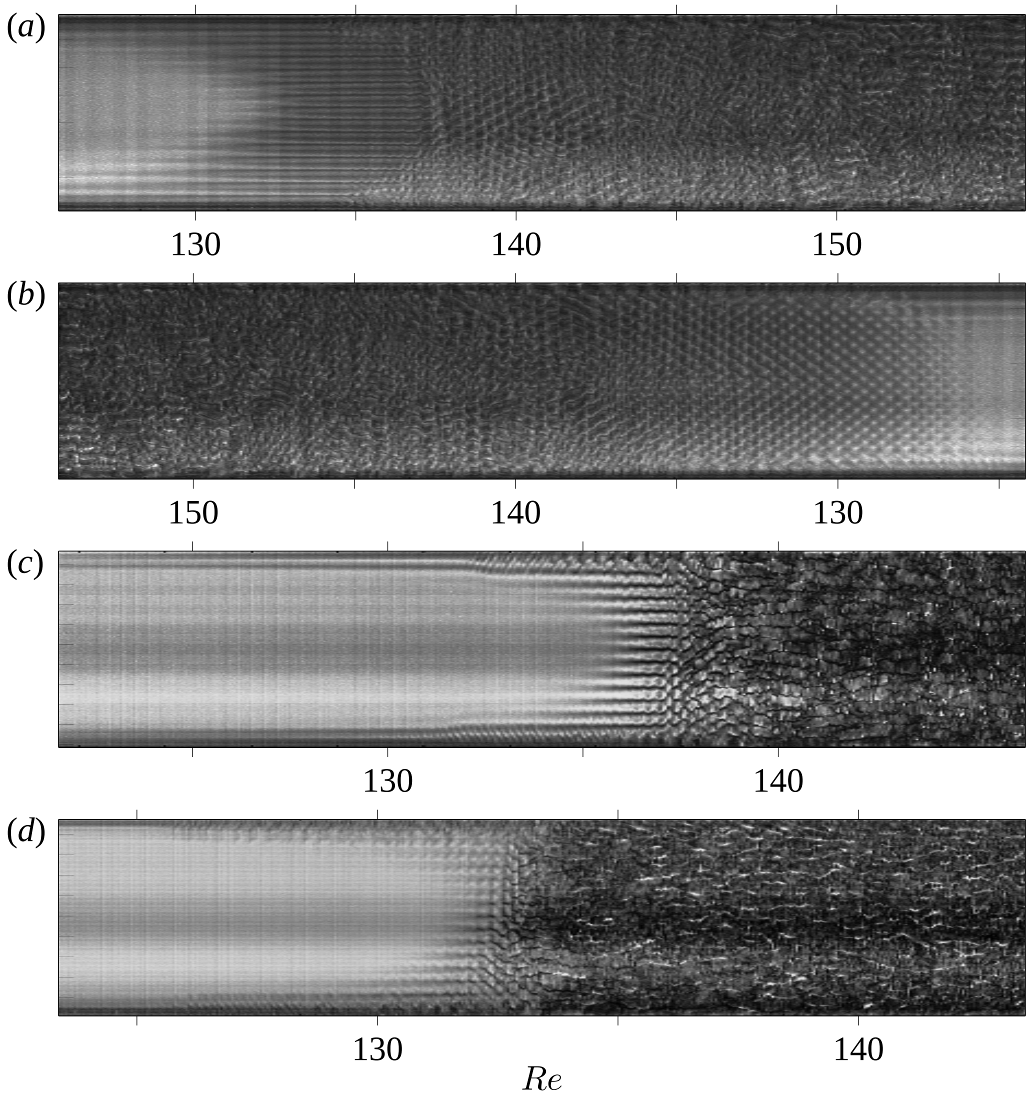

Figure 5.3: Spatio-temporal diagrams at the mid-plane of the gap over the whole height (the upper part is the top end plate and the lower part is the bottom end plate) of the flow for different concentrations of PEO dissolved in 7% PEG aqueous solution. (*a*) and (*b*) Diagrams of flows containing a 76 ppm PEO solution ($El = 0.05$) during acceleration and deceleration, respectively. (*c*) Diagram of the flows containing 100 ppm PEO solution ($El = 0.06$) during acceleration. (*d*) Diagram of the flows containing 150 ppm PEO solution ($El = 0.09$) during acceleration. Note that to convert Re into Wi, the Reynolds number has to be multiplied by El, which is also provided in table 5.1.

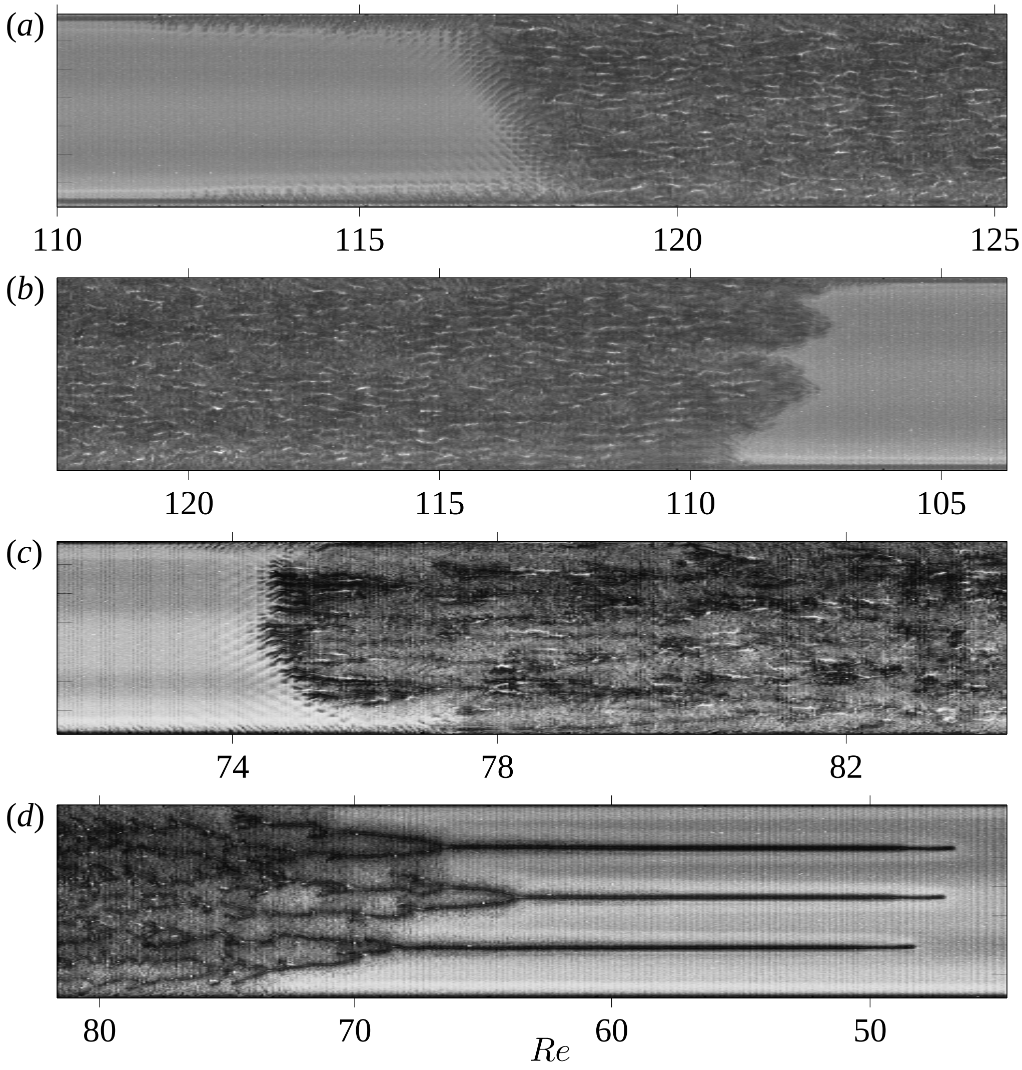

Figure 5.4: Spatio-temporal diagrams at the mid-plane of the gap over the whole height (the upper part is the top end plate and the lower part is the bottom end plate) of the flow for different concentrations of PEO dissolved in 7% PEG aqueous solution. (*a*) and (*b*) Diagrams of the flows for the 300 ppm solution ($El = 0.17$) during acceleration and deceleration, respectively. (*d*) and (*c*) Diagrams of the flows for the 1000 ppm solution ($0.71 < El < 1.09$) during acceleration and deceleration, respectively. Note that to convert Re into Wi, the Reynolds number has to be multiplied by El, which is also provided in table 5.1.

irregular and horizontal lines emerge giving rise to the flame pattern [105]. At $Re = 64$ the branches of the flame pattern end up in three horizontal stationary lines, which correspond to three solitary pairs of vortices or diwhirls [89]. The average distance between the centres of the diwhirls is 7.5 times the gap. At $Re = 48$, the diwhirls disappear from bottom to top. A snapshot of a three diwhirls pattern is shown in figure 5.13(*d*). The presence of diwhirls indicates that the 1000 ppm fluid is in the elastic regime.

5.3.2 Hysteresis in the torque

The hysteretic behaviour of the torque exerted by a viscoelastic fluid on the inner cylinder when it is accelerated and then decelerated was first observed by Groisman and Steinberg [92] at a large elastic number. The transitions they observed with $El = 57$ is of purely elastic nature, since $El >> 1$. However, this hysteresis has never been reported for several fluids in a wide range of El, where the viscous and the elastic forces are of the same order. This could help in the understanding of the relationship between the hysteresis and the level of elasticity of the fluid, that is, the elastic number. Here, we analyse the hysteresis observed in the torque for fluids with different concentrations of PEO, that lead to different $0 < El < 1.09$.

The torque data are shown in figures 5.5 and 5.6 as Nu_ω as a function of Re and Wi, respectively. In the laminar regime, Nu_ω is approximately constant and close to one. When Re or Wi is small, Nu_ω is slightly shifted up due to the end effects that introduce an additional torque (see chapter 4). The end effects seem to be reduced for the 1000 ppm solution ($0.71 < El < 1.09$), but it is not clear how the viscoelasticity affects them. At higher Re or Wi, there is a slight increase of the slope of Nu_ω before the abrupt increase of torque corresponding to the onset of inertio-elastic instabilities. This slight increase of torque was also observed in the study by Yi and Kim (1997) and attributed to the polymer contribution. As the shear rate exceeds a critical value, there is a rapid increase of the torque for large values of the polymer concentration. In figure 5.7 it is depicted the critical Reynolds number, Re_c, and the critical Weissenberg number, Wi_c, where the torque increases abruptly, as a function of the elastic number, El. It is observed that as El increases, Re_c decreases, as previously observed [104, 57].

In the case of Wi_c, it increases with the elastic number. In figures 5.5 and 5.6, Nu_ω fluctuates significantly for large value of Re or Wi and El [92].

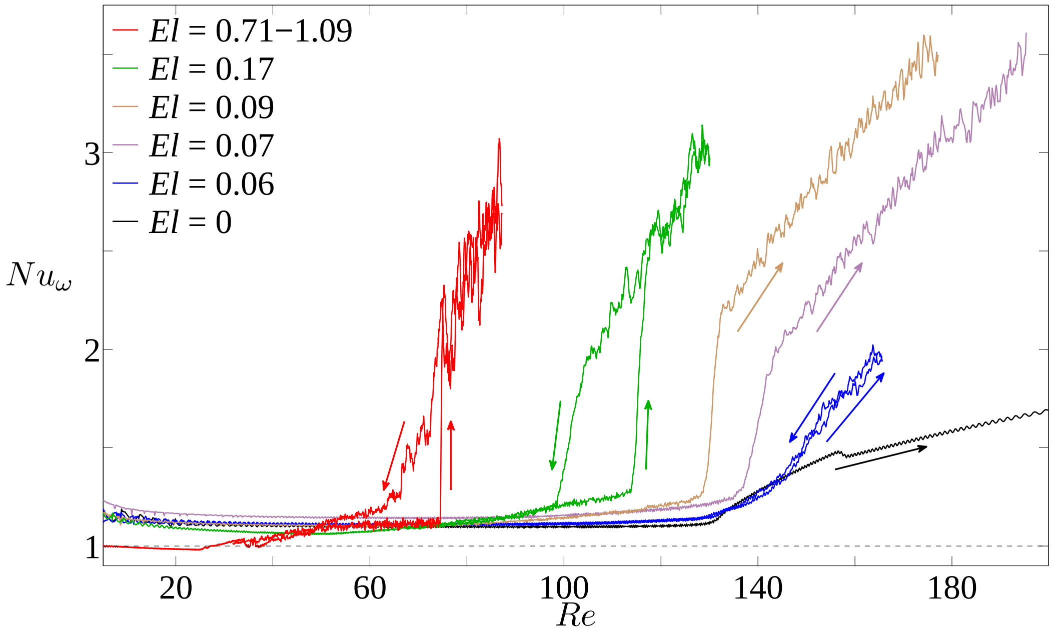

Figure 5.5: Nu_ω as a function of Re for solutions with different El or concentrations of PEO dissolved in 7% PEG aqueous solution. The up- and down-arrows indicate acceleration and deceleration, respectively.

The up- and down-arrows in figure 5.5 indicate the acceleration and deceleration protocol, respectively. The paths followed by Nu_ω present hysteresis loops as observed experimentally before [92]. This hysteretic region is a signature of a subcritical transition between the laminar state ($Nu_\omega \simeq 1$) and the regime where Nu_ω fluctuates. The flow with the smallest polymer concentration exerts almost the same torque when accelerating and decelerating, although the flow patterns can be quite different (see figures 5.3 and 5.4).

When only a single fluid with one concentration is studied, it is clear which dimensionless number best represents the dynamics of the flow. One can decide to use Re when El is small [79, 65], because the viscous forces are dominant, or Wi when El is large [92], since in this case, the elastic forces are the dominant ones. However, when $El \approx 1$ or when several fluids want to be compared in a wide range of elastic numbers,

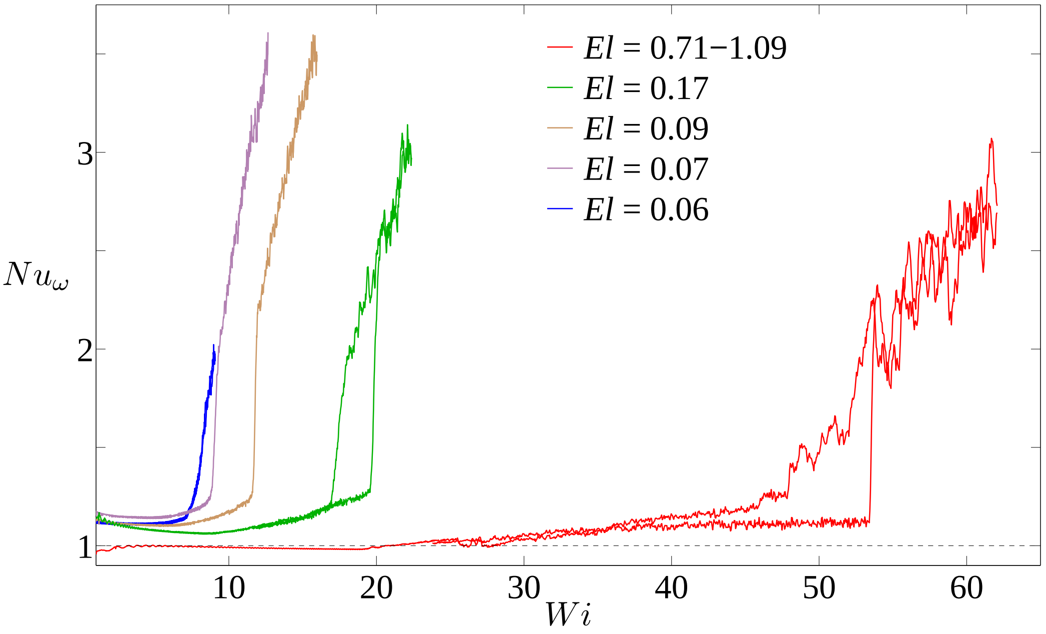

Figure 5.6: Nu_ω as a function of the Wi for solutions with different El or concentrations of PEO dissolved in 7% PEG aqueous solution.

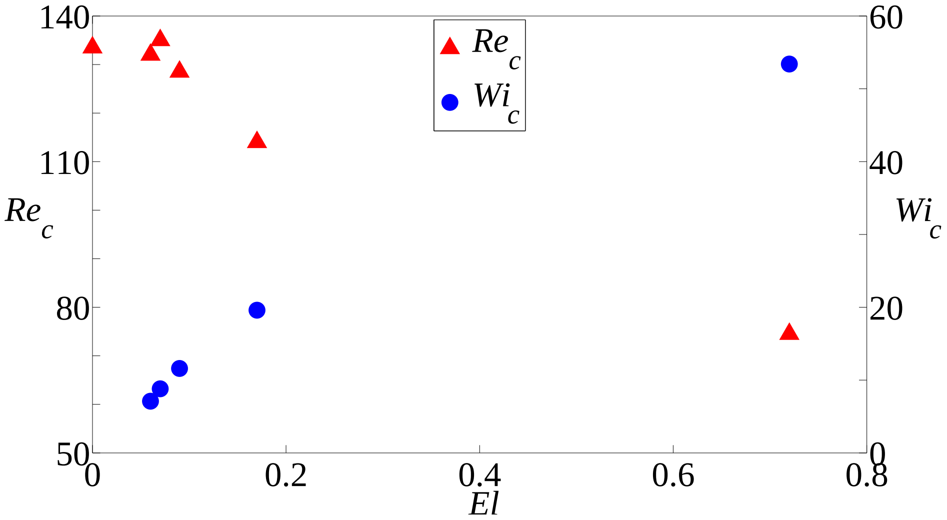

Figure 5.7: Critical Reynolds number, Re_c, and critical Weissenberg number, Wi_c, as a function of the elastic number, El.

an appropriate dimensionless number should be use to combine the effects of viscosity and elasticity, as none of them dominate the flow. Therefore, it is proposed, in a first test, an alternatively way to combine the viscous and the elastic effects, by using the geometric mean time of the viscous and the elastic time scales. In figure 5.8 the evolution of Nu_ω is presented as a function of $\sqrt{ReWi} = \dot{\gamma}\sqrt{\lambda_v \lambda_e}$, where the increase of the threshold with El is evidenced. In figure 5.9 it is depicted the critical control parameter, $\sqrt{ReWi_c}$, as a function of the elastic number, El. The tendency observed is clear and $\sqrt{ReWi_c}$ increases with El.

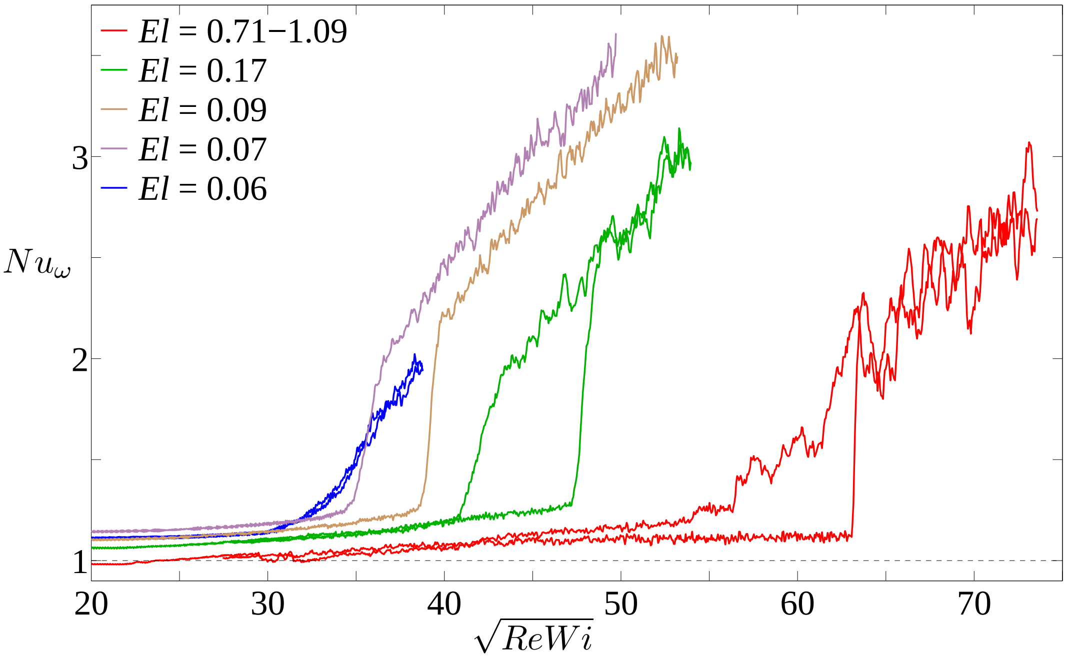

Figure 5.8: Evolution of Nu_ω for solutions with different El or concentrations of PEO dissolved in 7% PEG aqueous solution as a function of $\sqrt{ReWi}$.

The dimensionless areas of the hysteresis loop of the curves $Nu_\omega(Re)$, $Nu_\omega(Wi)$ and $Nu_\omega(\sqrt{ReWi})$, corresponding to figures 5.5, 5.6 and 5.8, respectively, have been calculated. Their values are shown in table 5.2. Since the hysteresis is a phenomenon related to the elasticity of the fluid, its area must be quantified using Wi, as it is the real parameter to count the elasticity effects. Regarding the values in table 5.2, one can observe that the only case when the values increase monotonously occurs for Wi. It means that the areas of the hysteresis loop are directly related to the elasticity of the fluid. On the contrary, the path followed by the Newtonian fluid is reversible presenting no hysteresis, so the transition is supercritical. Such hysteresis loop has also been found in numerical simulations by Thomas *et al.* [96]. Both, in the present experiments and

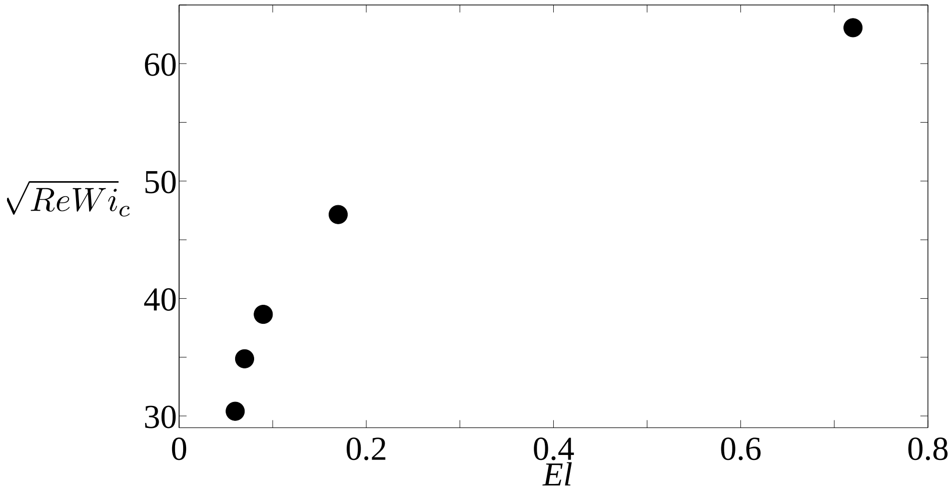

Figure 5.9: Critical $\sqrt{ReWi}_c$ as a function of the elastic number, El.

in the simulations, the flame pattern emerges when decelerating or reducing Wi (see figure 5.4(*d*) for $80 > Re > 64$). The associated torque is shown in figure 5.6 for $53 > Wi > 45$ during deceleration and appears as staircases. In the experiments, an anticlockwise hysteresis loop is observed, where the upper branch corresponds to the flame pattern. This is because of the delay in the elastic response, with respect to the viscous one. Part of the energy stored in the inertio-elastic regime by the elastic stresses is released with some delay during the deceleration, making the level of torque being higher. However, in the simulations [96], the initial state is a pattern of oscillatory strips, which remain stable when increasing Wi, and has larger torque than the flame pattern. Hence, the hysteresis loop predicted from the simulations is in the clockwise direction, contrary to the experiments.

El	0.06	0.17	0.71-1.09
Area loop Re	1.0	12.4	5.3
Area loop Wi	0.05	2.12	3.62
Area loop $\sqrt{ReWi}$	0.23	5.13	4.43

Table 5.2: Areas of the hysteresis loop of the curves $Nu_\omega(Re)$, $Nu_\omega(Wi)$ and $Nu_\omega(\sqrt{ReWi})$ of figures 5.5, 5.6 and 5.8, respectively, as a function of El.

5.3.3 Torque turbulent fluctuations

At high rotation speeds of the inner cylinder, beyond the transition region, the torque fluctuates significantly, as can be observed in figure 5.10. In order to analyse these fluctuations, new series of experiments were performed, where the 1000ppm solution was brought to relatively high shear rates in the inertio-elastic turbulent regime, using the same acceleration rate employed in the previous experiments. The value of the rotation speed at which the fluctuations have been analysed is depicted in figure 5.10 as a blue vertical line. This speed was kept constant at $\dot{\gamma} = 70$ 1/s, $Re = 81$, $Wi = 58$, during 4200s, and the torque was measured with a sampling frequency of 100 Hz, so 42 000 points were acquired.

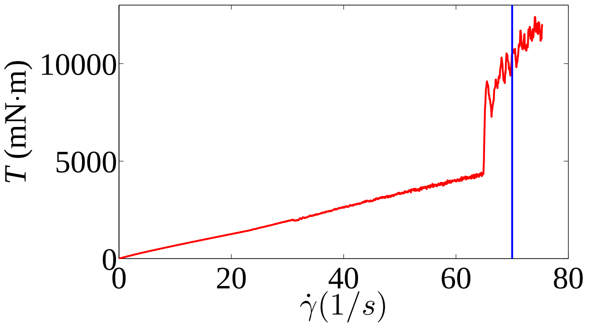

Figure 5.10: Injected power, P, as a function of the shear rate, $\dot{\gamma}$, for the solution containing 1000ppm of PEO dissolved in 7% of PEG. The vertical continuous blue line indicates the value of the shear rate, $\dot{\gamma}$, at which the analysis of the fluctuations has been done.

In figure 5.19(a) the evolution of the injected power signal, $P(t) = T(t) \times \Omega$, as a function of time, t, is shown. The power decreases during the experiment around 47% of its initial value. In order to be able to analyse the fluctuations, a deconvolution has been applied to the power signal. If the signal is the multiplication of an exponential function, $E(t)$, and a function containing the fluctuation, $F(t)$, as $P(t) = E(t) \times F(t)$, the resulting signal is as, $P_c(t) = P(t)/E(t) \times \bar{P}$. It is depicted in figure 5.19(b). It can be observed the presence of multiple frequencies, a typical behaviour of a random signal.

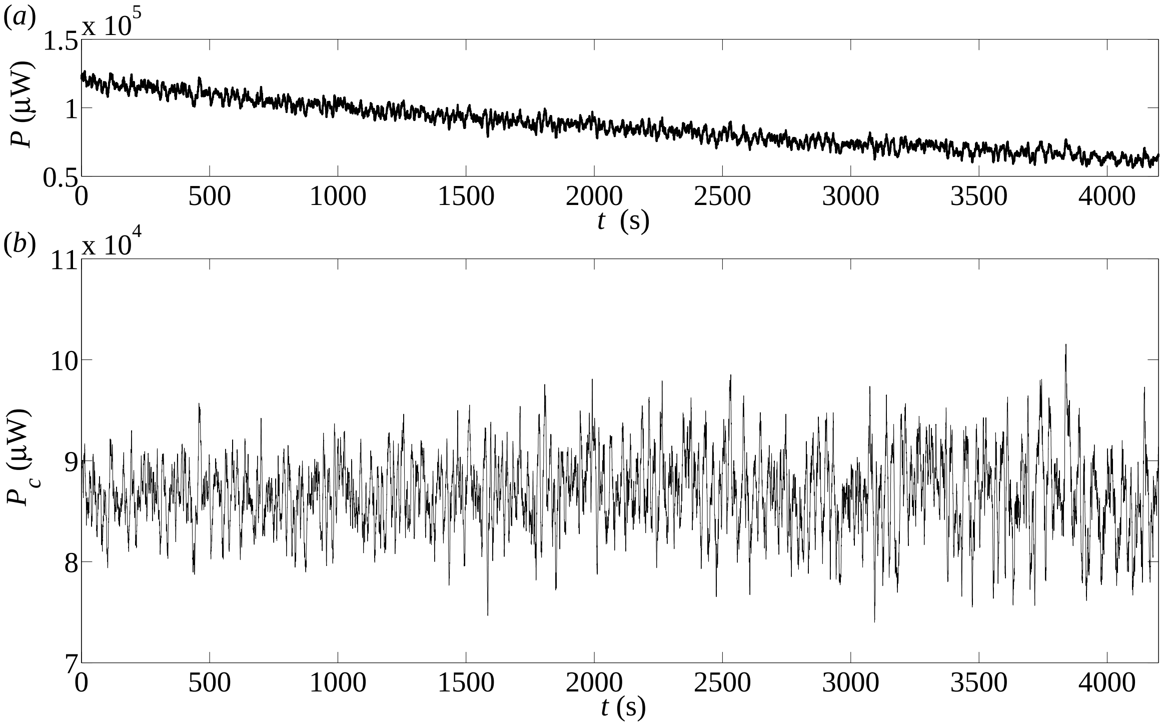

Figure 5.11: (a) Evolution of power, P, as a function of time, t for the solution containing 1000ppm of PEO dissolved in 7% of PEG when the rotation speed is kept constant at $\dot{\gamma} = 70$ 1/s. (b) Deconvolution of the power signal, P_c.

Figure 5.12(a) presents the normalized probability distribution functions (PDF) of the reduced injected power, $(P(t)-\langle P\rangle)/\sigma_p(P)$, where $\langle P\rangle$ is its time average and $\sigma_p(P)$ is the standard deviation of the signal $P(t)$. The PDF lays on the Gaussian curve for values above 3×10^{-2}, indicating the absence of intermittence in the torque signal. Figure 5.12(b) presents the spectral power density (SPD) of the injected power, $P(t)$. Two regions with different slopes can be identified. For frequencies below $f < 5 \times 10^{-3}$ the slope equals -1.5 and for $f > 5 \times 10^{-3}$ the slope equals -2.3. It means that the energy transfer at the higher frequencies is faster than for the low frequencies. For polymer solution in Couette-Taylor flow, radial velocity measurements [92] show a slope of -1.1 at low frequencies and a slope of -2.2 at higher frequencies. Simulations for radial velocity signal at a particular position in the gap are available [97] finding exponents from 0.6 to 2.2.

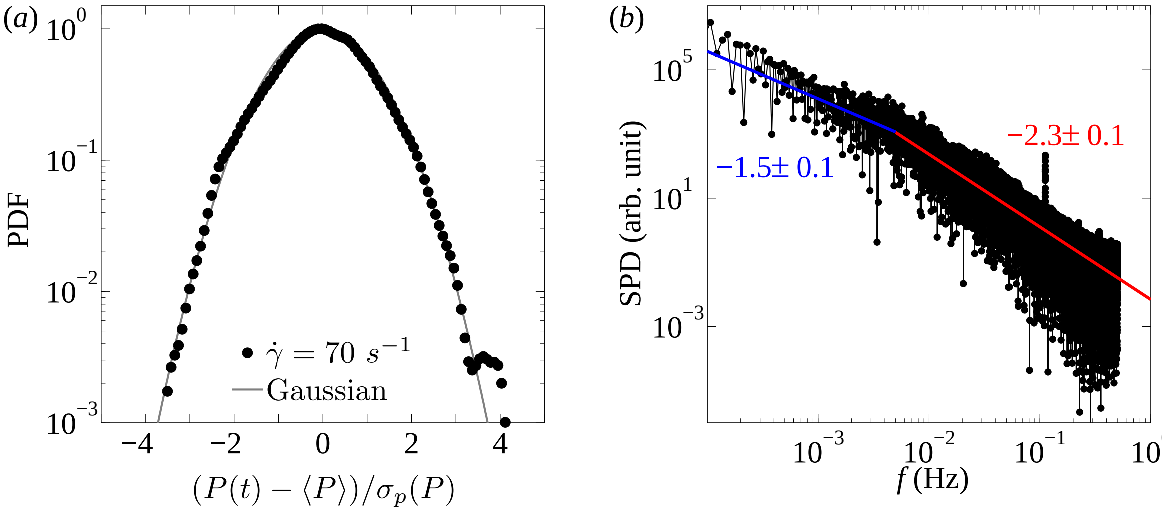

Figure 5.12: (a) Normalized PDFs of the reduce value of the injected power, $(P(t) - \langle P \rangle)/\sigma_p(P)$, of a solution containing 1000 ppm of PEO dissolved in 7% PEG aqueous solution at steady-state regime for shear rates, $\dot{\gamma} = 70$. The continuous line is a fitting to the Gaussian function. (b) SPD of the injected power.

5.3.4 Diwhirls

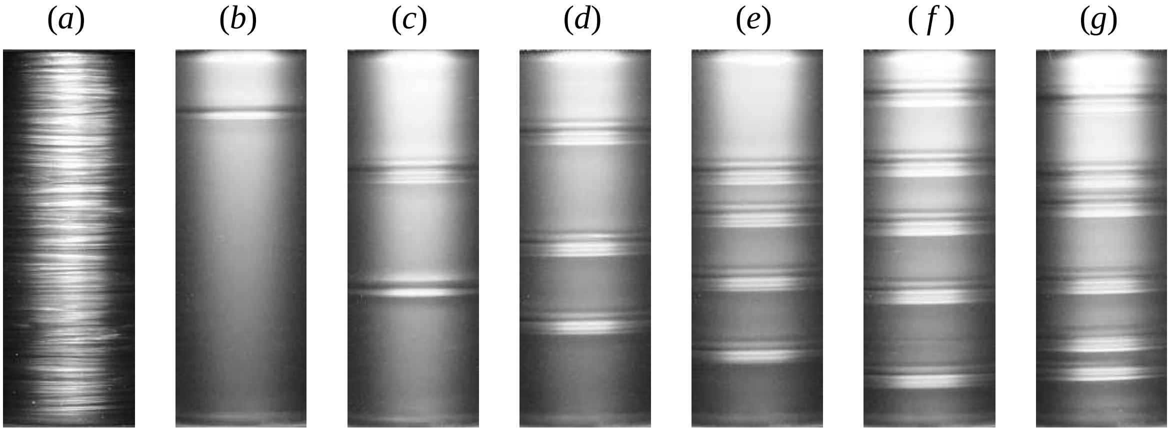

Figure 5.13: Snapshots over the whole height of the flow of solutions containing 1000 ppm of PEO dissolved in 7% PEG aqueous solution . (a) Inertio-elastically turbulent flow. (b-g) Flows at $Wi = 37$ containing 1 to 6 diwhirls, from left to right, respectively.

During deceleration, coming back from the inertio-elastic turbulent regime for solutions of high El, the latest stages of the hysteretic region gives rise to diwhirls [89]. These steady vortices have been found in the form of 1 to 6 pairs and are depicted in figure 5.13(*b*-*g*). The diwhirls are stationary counter-rotating vortices localised in space with strong inflow. The diwhirl pairs are separated by large laminar zones, that extend not regularly. They are due to the elastic stresses which tend to relax in the flow. The number of diwhirls increases with the ramping rate. The faster is the deceleration, the shorter is the time that the elastic stresses have to relax, so they have less time to respond to the applied stress. In practice, the numbers of diwhirls is controlled by the deceleration rate of the inner cylinder as quantified in figure 5.14(*a*). Using the constant deceleration of $\Delta\Omega/\Delta t = 0.1 \times \Delta\dot{\gamma}/\Delta t = -5.2 \times 10^{-3}$ rad/s^2, three diwhirls are observed (see figure 5.4(*d*) and figure 5.13(*e*). When using faster decelerations, the number of diwhirls increases. An alternative procedure to obtain 1 or 2 diwhirls is to decrease the speed of the inner cylinder until the diwhirls start to disappear. Once the desired number of diwhirls is reached, the inner cylinder is accelerated to a speed that can sustain it. Furthermore, the existence of diwhirls leads to an additional torque with respect to the laminar torque. It has been measured at a constant speed, $Re = 51$ or $Wi = 37$, for several minutes and is represented in figure 5.14(*b*) as the additional torque compared to the laminar, $\bar{T} - T_{lam}$, per number of diwhirls, n_d, divided by the laminar torque. Here, the laminar torque, T_{lam}, is the torque of the flow without any diwhirl. The increase of this relationship with n_d indicates that the additional torque that each individual diwhirls needs to be sustained depends on the numbers of diwhirls. This could be also explained relating this increase of torque to the distance between diwhirls, so the closer they are the more torque they need. The variation of the torque with the number of diwhirls is given by the following fit,

$$(\bar{T}/T_{lam} - 1)/n_d = \mathcal{B} + \mathcal{C}(n_d - 1)^{\zeta}, \tag{5.7}$$

where $\mathcal{B}$ represents the momentum transfer per diwhirl in a flow containing one diwhirl. Note that this is directly related to the energy dissipation rate of this solitary diwhilr (see (2.52)), as it is equal to $\bar{T}/T_{lam} - 1$. The coefficient $\mathcal{C}$ measures the influence of the number of diwhirls on the additional torque over the laminar. The exponent ζ indicates how strong is the dependency of the torque on the numbers of diwhirls. Here $\zeta \simeq 3/5$, $\mathcal{B} = 1.37 \times 10^{-3}$ and $\mathcal{C} = 8.4 \times 10^{-3}$.

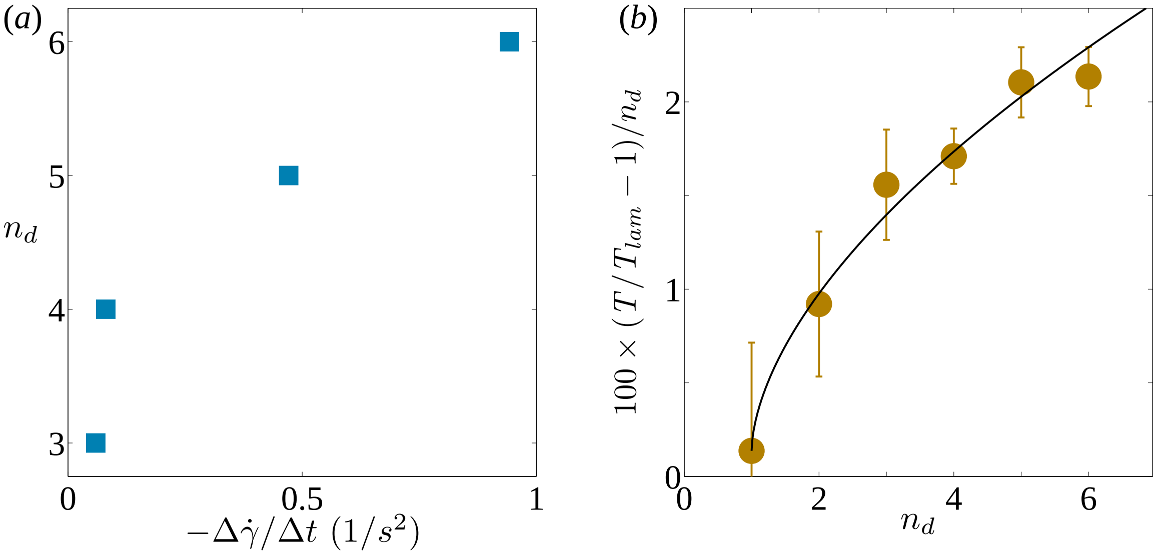

Figure 5.14: (a) Dependency of the numbers of diwhirls, n_d, on the deceleration of the inner cylinder, $-\Delta\dot{\gamma}/\Delta t$. ($b$) Additional dimensionless torque over the laminar per number of diwhirls, n_d, of flows containing six different numbers of diwhirls at $Re = 51$ or $Wi = 37$. The black line represents a fitting described in the text (5.7).

5.4 Non pre-sheared solutions

As observed in figure 5.1, the transition point strongly depends on the pre-shear when the concentration of polymer increases. So, it is interesting to analyse it in terms of dimensionless numbers. In this section the results concerning the non pre-sheared fluids are studied and compared with those of pre-shear fluids.

5.4.1 Torque increase

The variation of the torque with the rotation speed of the inner cylinder is analysed. In figures 5.15 and 5.16 the evolutions of the Nu_ω as a function of Re and Wi are presented, respectively, for all the solution without pre-shear. Note that they correspond to the dimensional curves shown in figure 5.2. As previously observed, the critical Reynolds number, Re_c, where the torque increases abruptly, decreases for increasing El, and the critical Weissenberg number, Wi_c, increases for increasing El. In figure 5.17 it is depicted the critical Reynolds number, Re_c, and the critical Weissenberg number, Wi_c, where the torque increases abruptly, as a function of the elastic number, El. If it is compared with figure 5.7, it is observed that both Re_c and Wi_c are much smaller for the solutions with $El = 0.17$ and 0.72. This can be also deduced from figure 5.1. In figures 5.15 and 5.16, the $Nu_\omega(Re)$ and $Nu_\omega(Wi)$ curves reach a maximum that increases with El. In the case of $Nu_\omega(Re)$, the maximum is attained with different slopes, that increase with El. After this maximum, the curves for $El = 0.06$ and 0.07 present a plateau, what indicates that the torque increases linearly with the rotation speed of the inner cylinder, so the increase of energy dissipation rate is constant. The curves with higher El decreases after the maximum. This is due to the degradation of the solution shown in figure 5.2. In the case of $0.66 < El < 1.09$ the solution is completely degraded at $Re = 500$. Then, the Nu_ω is constant, as for $El = 0.06$ and 0.07. Again, the steps correspond to the change in the number of vortices. The absence of fluctuations indicates that there is no more elastic effects.

In figure 5.18 it is depicted the evolution of Nu_ω as a function of $\sqrt{ReWi}$. In this case, the critical $\sqrt{ReWi}$ where the torque increase abruptly does not follow a monotonous behaviour as for the pre-sheared solutions, as shown in figure 5.8.

5.4.2 Torque turbulent fluctuations

The torque fluctuations observed in figures 5.15 and 5.16) have been quantify, so experiments were performed where the 1000 ppm solution was brought to relatively high shear rates in the inertio-elastic turbulent regime, without being pre-sheared, and then, the shear rate was kept constant during 3000 s. The torque was measured with a sampling frequency of 1 Hz. The fluctuations for the applied shear rates $\dot{\gamma} = 46$ and 85 s^{-1} are 3.1 and 3.2%, respectively. In figures **??** and 5.20 the power signals are shown as previously done in figure 5.19. Figure 5.21(a) presents the normalized probability

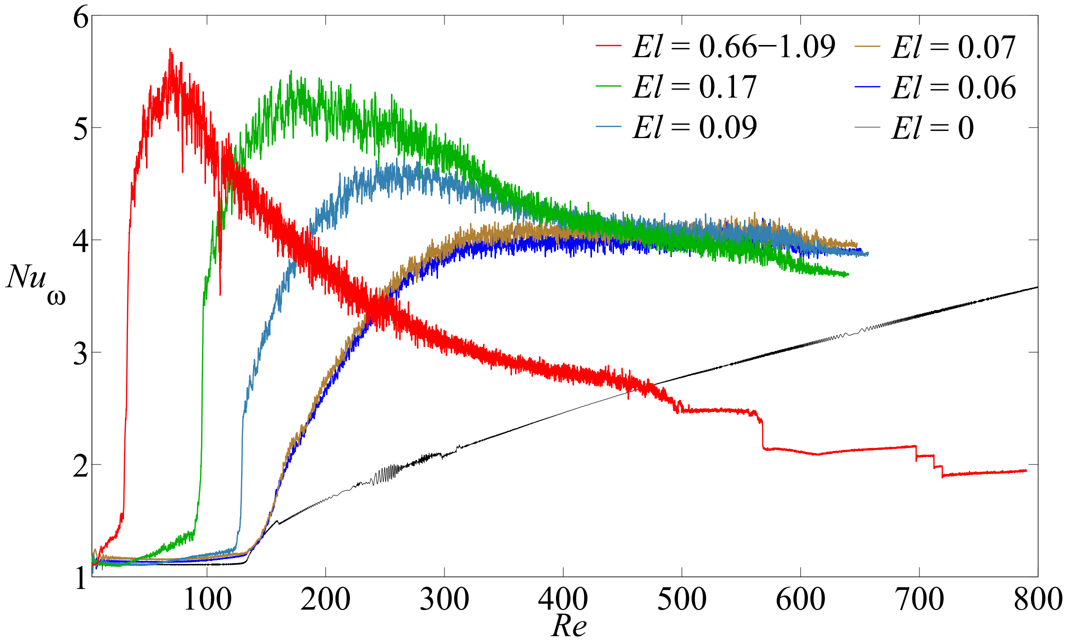

Figure 5.15: Nu_ω as a function of Re for solutions with different El or concentrations of PEO dissolved in 7% PEG aqueous solution for non pre-sheared solutions.

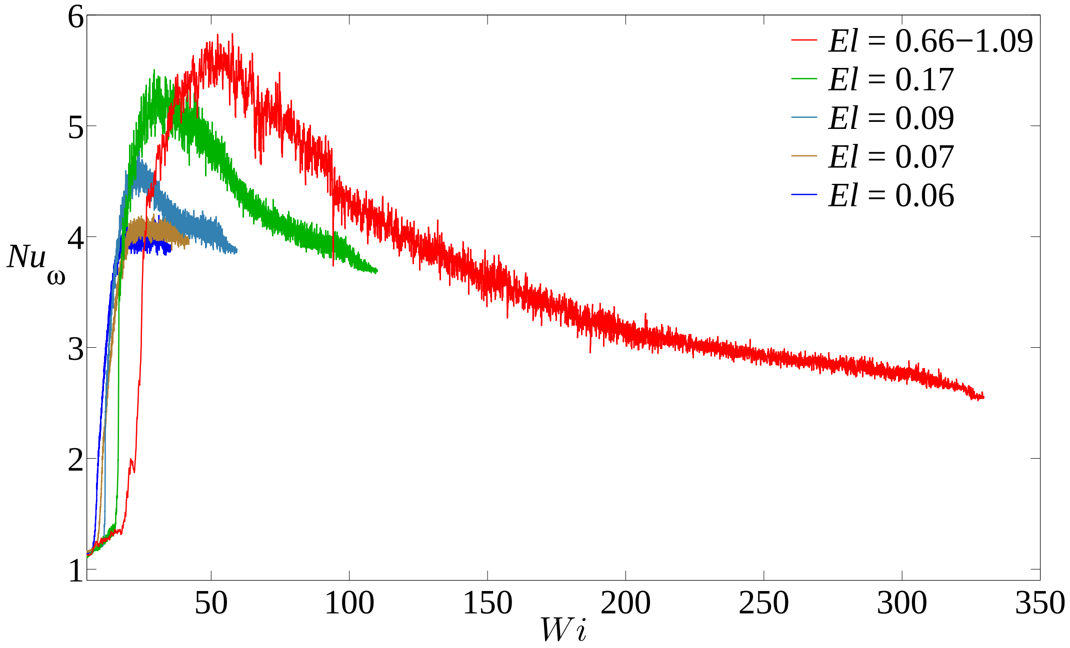

Figure 5.16: Nu_ω as a function of Wi for solutions with different El or concentrations of PEO dissolved in 7% PEG aqueous solution for non pre-sheared solutions.

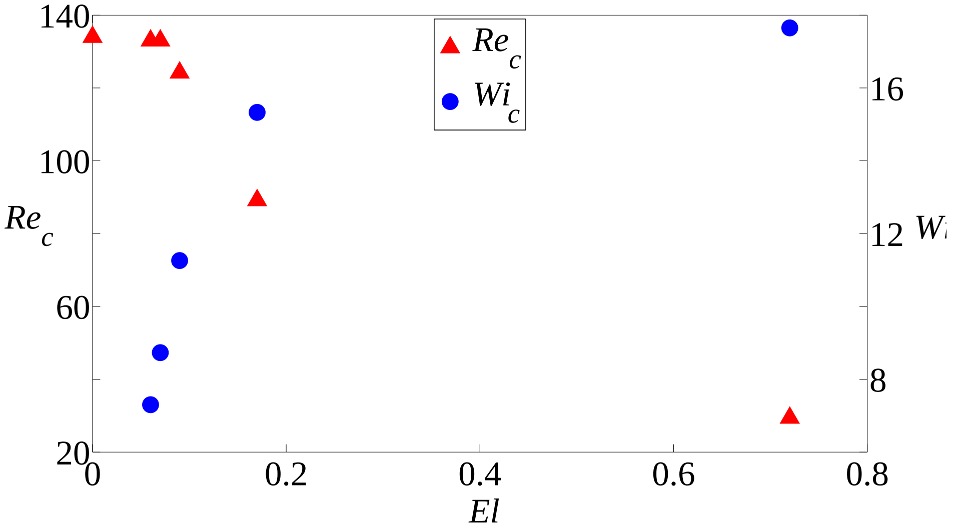

Figure 5.17: Critical Reynolds number, Re_c, and critical Weissenberg number, Wi_c, as a function of the elastic number, El, for non pre-sheared solutions.

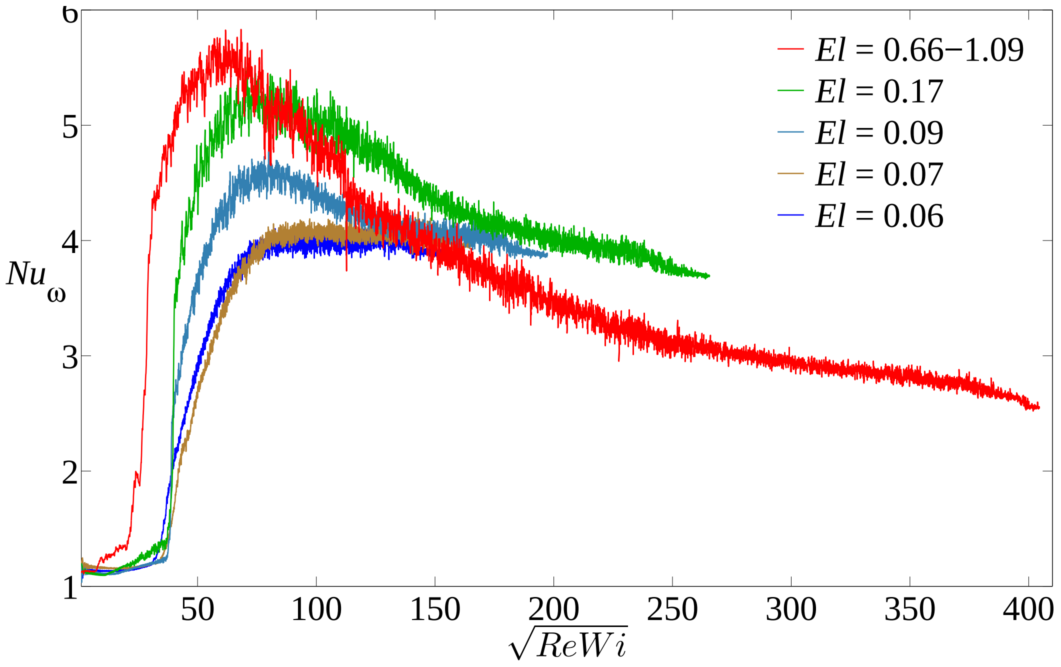

Figure 5.18: Evolution of Nu_ω for non-presheared solutions with different El or concentrations of PEO dissolved in 7% PEG aqueous solution as a function of $\sqrt{ReWi}$.

distribution functions (PDF) of the reduced injected power, $(P(t) - \langle P \rangle)/\sigma_p(P)$, where $P(t) = T(t) \times \Omega$ is the injected power, $\langle P \rangle$ is its time average and $\sigma_p(P)$ is the standard deviation of the signal $P(t)$. It can be seen that the two PDFs lay on the same master curve for PDF values above 3×10^{-2}. The continuous line is a Gaussian fit to show the non-Gaussian nature of the PDFs. Figure 5.21(b) presents the spectral power density (SPD) of the injected power, $P(t)$. Both PSDs vary with a power law and an exponent of -1.9±0.2.

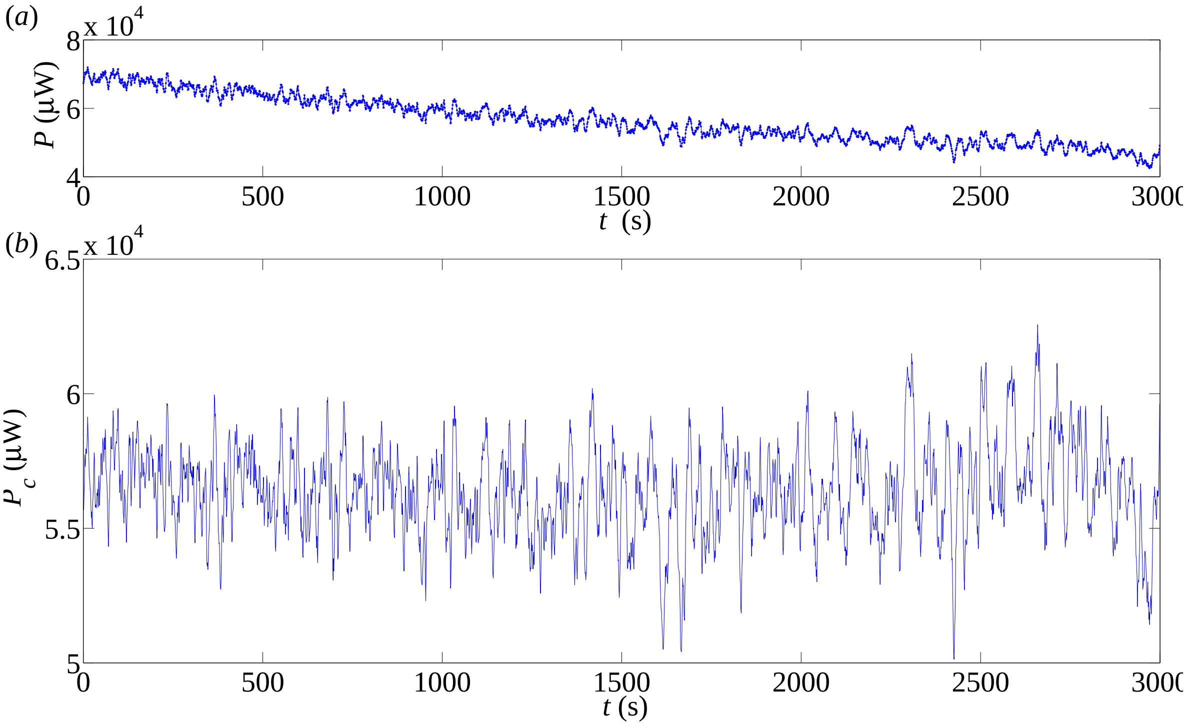

Figure 5.19: (a) Evolution of power, P, as a function of time, t for the solution containing 1000ppm of PEO dissolved in 7% of PEG without pre-shear when the rotation speed is kept constant at $\dot{\gamma} = 46$ 1/s. (b) Deconvolution of the power signal, P_c.

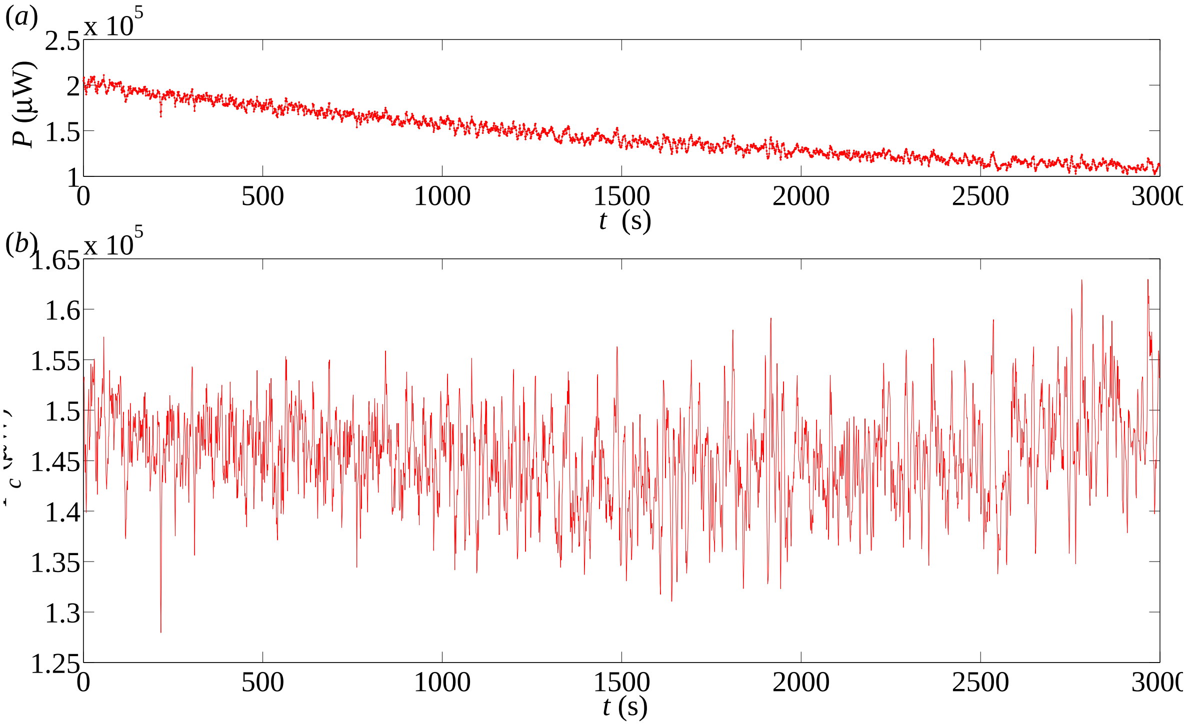

Figure 5.20: (a) Evolution of power, P, as a function of time, t for the solution containing 1000ppm of PEO dissolved in 7% of PEG without pre-shear when the rotation speed is kept constant at $\dot{\gamma} = 85$ 1/s. (b) Deconvolution of the power signal, P_c.

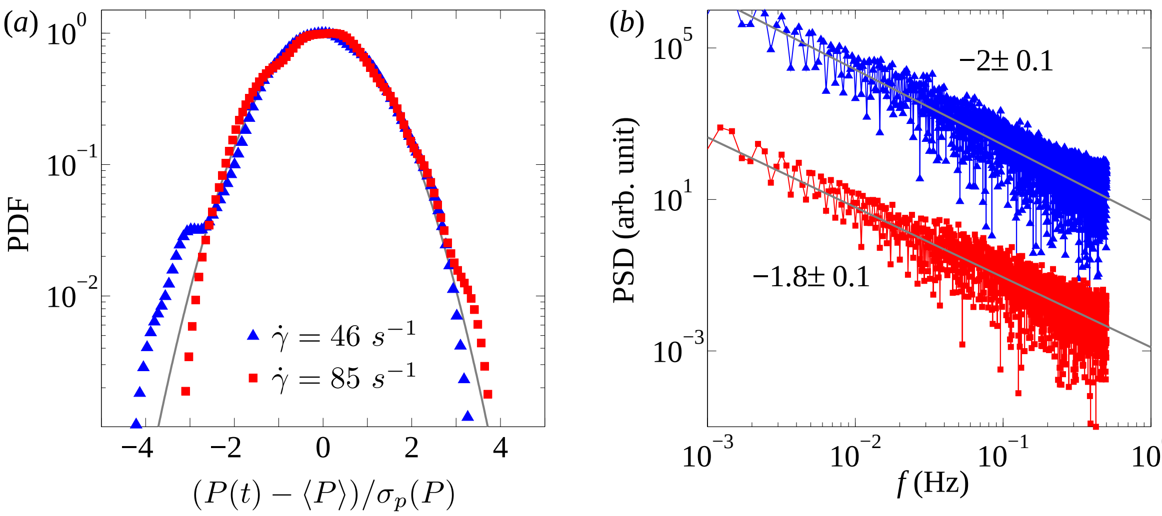

Figure 5.21: (a) Normalized PDFs of the reduce value of the injected power, $(P(t) - \langle P \rangle)/\sigma_p(P)$, of a solution containing 1000 ppm of PEO dissolved in 7% PEG aqueous solution at steady-state regime for shear rates, $\dot{\gamma} = 46$ and 85 s^{-1} ($Re = 55$ and 100, $Wi = 38$ and 70). The continuous line is a fitting to the Gaussian function. (b) PSDs of the injected power. For clarity, the curve for $\dot{\gamma} = 85$ s^{-1} has been shifted down by a factor 10^{-4}.

5.5 Conclusions

The effect of viscoelasticity over a wide range of elastic numbers, El, on Couette-Taylor flow has been investigated. Using a specific protocol, consisting on a slow acceleration and deceleration of the inner cylinder, the flow patterns and the corresponding torque have been analysed. A significant difference is found when the solutions are pre-sheared after preparation. The degradation of the fluid is analysed, finding that the fluid degrades mechanically, if high shear rates are applied. Above a certain value of shear rate, $\dot{\gamma}$, the solution loses all its elasticity and behaves as a Newtonian fluid, presenting the same flow patterns.

The flow patterns of pre-sheared solutions vary with El. Taylor vortices are found during acceleration for $El < 0.1$, and its range of stability decreases with El. The disordered oscillating flow is also found during acceleration for $El < 0.1$ and its range of stability also decreases with increasing El. Standing waves are found during deceleration, in the case of $El = 0.05$ (or $\mathrm{C_{PEO}}$=76 ppm) and during acceleration and deceleration for $El = 0.17$ (or $\mathrm{C_{PEO}}$=300 ppm). All the fluids present the pattern typical of inertio-elastic turbulence at high Reynolds numbers, Re. In the case of $El \approx 1$ (or $\mathrm{C_{PEO}}$=1000 ppm) and during deceleration, the inertio-elastic turbulent pattern gives rise to the flame pattern, that end in three pairs of vortices, also called diwhirls. These transitions, that were reported before [105, 92, 65], are retrieved and the associated torque has been measured in more details.

The torque during an acceleration-deceleration cycle of the inner cylinder presents a hysteresis loop, indicating a subcritical transition. During the acceleration, the torque increases abruptly at a critical point. The critical Reynolds number, Re_c, decreases with El. The critical Weissenber number Wi, increases with El. The critical points for the pre-sheared fluids are much larger when $El \geq 0.17$. The area of the loops increases with the elasticity of the solutions, since they are associated to the elastic stresses. The torque presents large fluctuations at high rotation speed of the inner cylinder, associated to intertio-elastic turbulence, its amplitude increases with El. At large rotation rates, the torque signal fluctuates significantly and its power spectral density scales with the frequency with an exponent of -1.9 ± 0.2, indicating that it is a inertio-elastic turbulent flow.

Six different numbers of stationary solitary pair of vortices or diwhilrs have been found when varying the deceleration rate of the inner cylinder. The faster is the deceleration, the larger is the number of diwhirls. This is associated to the response time of the elastic stresses. The torque that these diwhilrs exert per number of diwhirl increases with the number of diwhirls present in the flow.

Chapter 6

Conclusions

"Let the future tell the truth and evaluate each one according to his work and accomplishments. The present is theirs; the future, for which I have really worked, is mine".

—Nicola Tesla

The experimental researches carried out in the LOMC deal with the fluid confined between two coaxial differentially rotating cylinders, namely, the Couette-Taylor flow, particularly, when only the inner cylinder rotates and the outer is fixed. This system is characterised by the radius ratio, η, which is the ratio between the inner and the outer radii of the cylinders and the aspect ratio, Γ, which is the ratio between the height of the cylinders and the gap between them. The investigations have focused on turbulent flows, those which appear at high Reynolds numbers, Re, *i.e.*, when the inertial forces dominate the viscous forces. Turbulent flows are characterised by a high energy dissipation and a high momentum transfer. This kind of flow are of great scientific and technological interest, since they appear in several natural and industrial processes.

In the last decade there has been a large interest in turbulent Couette-Taylor flows among the scientific community, after Eckhardt, Grossmann and Lohse [44] proposed an unifying theory that makes the analogy with Rayleigh-Bénard convection, the flow between two parallel differentially heated plates. They demonstrated that the equations that describe the evolution of the momentum transfer in Couette-Taylor flow are analogous to the equations of Rayleigh-Bénard convection. In Couette-Taylor flow, the momentum transfer is characterised by the pseudo-Nusselt number, Nu_ω, and by the centrifugal driving force, represented by the Taylor number, Ta, which is proportional to Re^2. In Rayleigh-Bénard convection, the heat transfer is described by the Nusselt number, Nu, and by the driving force (the Archimede buoyancy force), represented by the Rayleigh number, Ra, which is proportional to the temperature difference between the plates. Both systems have similar scaling of the momentum and heat transfer with their corresponding driving force in the turbulent regime. This scaling laws have exponents which should be the exactly the same. The power law relationship in Couette-Taylor flow between is written as $Nu_\omega \propto Ta^{\xi_{TC}}$, and the power law relationship in Rayleigh-Bénard convection is written as $Nu \propto Ra^{\xi_{RB}}$, so it is expected that $\xi_{TC} \approx \xi_{RB}$. This theory also allows to calculate the energy dissipation rates by exactly the same equations. In the case of Couette-Taylor flow the dimensionless energy dissipation rate is given by $\hat{\varepsilon}_{TC} = Ta/\sigma^2(Nu_\omega - 1)$ and in Rayleigh-Bénard convection is given by $\hat{\varepsilon}_{RB} = Ra/Pr^2(Nu - 1)$. The pseudo-Prandtl number, σ, in Couette-Taylor flow is the analogous of the Prandtl number, Pr, in Rayleigh-Bénard convection. The momentum transfer and the energy dissipation rate can be easily quantified by measuring the torque exerted by the flow in the inner cylinder.

The main goal of this thesis has been to analyse several parameters that influence the momentum transfer and energy dissipation by acquiring accurate torque measurements. We got interested in the effect of the variation of the number of vortices present in a turbulent flow and the influence of the radius ratio, η, in the momentum transfer, Nu_ω. Three systems with different η have been studied. The torque measurements reveal that flows with different numbers of vortices exert distinct levels of torque, giving rise to distinct $Nu_\omega(Re)$ curves. Consequently, the momentum transfer and energy dissipation rate change from one state to another. Crossings of the $Nu_\omega(Re)$ curves are observed, a feature related to the transition to the so-called "ultimate regime of turbulence", a regime attained when the boundary layers become turbulent, in analogy with the Rayleigh-Bénard convection. Before the crossings, flows with larger number of vortices exert higher levels of torque. After the crossings, flows with larger number of vortices exert lower levels of torque. This is related to the change of momentum transfer mechanism in the ultimate regime of turbulence, in which the turbulent boundary layers predominates over the vortices. The variation of the exponent $\xi = (\alpha - 1)/2$ with the driving force $Ta \propto Re^2$ has been studied. The scaling laws of the torque shows that flows with smaller number of vortices have larger exponents, α. This indicates that the level of turbulence increases when decreasing the number of vortices. It is found that the pre-factor, $\mathcal{A}$, becomes constant in the ultimate regime, another indication of the change of momentum transfer mechanism in this regime. Finally, we have observed that the radius ratio, η, and the aspect ratio, Γ, modify the threshold of the transition to the ultimate regime of turbulence.

The other goal of this thesis has been to analyse the effect of viscoelasticity in the energy dissipation of Couette-Taylor flow with aqueous solutions of poly(ethylene oxyde) (PEO). Viscoelastic solutions have been studied in a wide range of elastic numbers, El, which is the ratio between Re and the Weissenberg number, Wi. Using a protocol consisting on a acceleration and deceleration of the inner cylinder, the flow patterns and the corresponding torque have been analysed. Distinct patterns have been observed in solutions with different concentrations of PEO. A variation of the critical Reynolds number, Re_c, and the critical Weissenber number, Wi_c, is found, corresponding to an abrupt increase of the torque, at different El. Hysteresis loops in the $Nu_\omega(Re)$ and $Nu_\omega(Wi)$ curves have been observed for increasing with El. When using solutions whose El is close to one, different number of stationary solitary pair of vortices, called diwhirls, have been found when decelerating the inner cylinder, starting from the inertio-elastic turbulent regime. Their energy dissipation rate have been quantified. The analysis of the torque signal fluctuations at high shear rates, $\dot{\gamma}$, indicates the presence of intertio-elastic turbulence in the flow.

This project has allowed me to acquire a wide knowledge about torque measurements in several Couette-Taylor systems. The torque have been measured in three different systems with distinct radius ratios using a rheometer. Additionally, the collaboration with the Department of Aerodynamics and Fluid Mechanics in the Technical University of Cottbus-Senftenber, in Germany, has allowed me to operate a different type of Couette-Taylor system, which uses strain gauges as a torque measurement system. Flow visualisations have also been performed using different types of laboratory instruments (high speed cameras, white lights, lasers). The image treatment and the creation of spatio-temporal diagrams have been done using specific programs or codes that have been developed in the laboratory. The rheological properties of the fluids have been analysed. Several measuring apparatuses, such us a density-meter, viscosimeters, a tensiometer, a shear rheometer, or a Capillary Breakup Extensional Rheometer (CaBER), have been employed to quantify the density, the viscosity, the relaxation time or the surface tension of the tested fluids. In the case of the shear rheometer, various configurations have been employed, like cone and plate geometries with different angles or cup and bob geometries. In the case of the extensional rheometry, I have learnt how to master this robust measurement technique to obtain the relaxation times to characterise the viscoelastic fluids.

Finally, the collaboration between the laboratory in Le Havre and the one in Cottbus has resulted in a three-month research project founded by the European High performance Infrastructures in Turbulence (EuHIT) program. This European project has allowed me to broaden further my research experience in a different institute and in a different country. The experience has been fruitful, thanks to the possibility of the exchange of ideas and work methods.

Résumé

Les travaux de recherche menés au cours de la thèse au LOMC concernent l'écoulement de Couette-Taylor dans l'entrefer de deux cylindres coaxiaux lorsque le cylindre intérieur tourne et l'extérieur est fixé. Ce système est caractérisé par le rapport des rayons ,η, du cylindre intérieur et du cylindre extérieur, et le rapport d'aspect, Γ, entre la hauteur des cylindres et la taille de l'entrefer. Les recherches se sont centrées sur les écoulements turbulents, qui apparaissent à des grandes valeurs du nombre de Reynolds, Re, c'est-à-dire, quand les forces inertielles dominent les forces visqueuses. Les écoulements turbulents sont caractérisés par une forte dissipation d'énergie et un grand transfert de quantité de mouvement. Les écoulements turbulents revêtent un grand intérêt scientifique et technologique car ils apparaissent dans beaucoup de phénomènes naturels et de processus industriels.

Durant la dernière décennie, les écoulements turbulents de Couette-Taylor ont attiré une forte attention de la communauté scientifique grâce à la théorie unificatrice proposée par Eckhardt, Grossman et Lohse, qui fait l'analogie avec la convection de Rayleigh-Bénard entre deux plaques horizontales parallèles maintenues à différentes températures. Ils ont montré que les équations qui décrivent l'évolution du transfert de la quantité de mouvement entre les deux cylindres dans l'écoulement de Couette-Taylor sont analogues à celles qui décrivent le transfert de chaleur entre les deux plaques dans la convection de Rayleigh-Bénard. Dans l'écoulement de Couette-Taylor, le transfert de quantité de mouvement est caractérisé par le pseudo-nombre de Nusselt, dénoté Nu_ω, et par la force motrice centrifuge, représentée par le nombre de Taylor, Ta, proportionnel au carré de la vitesse de rotation du cylindre et la courbure. Dans la convection de Rayleigh-Bénard, le transfert de chaleur est décrit par le nombre de Nusselt, Nu, et par la force motrice (poussée d'Archimède), qui est représentée par le nombre de Rayleigh, Ra proportionnel à la différence de température entre les plaques. Les deux systèmes ont des lois d'échelle similaires du transfert de quantité de mouvement et de

chaleur, par rapport à leurs forces motrices. Ces lois s'expriment sous forme de lois de puissance avec des exposants qui devraient être identiques. La loi de puissance dans l'écoulement de Couette-Taylor s'écrit comme $Nu_\omega \propto Ta^{\xi_{TC}}$, et la loi de puissance dans la convection de Rayleigh-Bénard s'écrit comme $Nu \propto Ra^{\xi_{RB}}$ et on s'attend à ce que $\xi_{TC} \approx \xi_{RB}$. Cette théorie permet aussi de décrire le taux de dissipation d'énergie avec exactement les mêmes équations. Le taux de dissipation d'énergie adimensionnel est donné par $\hat{\varepsilon}_{TC} = Ta/\sigma^2(Nu_\omega - 1)$ dans l'écoulement de Couette-Taylor et par $\hat{\varepsilon}_{R-B} = Ra/Pr^2(Nu - 1)$ dans la convection de Rayleigh-Bénard. Le pseudo-nombre de Prandtl, σ, dans l'écoulement de Couette-Taylor est analogue au nombre de Prandtl, Pr, dans la convection de Rayleigh-Bénard. Le transfert de quantité de mouvement et le taux de dissipation d'énergie dans le système de Couette-Taylor peuvent être facilement quantifiés, par la mesure du couple que l'écoulement applique sur le cylindre intérieur.

L'objectif principal de la thèse a été l'étude exprimentale de l'influence de certains paramètres sur le transfert de la quantité de mouvement et sur la dissipation d'énergie. Cette étude a été réalisée par l'acquisition de mesures précises du couple. Nous nous sommes intéressés à l'influence de la variation du nombre de rouleaux et du rapport des rayons, η, sur le transfert de quantité de mouvement, Nu_ω. Trois systèmes avec différentes valeurs de η ont été étudiés. Les mesures du couple ont révélé que les écoulements avec différents nombres de tourbillons exercent un niveau de couple différent et donc donnent lieu à des courbes distinctes $Nu_\omega(Re)$. Par conséquent, le transfert de quantité de mouvement et le taux de dissipation d'énergie changent d'un état à un autre. Des croisements des courbes $Nu_\omega(Re)$ sont observés, une caractéristique liée à la transition vers le "régime ultime de la turbulence", un régime atteint quand les couches limites deviennent turbulentes, par analogie à la convection de Rayleigh-Bénard. Avant chaque croisement, les écoulements avec un nombre plus grand de rouleaux exercent un couple plus grand que ceux avec un petit nombre de rouleaux. Après chaque croisement, la situation s'inverse. Ceci est relié au changement du mécanisme du transfert de quantité de mouvement dans le régime ultime de la turbulence, où la turbulence dans les couches limites domine sur la dynamique des tourbillons. La variation de l'exposant $\xi = (\alpha - 1)/2$ avec la métrique Ta de la force motrice a été analysée. La loi d'échelle du couple montre que les écoulements avec un nombre de rouleaux plus petit ont un exposant α plus grand. Cela signifie que le niveau de turbulence augmente quand le nombre de tourbillons diminue. Le pré-facteur, $\mathcal{A}$ de la loi de puissance, devient constant dans le régime ultime de la turbulence, une autre signature du changement du mécanisme du transfert de la quantité de mouvement dans ce régime. Nous avons observé aussi que le rapport des rayons, η, et le rapport d'aspect, Γ, modifient le seuil de la transition vers le régime ultime de la turbulence.

L'autre objectif de cette thèse a été d'étudier l'effet de la viscoélasticité des solutions aqueuses de polyoxyéthylène (PEO) sur la dissipation d'énergie des écoulements de Couette-Taylor. On a étudié des solutions viscoélastiques ave une grande plage de nombres élastiques, El, rapport entre Re et le nombre de Weissenberg, Wi. En utilisant un protocole d'accélération et de décélération de la vitesse de rotation du cylindre intérieur, les motifs qui apparaissent dans l'écoulement et le couple associé ont été analysés. Différents motifs ont été observés dans des solutions avec différentes concentrations de PEO. Une variation du nombre de Reynolds critique, Re_c, et du nombre de Weissenberg critique, Wi_c, a été établie, correspondant à une augmentation abrupte du couple, pour différentes valeurs de El. Des boucles d'hystérésis dans les courbes $Nu_\omega(Re)$ et $Nu_\omega(Wi)$ ont été observées quand El augmente. Dans des solutions dont les valeurs de El sont voisines de 1, des paires solitaires de vortex stationnaires appelés diwhirls, ont été mises en évidence, lors de la décélération du cylindre intérieur, à partir du régime de turbulence viscoélastique. Leur taux de dissipation d'énergie a été mesurée et elle est significative. L'analyse du signal des fluctuations du couple pour des grandes valeurs du taux de cisaillement, $\dot{\gamma}$, indique la présence de turbulence inertio-élastique dans l'écoulement.

Ce projet m'a permis d'acquérir une connaissance profonde sur la mesure du couple sur nombreux systèmes de Coutte-Taylor. Le couple a été mesuré sur trois systèmes avec des différents rapports des rayons en utilisant le rhéomètre. La collaboration avec le Département d'Aérodynamique et Mécanique des Fluides de l'Université Technique de Cottbus-Senftenberg, en Allemagne, m'a permis de manipuler un système de Couette-

Taylor différent, lequel utilise de jauges de déformation comme méthode de mesure du couple. Des visualisations de l'écoulement ont été réalisées en utilisant différents outils de laboratoire (caméras de haute vitesse, sources de lumière blanches, lasers). Le traitement des images et la construction des diagrammes spatio-tempoels ont été réaliés avec des programmes spécifiques ou bien avec des programmes développés au sein du laboratoire. Les propriétés rhéologiques des fluides ont été mesurées avec plusieurs appareils de mesures, comme le densimètre, le viscosimètre, le rhéomètre de cisaillement ou le rhéomètre extensionnel (CaBER), le tensiomètre. Dans les cas du rhéomètre de cisaillement, nombreuses géométries ont été utilisées, comme des géométries de conne et plan avec de plusieurs angles ou des géomtries de *cup* et *bob*. Dans le cas de la rhéométrie extensionnel, j'ai appris à maitriser cette technique de mesure robuste pour obtenir les temps de relaxation caractéristiques des fluides viscoélastiques.

Finalement, la collaboration entre le laboratoire du Havre et celui de Cottbus a donné lieu à un projet de recherche de trois mois financé par le programme *European High performance Infrastrucures in Turbulence* (EuHIT). Ce programme européen m'a permis d'agrandir mes expériences de recherche dans un laboratoire différent et dans un pays différent. L'expèrience a été fructueuse, grâce à la possibilité d'échange des idées et de méthodes de travail.

Bibliography

[1] G. I. Taylor. Stability of a viscous liquid contained between two rotating cylinders. *Phil. Trans. R. Soc. Lond. A*, 223:289–343, 1923.

[2] C. D. Andereck, S.S. Liu, and H. L. Swinney. Flow regimes in a circular Couette system with independently rotating cylinders. *J. Fluid Mech.*, 164:155–183, 1986.

[3] M. Cross and H. Greenside. *Pattern Formation and Dynamics in Nonequilibrium Systems*. Cambridge University Press, 2009.

[4] F. Wendt. Turbulente strömungen zwischen zwei rotierenden konaxialen zylindern. *Ing.-Arch.*, 4(6):577–595, 1933.

[5] D. P. Lathrop, J. Fineberg, and H. L. Swinney. Turbulent flow between concentric rotating cylinders at large Reynolds number. *Physical review letters*, 68(10):1515, 1992.

[6] G. S. Lewis and H. L. Swinney. Velocity structure functions, scaling and transitions in high-Reynolds-number Couette-Taylor flow. *Phys. Rev. E*, 59:5457–5467, 1999.

[7] R. Ostilla-Mónico, E.P. van der Peol, R. Verzicco, S. Grossmann, and D. Lohse. Exploring the phase diagram of fully turbulent Taylor-Couette flow. *J. Fluid Mech.*, 761:1–26, 2014.

[8] R. Ostilla-Mónico, S. Huisman, T. J. G. Jannick, D. P .M Van Gils, R. Verzicco, S. Grossmann, C. Sun, and D. Lohse. Optimal Taylor-Couette flow: radius ratio dependence. *J. Fluid Mech.*, 747:1–29, 2014.

[9] B. Martínez-Arias, J. Peixinho, O. Crumeyrolle, and I. Mutabazi. Effect of the number of vortices on the torque scaling in Taylor-Couette flow. *J. Fluid. Mech.*, 748:756–767, 2014.

[10] R. C Di Prima and H. L. Swinney. Instabilities and transition in flow between concentric rotating cylinders. In *Hydrodynamics Instabilities and the transition to turbulence*, volume 45 of *Topics in Applied Physics*, pages 139–180. Springer, 1981.

[11] R.C. DiPrima, P.M. Eagles, and B.S. Ng. The effect of radius ratio on the stability of Couette flow and Taylor vortex flow. *Phys. Fluids (1958-1988)*, 27(10):2403–2411, 1984.

[12] H. J. Brauckmann and B. Eckhardt. Direct numerical simulation of local and global torque in Taylor-Couette flow up to $Re = 30\ 000$. *J. Fluid Mech.*, 718:398–427, 2013.

[13] S. Merbold, H. J. Brauckmann, and C. Egbers. Torque measurements and numerical determination in differentially rotating wide gap Taylor-Couette flow. *Phys. Rev. E*, 87:23014, 2013.

[14] F. Ravelet, R. Delfos, and J. Westerweel. Influence of global rotation and Reynolds number on the large-scale features of a Taylor-Couette flow. *Phys. Fluids*, 22:55103, 2010.

[15] T. T. Lim and K. S. Tan. A note on power-law scaling in a Taylor-Couette flow. *Phys. Fluids*, 16:140–144, 2004.

[16] D. P. Lathrop, J. Fineberg, and H. L. Swinney. Transition to shear-driven turbulence in Couette-Taylor flow. *Phys. Rev. A*, 46:6390–6405, 1992.

[17] S. G. Huisman, S. Scharnowski, C. Cierpka, C. J. Kähler, D. Lohse, and C. Sun. Logarithmic boundary layers in strong Taylor-Couette turbulence. *Phys. Rev. Lett.*, 110(26):264501, 2013.

[18] R. J. Donnelly and N. J. Simon. An empirical torque relation for supercritical flow between rotating cylinders. *J. Fluid Mech.*, 7:401–418, 1960.

[19] O. Reynolds. An experimental investigation of the circumstances which determine whether the motion of water shall be direct or sinuous, and of the law of resistance in parallel channels. *Proc. R. Soc. of London*, 35(224-226):84–99, 1883.

[20] A. Mallock. Determination of the viscosity of water. *Proc. R. Soc. Lond.*, 45:126–132, 1888.

[21] M. Couette. Etudes sur le frottement des liquides. *Annal. Chim. Phys.*, 6:433–510, 1890.

[22] L. Rayleigh. On the dynamics of revolving fluids. *Proceedings of the Royal Society of London. Series A, Containing Papers of a Mathematical and Physical Character*, pages 148–154, 1917.

[23] S Chandrasekhar. *Amer Math. Monthly*, pages 32–45, 1954.

[24] J. T. Stuart. On the non-linear mechanics of hydrodynamic stability. *J. Fluid Mech.*, 4(1):1–21, 1958.

[25] D. Coles. Transition in circular Couette flow. *J. Fluid Mech.*, 21:385–425, 1965.

[26] H. A. Snyder. Wave-number selection at finite amplitude in rotating Couette flow. *J. Fluid Mech.*, 35(2):273–298, 1969.

[27] J. P. Gollub and H. L. Swinney. Onset of turbulence in a rotating fluid. *Phys. Rev. Lett.*, 35(14):927–930, 1975.

[28] A. Barcilon, J. Brindley, M. Lessen, and F. R. Mobbs. Marginal instability in Taylor-Couette flows at a very high Taylor number. *J. Fluid Mech.*, 94:453–463, 1979.

[29] E. L. Koschmieder. Turbulent Taylor vortex flow. *J. Fluid Mech.*, 93:515–527, 1979.

[30] T. Mullin and T. B. Benjamin. Transition to oscillatory motion in the Taylor experiment. *Nature*, 288:567–659, 1980.

[31] T. B. Benjamin and T. Mullin. Notes on the multiplicity of flows in the Taylor experiment. *J. Fluid Mech.*, 121:219–230, 1982.

[32] G. I. Taylor. Fluid fraction between rotating cylinders. I. Torque measurements. *Proc. R. Soc. Lond. A*, 157:546–564, 1936.

[33] K. Nakabayashi, Y. Yamada, and T. Kishimoto. Viscous frictional torque in the flow between two concentric rough cylinders. *J. Fluid Mech.*, 119:409–422, 1982.

[34] R. Fernández-Feria. *Mecánica de fluidos.* Universidad de Málaga / Manuales, 2005.

[35] K. Coughlin and P. S. Marcus. Turbulent bursts in Couette-Taylor flow. *Phys. Rev. Lett.*, 77:2214–2217, 1996.

[36] Y. Takeda. Quasi-periodic state and transition to turbulence in a rotating Couette system. *J. Fluid Mech.*, 389:81–99, 1999.

[37] W. M. J. Batten, N. W. Bressloff, and S. R. Turnock. Transition from vortex to wall driven turbulence production in the Taylor-Couette system with a rotating inner cylinder. *Int. J. Numer. Meth. Fluids*, 38(3):207–226, 2002.

[38] A. Racina and M. Kind. Specific power input and local micro mixing times in turbulent Taylor-Couette flow. *Exp. Fluids*, 41:513–522, 2006.

[39] M. Bilson and K. Bremhorst. Direct numerical simulation of turbulent Taylor-Couette flow. *J. Fluid Mech.*, 579:227–270, 2007.

[40] D. Pirró and M. Quadrio. Direct numerical simulation of turbulent Taylor-Couette flow. *Eur. J. Mech. B/Fluids*, 27:552–566, 2008.

[41] C. S. Dutcher and S. Muller. Spatio-temporal mode dynamics and higher order transitions in high aspect ratio newtonian Taylor-Couette flows. *J. Fluid Mech.*, 641:85–113, 2009.

[42] M. J. Burin, E. Schartman, and H. Ji. Local measurements of turbulent angular momentum transport in circular Couette flow. *Exp. Fluids*, 48:763–769, 2010.

[43] B Dubrulle and F Hersant. Momentum transport and torque scaling in Taylor-Couette flow from an analogy with turbulent convection. *European Physical Journal B*, 26(3):379–386, 2002.

[44] B. Eckhardt, S. Grossmann, and D. Lohse. Torque scaling in turbulent Taylor-Couette flow between independently rotating cylinders. *J. Fluid Mech.*, 581:221–250, 2007.

[45] S. Grossmann and D. Lohse. Scaling in thermal convection: a unifying theory. *J. Fluid Mech.*, 407:27–56, 2000.

[46] B. Dubrulle, O. Dauchot, F. Daviaud, P.-Y. Longaretti, D. Richard, and J.-P. Zahn. Stability and turbulent transport in Taylor-Couette flow from analysis of experimental data. *Phys. Fluids*, 17:95103, 2005.

[47] C. R. Doering and P. Constantin. Energy equation in shear driven turbulence. *Phys. Rev. Lett.*, 69:1648–1651, 1992.

[48] M. S. Paoletti and D. P. Lathrop. Angular momentum transport in turbulent flow between independently rotating cylinders. *Phys. Rev. Lett.*, 106:24501, 2011.

[49] D. P. M. van Gils, S. G. Huisman, G.-W. Bruggert, C. Sun, and D. Lohse. Torque scaling in turbulent Taylor-Couette flow with co- and counterrotating cylinders. *Phys. Rev. Lett.*, 106:24502, 2011.

[50] S. G. Huisman, R. C. A. van der Veen, C. Sun, and D. Lohse. Multiple states in highly turbulent Taylor–Couette flow. *Nature Communications*, 5, 2014.

[51] R. Ostilla, R. J. A. M. Stevens, S. Grossmann, R. Verzicco, and D. Lohse. Optimal Taylor-Couette flow: direct numerical simulation. *J. Fluid Mech.*, 719:14–46, 2013.

[52] R. Ostilla-Mónico, E. P. van der Poel, R. Verzicco, S. Grossmann, and D. Lohse. Boundary layer dynamics at the transition between the classical and the ultimate regime of taylor-couette flow. *Phys. Fluids*, 26:015114, 2014.

[53] J. Kestin, J. V. Sengers, B. Kamgar-Parsi, and J. M. H. L. Sengers. Thermophysical properties of fluid H_2O. *J. Phys. Chem. Ref. Data*, 13(1):175–183, 1984.

[54] W. Wagner and A. Pruß. The IAPWS formulation 1995 for the thermodynamic properties of ordinary water substance for general and scientific use. *J. Phys. Chem.*, 31(2):387–535, 2002.

[55] Glycerine Producer's Association. *Physical Properties of Glycerine and Its Solutions*. Glycerine Producer's Association, New York, 1963.

[56] F.E. Jr. Bailey. *Poly(ethylene oxide)*. Academic Press, Inc., 1976.

[57] O. Crumeyrolle, I. Mutabazi, and M. Grisel. Experimental study of inertioelastic couette–taylor instability modes in dilute and semidilute polymer solutions. *Phys. Fluids*, 14(5):1681–1688, 2002.

[58] W.-M. Kulicke and C. Clasen. *Viscosimetry of polymers and polyelectrolytes*. Springer, 2004.

[59] C. Clasen, J.P. Plog, W.-M. Kulicke, M. Owens, C. Macosko, L.E. Scriven, M. Verani, and G. H. McKinley. How dilute are dilute solutions in extensional flows? *J. Rheol.*, 50(6):849–881, 2006.

[60] K. Watanabe, S. Sumio, and S. Ogata. Formation of taylor vortex flow of polymer solutions. *J. Fluids Eng.*, 128(1):95–100, 2006.

[61] L. E. Rodd, J. J. Cooper-White, D. V. Boger, and G. H. McKinley. Role of the elasticity number in the entry flow of dilute polymer solutions in micro-fabricated contraction geometries. *J. Non-Newtonian Fluid Mech.*, 143(2):170–191, 2007.

[62] F. Bossard, N. El Kissi, A. D'Aprea, F. Alloin, J.-Y. Sanchez, and A. Dufresne. Influence of dispersion procedure on rheological properties of aqueous solutions of high molecular weight PEO. *Rheol. Acta*, 49(5):529–540, 2010.

[63] O. Arnolds, H. Buggisch, D. Sachsenheimer, and N. Willenbacher. Capillary breakup extensional rheometry (CaBER) on semi-dilute and concentrated polyethyleneoxide (PEO) solutions. *Rheol. Acta*, 49(11-12):1207–1217, 2010.

[64] F. Kelai. *Etude expérimentale des intabilités viscoélastiques dans le système de Couette-Taylor*. PhD thesis, Université du Havre, 2011.

[65] C. S. Dutcher and S. J. Muller. Effects of moderate elasticity on the stability of co-and counter-rotating Taylor–Couette flows. *J. Rheol.*, 57(3):791–812, 2013.

[66] W. W. Graessley. Polymer chain dimensions and the dependence of viscoelastic properties on concentration, molecular weight and solvent power. *Polymer*, 21(3):258–262, 1980.

[67] N. Latrache, O. Crumeyrolle, and I. Mutabazi. Transition to turbulence in a flow of a shear-thinning viscoelastic solution in a Taylor-Couette cell. *Phys. Rev. E*, 86(5):056305, 2012.

[68] M. Stelter, G. Brenn, A. L. Yarin, R. P. Singh, and F. Durst. Validation and application of a novel elongational device for polymer solutions. *J. Rheol.*, 44(3):595–616, 2000.

[69] S. J. Haward, V. Sharma, C. P. Butts, G. H. McKinley, and S. S. Rahatekar. Shear and extensional rheology of cellulose/ionic liquid solutions. *Biomacromolecules*, 13(5):1688–1699, 2012.

[70] G. H. McKinley. Visco-elasto-capillary thinning and break-up of complex fluids. *Rheo. Rev.*, pages 1–48, 2005.

[71] L. E. Rodd, T. P. Scott, J. J. Cooper-White, and G. H. McKinley. Capillary break-up rheometry of low-viscosity elastic fluids. *Appl. Rheol*, 15:12–27, 2005.

[72] O. Crumeyrolle, N. Latrache, A. Ezersky, and I. Mutabazi. Instability modes observed in a viscoelastic Couette-Taylor flow. *Mécanique & Industries*, 4(4):397–409, 2003.

[73] Ö. Savaş. On flow visualization using reflective flakes. *J. Fluid Mech.*, 152:235–248, 1985.

[74] N. Abcha, N. Latrache, F. Dumouchel, and I. Mutabazi. Qualitative relation between reflected light intensity by kalliroscope flakes and velocity field in the couette-taylor flow system. *Exp. Fluids*, 45:85–94, 2008.

[75] P. Matisse and M. Gorman. Neutrally buoyant anisotropic particles for flow visualization. *Phys. Fluids (1958-1988)*, 27(4):759–760, 1984.

[76] M.A. Dominguez-Lerma, G. Ahlers, and D. S. Cannell. Effects of Kalliroscope flow visualization particles on rotating Couette–Taylor flow. *Phys. Fluids (1958-1988)*, 28(4):1204–1206, 1985.

[77] A. Esser and S. Grossmann. Analytic expression for Taylor-Couette stability boundary. *Phys. Fluids*, 8:1814–1819, 1996.

[78] O. Czarny, E. Serre, P. Bontoux, and R. M. Lueptow. Interaction between Ekman pumping and centrifugal instability in Taylor-Couette flow. *Phys. Fluids*, 15:467–477, 2003.

[79] C. S. Dutcher and S. J. Muller. Effects of weak elasticity on the stability of high Reynolds number co-and counter-rotating Taylor-Couette flows. *J. Rheol.*, 55(6):1271–1295, 2011.

[80] J.A. Cole. Taylor-vortex instability and annulus-length effects. *J. Fluid Mech.*, 75(01):1–15, 1976.

[81] K. A. Cliffe, J. J. Kobine, and T. Mullin. The role of anomalous modes in Taylor-Couette flow. *Proc. Roy. Soc. Lond. A*, 439:341–357, 1992.

[82] S. Tokgoz, G. E. Elsinga, R. Delfos, and J. Westerweel. Spatial resolution and dissipation rate estimation in Taylor-Couette flow for tomographic PIV. *Exp. Fluids*, 53:561–583, 2012.

[83] H. Görtler. Über den Einfluß der Wandkrümmung auf die Entstehung der Turbulenz. *ZAMM-J. Appl. Math. and Mech.*, 20(3):138–147, 1940.

[84] K.C. Muck, P.H. Hoffmann, and P. Bradshaw. The effect of convex surface curvature on turbulent boundary layers. *J. Fluid Mech.*, 161:347–369, 1985.

[85] P.H. Hoffmann, K.C. Muck, and P. Bradshaw. The effect of concave surface curvature on turbulent boundary layers. *J. Fluid Mech.*, 161:371–403, 1985.

[86] R.G. Larson, E. S. G. Shaqfeh, and S. J. Muller. A purely elastic instability in Taylor–Couette flow. *J. Fluid Mech.*, 218:573–600, 1990.

[87] G. S Beavers and D. D. Joseph. Tall taylor cells in polyacrylamide solutions. *Phys. Fluids*, 17(3):650–651, 1974.

[88] R. Haas and K. Bühler. Einfluß nichtnewtonscher stoffeigenschaften auf die taylorwirbelströmung. *Rheol. Acta*, 28(5):402–413, 1989.

[89] A. Groisman and V. Steinberg. Solitary vortex pairs in viscoelastic couette flow. *Phys. Rev. Lett.*, 78(8):1460, 1997.

[90] A. Groisman and V. Steinberg. Elastic vs. inertial instability in a polymer solution flow. *EPL*, 43(2):165, 1998.

[91] M. M. Denn and J. J. Roisman. Rotational stability and measurement of normal stress functions in dilute polymer solutions. *AIChE J.*, 15(3):454–459, 1969.

[92] A. Groisman and V. Steinberg. Elastic turbulence in curvilinear flows of polymer solutions. *New J. Phys.*, 6(1):29, 2004.

[93] A. N. Morozov and W. van Saarloos. Subcritical finite-amplitude solutions for plane couette flow of viscoelastic fluids. *Phys. Rev. Lett.*, 95(2):024501, 2005.

[94] M. Lange and B. Eckhardt. Vortex pairs in viscoelastic couette-taylor flow. *Phys. Rev. E*, 64(2; PART 2):027301–027301, 2001.

[95] K. Kumar and M. D. Graham. Finite-amplitude solitary states in viscoelastic shear flow: computation and mechanism. *J. Fluid Mech.*, 443:301–328, 2001.

[96] D. G. Thomas, B. Khomami, and R. Sureshkumar. Nonlinear dynamics of viscoelastic taylor–couette flow: effect of elasticity on pattern selection, molecular conformation and drag. *J. Fluid Mech.*, 620:353–382, 2009.

[97] N. Liu and B. Khomami. Polymer-induced drag enhancement in turbulent taylor-couette flows: Direct numerical simulations and mechanistic insight. *Phys. Rev. Lett.*, 111(11):114501, 2013.

[98] N. Liu and B. Khomami. Elastically induced turbulence in taylor–couette flow: direct numerical simulation and mechanistic insight. *J. Fluid Mech.*, 737:R4, 2013.

[99] A. S. Pereira and E. J. Soares. Polymer degradation of dilute solutions in turbulent drag reducing flows in a cylindrical double gap rheometer device. *J. Non-Newtonian Fluid Mech.*, 179:9–22, 2012.

[100] A. S. Pereira, R. M. Andrade, and E. J. Soares. Drag reduction induced by flexible and rigid molecules in a turbulent flow into a rotating cylindrical double gap device: Comparison between poly (ethylene oxide), polyacrylamide, and Xanthan Gum. *J. Non-Newtonian Fluid Mech.*, 202:72–87, 2013.

[101] R. M. Andrade, A. S. Pereira, and E. J. Soares. Drag increase at the very start of drag reducing flows in a rotating cylindrical double gap device. *J. Non-Newtonian Fluid Mech.*, 212:73–79, 2014.

[102] M.-K. Yi and C. Kim. Experimental studies on the taylor instability of dilute polymer solutions. *J. Non-Newtonian Fluid Mech.*, 72(2):113–139, 1997.

[103] C. W. McGary. Degradation of poly (ethylene oxide). *J. Polym. Sci.*, 46(147):51–57, 1960.

[104] A. Groisman and V. Steinberg. Couette-taylor flow in a dilute polymer solution. *Phys. Rev. Lett.*, 77(8):1480, 1996.

[105] B. M. Baumert and S. J. Muller. Axisymmetric and non-axisymmetric elastic and inertio-elastic instabilities in Taylor–Couette flow. *J. Non-Newtonian Fluid Mech.*, 83(1):33–69, 1999.

[106] S. J. Muller, R. G. Larson, and E. S. G. Shaqfeh. A purely elastic transition in taylor-couette flow. *Rheol. Acta*, 28(6):499–503, 1989.

[107] J. Beaumont, N. Louvet, T. Divoux, M.-A. Fardin, H. Bodiguel, S. Lerouge, S. Manneville, and A. Colin. Turbulent flows in highly elastic wormlike micelles. *Soft Matter*, 9(3):735–749, 2013.

Voy a parar en el camino
y en lo que dura un cigarrito
voy a pensar en estos años,
todo lo que ha pasado.

En el cajón de la memoria
guardo trocitos de la historia,
las páginas que ya han pasado
de un libro inacabado.

Platero y tú, “Cigarrito”.

Résumé

L'écoulement entre deux cylindres coaxiaux, appelé l'écoulement de Couette-Taylor, a été étudié lorsque le cylindre intérieur tourne. Quatre dispositifs ont été utilisés avec différentes tailles dentrefer. Les visualisations montrent l'évolution des motifs avec le nombre de Reynolds, *Re*. La variation du couple sur le cylindre intérieur a été détermine en utilisant le pseudo-nombre de Nusselt, qui est une mesure du taux de dissipation d'énergie.

Pour des faibles valeurs de Re, l'écoulement est laminaire et azimutal, et le couple est proportionnel à *Re*. Au-delà d'une valeur critique de Re, les rouleaux de Taylor apparaissent et la pente de variation du couple change brutalement. Pour de grandes valeurs de *Re*, les rouleaux deviennent turbulents et la pente du couple augmente à cause de la dissipation d'énergie turbulente. Le couple a été mesuré jusqu'à Re=45.000 et montre une dépendance avec le rapport de rayons des cylindres et du nombre de vortex. Avant le régime ultime de la turbulence, les états avec plus de rouleaux présentent un couple plus grand et la situation est inversée dans le régime ultime.

Une étude du couple agissant sur le cylindre intérieur a été menée en présence d'un liquide viscoélastique contenant des polymères de grande masse molaire. En appliquant des cycles d'accélération-décélération de la rotation du cylindre intérieur, le couple présente une boucle d'hystérèse dont l'aire augmente avec la concentration de polymère. Les statistiques des fluctuations de la turbulence élastique ont été analysées. Le couple exercé par les vortex solitaires obtenus lors de la phase de décélération, avant la relaminarisation complète de l'écoulement, a été étudié.

Mots clés : Écoulement de Couette-Taylor, Couple, Transfer de quantité de mouvement, rouleaux, turbulence, Dissipation, Viscoélasticité.

Abstract

The flow between two concentric cylinders, i.e., the Couette-Taylor flow, has been investigated when only the inner cylinder rotates. Four set-ups have been employed with 4 values of the radius ratio. Flow visualisations have been performed to analyse the evolution of the flow patterns with the Reynolds number, *Re*. The variation of the torque acting on the inner cylinder with different parameters has been quantified using the pseudo-Nusselt number, which measures the rate of energy dissipation in the flow.

At low Re, the flow is laminar and azimuthal, and the torque is proportional to Re. Above a critical value of *Re*, Taylor vortices emerge in the flow and the slope of the torque changes drastically. At high values of *Re*, the vortices become turbulent and the increase rate of torque is enhanced due to the energy dissipation of turbulence. The torque measured up to Re=45 000 depends on the radius ratio of the cylinders and on the number of vortices. Below the ultimate regime of turbulence, flows containing larger number of vortices exert larger levels of torque; above it, flows containing larger number of vortices exert lower levels of torque.

A specific study of the torque exerted on the inner cylinder has been carried out with viscoelastic fluids made of large-weight-molecule polymers. If acceleration-deceleration cycles of the rotation of the inner cylinder are applied, the torque exhibits a hysteretic loop, which increases with the polymer concentration. The statistics of the elastic turbulence fluctuations have been analysed. A special focus was made on the torque induced by the solitary vortices obtained in the deceleration phase, before the flow relaminarisation.

Keywords : Couette-Taylor flow, Torque, Momentum transfer, Vortex, Turbulence, Dissipation, Viscoelasticity.